DEPARTAMENTO DE ASTROFÍSICA

Universidad de La Laguna

Cold-flows in the local Universe

Memoria que presenta
Dña. Amanda María Del Olmo García
para optar al grado de
Doctor por la Universidad de La Laguna.

Trabajo dirigido por Prof. Jorge Sánchez Almeida
y codirigido por Prof. Casiana Muñoz Tuñón

INSTITUTO Đ ASTROFISICA Đ CANARIAS
julio de 2019

Examination date: July, 2019
Thesis supervisors: Prof. Jorge Sánchez Almeida, Prof. Casiana Muñoz Tuñón

Part of the material included in this document has been already published in *The Astrophysical Journal* and *Proceedings of the International Astronomical Union*.

Agradecimientos

Esta tesis no habría tenido lugar de no ser por el Instituto de Astrofísica de Canarias, por haberme contratado dentro del programa Astrofísico Residente "La Caixa" - Severo Ochoa, y a la Fundación La Caixa por haber financiado el programa.

Agradezco la labor de mis tutores Jorge y Casiana, por haberme guiado durante estos años. También a Ricardo Amorín por haberme acogido durante mi estancia en Cambridge, y a José Miguel por hacer de referee interno de esta tesis.

También quiero agradecer al personal de administración del IAC, de la Escuela de Doctorado y Estudios de Posgrado de la ULL, y la Comisión Académica del Doctorado en Astrofísica, que me han ayudado con los trámites burocráticos a lo largo de toda la tesis. El personal del CAU merece mención especial por solucionarme los problemas informáticos y recuperarme el disco duro.

A todas las personas que hacen la rutina más amena: a los compañeros de tan largas comidas y a mis compañeros de despacho. En especial a Carlos por ayudarme tanto con Python.

A Trini, Hari, Marcos, Inés y Efsan, por ser las mejores amigas que una pudiera tener, gracias por vuestro apoyo durante estos últimos años.

Por último, a mis padres y familia, que sin ellos no podría haber llegado hasta aquí. Gracias por todo.

En general, gracias a todas las personas que han contribuido al desarrollo de esta tesis y finalización de esta tesis.

Resumen

Uno de los principales mecanismos de formación de discos es la acreción de gas desde el medio intergaláctico (IGM; también llamada *cold-flow*). El gas acretado alimenta y es responsable de la formación estelar en las galaxias. La necesidad de este suministro de gas externo es evidente en las simulaciones numéricas, sin embargo, ha sido bastante difícil de confirmar observacionalmente. Esta tesis se centra en el estudio de galaxias extremadamente pobres en metales (XMP), en las que el gas que forma las estrellas tiene una metalicidad inferior a una décima parte de la metalicidad solar. Son relevantes en este contexto porque las XMPs parecen estar atravesando actualmente un evento de acreción de gas. El objetivo de esta tesis es investigar objetos que puedan indagar en este proceso de acreción de gas en el Universo local, y explorar varias posibilidades para restringir sus propiedades a través de observaciones.

Estudio las propiedades cinemáticas de 9 XMPs para saber si sugieren un evento reciente de acreción de gas. Derivo curvas de rotación y dispersión de velocidad a partir de los parámetros de la línea principal de Hα, obteniendo que las XMPs presentan movimientos turbulentos mayores que las velocidades de rotación, y que las regiones HII parecen moverse de manera coherente. Las alas de la línea de Hα presentan unas débiles componentes en emisión que parecen ser producidas por la expansión de estructuras en forma de concha. Del análisis de estas componentes, obtengo masas de gas, tasas de pérdida de masa y fracciones de masa arrastrada. Resulta que las XMPs son muy ineficientes en el uso del gas para formar estrellas, esto se demuestra por las grandes fracciones de masa arrastrada que mido. Los flujos de salida de gas deben compensarse con flujos de entrada de gas.

Busco candidatos de galaxias locales para detectar a su alrededor el medio circumgaláctico (CGM) y el IGM. Para ello, busco galaxias con estructuras no simétricas respecto al eje mayor de la galaxia en las imágenes profundas del proyecto IAC Stripe 82 Legacy Project. Las más interesantes primero se seleccionaron y luego se clasificaron según criterios morfológicos. Una de ellas fue seleccionada para una observación como prueba de concepto utilizando el Gran Telescopio Canarias (GTC). La observación se basó en la obtención de imágenes profundas para detectar la emisión débil y difusa de Hα en el CGM de la galaxia. La estrategia de observación y el proceso de reducción estuvieron orientados a reducir el ruido producido por la emisión del cielo, que es nuestro principal obstáculo. Detecto objetos con líneas de emisión alrededor de la XMP. La distribución de estos objetos no es uniforme al tener direcciones preferidas. También detecto un halo de emisión de bajo brillo superficial alrededor de la XMP. Analizo estas detecciones en términos del gas en el CGM y el IGM.

Como hay galaxias que están atravesando eventos de acreción de gas, debería haber galaxias entre esos eventos. Galaxias que comparten las propiedades de un anfitrión de XMP pero sin un estallido de formación estelar pobre en metales. Estas galaxias eran desconocidas hasta ahora. Analizo los espectros de GTC de la galaxia ultra-difusa UGC2162 que muestra todas las propiedades para ser una de esas galaxias.

Summary

One of the main mechanisms of disk formation is accretion of gas from the intergalactic medium (IGM; the so-called cold-flow accretion). The accreted gas fuels and is responsible for the star formation in galaxies. The need for this external gas supply is clear in numerical simulations, however it has been quite difficult to confirm observationally. This thesis is focused on the study of Extremely Metal-Poor (XMP) galaxies, where the star-forming gas has a metallicity smaller than a tenth of the solar metallicity. They are relevant in this context because XMPs seem to be undergoing a gas accretion event at present. The aim of this thesis is to investigate objects that could shed light into the process of cold-flow accretion in the local Universe, and to explore various possibilities to constrain it observationally.

I study the kinematic properties of 9 XMPs in order to know if they suggest a recent gas accretion event. I derive rotation curves and velocity dispersion from the parameters of the main Hα line, obtaining that XMPs present turbulent motions larger than the rotational velocities and that the HII regions appear to move coherently. The wings of Hα present faint emission features that seem to be produced by expanding shell-like structures. From the analysis of these components, I derive gas masses, mass loss rates, and mass loading factors. It turns out that XMPs are very inefficient at using the gas to form stars, this is evidenced by the large mass loading factors that I measure. Large outflow rates have to be balanced by large inflow rates.

I look for local galaxy candidates to detect around them the circumgalactic medium (CGM) and the IGM. I search for galaxies with non-axisymmetric structures in the deep images of the IAC Stripe 82 Legacy Project. The most interesting ones were first selected and then classified according to morphological criteria. One of them was selected for a proof-of-concept observation using GTC (Gran Telescopio Canarias). The observation consisted in deep imaging to detect faint diffuse Hα emission in the CGM of the galaxy. The observing strategy and the reduction process were aimed at reducing the noise produced by the sky emission, which is our limiting factor. I detect line emission clumps around the target galaxy. The distribution of the clumps is not uniform having preferred directions. I also detect a low surface brightness emission halo surrounding the target galaxy. I analyse these detections in terms of the gas in the CGM and the IGM.

As there are galaxies undergoing gas accretion events, there should be galaxies in between those events. Galaxies that share the properties of an XMP host but lacking a metal-poor starburst. These galaxies were so-far unknown. I analyse the GTC spectra of the ultra-diffuse galaxy UGC2162 that shows all

the properties to be one such galaxy.

Contents

List of Figures

List of Tables

1

Introduction and rationale

1.1 Introduction

According to cosmological numerical simulations, the accretion of cold pristine gas streams seems to be the preferred mode of galaxy disk assembly. This gas is the fuel for the star formation inside the galaxy and has to be replenished at the rate it is consumed into stars. Most galaxies have being forming stars from the early universe in a time span much larger than the timescale in which the gas is transformed into stars, therefore, galaxies have to keep accreting gas in order to sustain star formation. Although the need for external gas accretion is clear in numerical simulations, it has been quite difficult to confirm it observationally. This thesis explores new observational venues to confirm this key ingredient of the theory of galaxy formation.

This introductory chapter is organized as follows: in Section 1.1.1, I introduce the components of the circumgalactic medium (CGM) and the intergalactic medium (IGM) of galaxies, the importance of gas accretion process in the formation of galaxies, as well as the observational evidences of gas accretion reported in the literature. In Section 1.1.2, I present the targets of our study, namely, the Extremely Metal-Poor (XMP) galaxies of the local Universe, as they seem to be undergoing a gas accretion event at present. Finally, Sect. 1.2 lists the specific objetives of this thesis.

1.1.1 Gas accretion feeding the star formation process in galaxy disks

Gas in the CGM and IGM

The CGM is usually defined as the gas that surrounds galaxies, confined between their disks or interstellar medium (ISM) and their virial radii (e.g. Tumlinson et al. 2017). The gas beyond the virial radii is part of the IGM.

Observations of the IGM have been used to test the models of structure formation in cosmology (Viel et al. 2005; Seljak et al. 2005) and can be used to constrain the cosmogical initial conditions. Not only is important for the field of cosmology, but also for galaxy formation. The gas in the IGM feeds the galaxies (Kereš et al. 2005) and sets the minimum mass of galaxies (Rees 1986; Efstathiou 1992; Thoul & Weinberg 1996).

Most of the observations of the IGM come from the redshift range $2 < z < 5$, mainly because the Lyα can be observed in the optical range and there are a high number of bright quasars with good signal to noise in the spectra. The IGM is probed by the Lyα forest, which is produced by Lyα absorption of intergalactic neutral hydrogen clouds in the sightline of quasars (Bahcall & Salpeter 1965; Gunn & Peterson 1965). Also with cosmological hydrodynamics simulations, one can produce a mock Lyα forest spectrum to compare with the observations (Zhang et al. 1995; Hernquist et al. 1996). From the study of the Lyα forest we can measure the HI column density distribution, the thermal history of the IGM and the metal enrichment of intergalactic gas. Not only galaxies feed from the IGM, but the winds generated in supernova explosions can reach the IGM (depending on the velocity and the depth of the potential well) and enrich it. The fraction of metals retained in a galaxy ISM is around 20%, for stellar masses in the range $9.5 \leq \log(M_*/M_\odot) \leq 11.5$ (Peeples et al. 2014). If we go to the local universe, the IGM is harder to study for two reasons. First, the cosmological expansion of the universe makes the Lyα forest more transmissive and, second, the Lyα lines are now observed in the UV which requires space-borne telescopes. Shull et al. (2012) found that only $30 \pm 10\%$ of the $z \sim 0$ gas is seen in Lyα absorption and that $\sim$10% of the baryons can be found on galaxies, galaxy groups, and clusters. There is a missing fraction of baryons that we can not observe, also known as the missing baryon problem (Bregman 2007). Also, the amount of dark matter that belongs to the intergalactic medium has changed over cosmic time, while at present $\sim$50% of dark matter is in intergalactic structures, at larger redshifts ($z = 3$), the fraction increases to 80% (McQuinn 2016).

The CGM was firstly studied by the observation of absorption lines of heavy

elements in the spectra of background objects like quasars (e.g., Spitzer 1956; Münch & Zirin 1961; Bahcall & Spitzer 1969). This method provides information even in low column densities (N $\simeq 10^{12}$ cm^{-2}) but depends on the availability of quasars. Since then, new methods have been added to study the CGM, for example the staking of spectra of galaxies. This method consists on averaging the spectra after correcting for redshift and normalization of the continuum, which increases the signal to noise of weak lines, but loses information from individual sources. Another method is studying the line emission directly. Observations have been done in the UV and X-rays, for example the Lyα extended emission found by Arrigoni Battaia et al. (2019). Apart from observations, the CGM can be studied in hydrodynamic simulations, where the physical details are known and controlled.

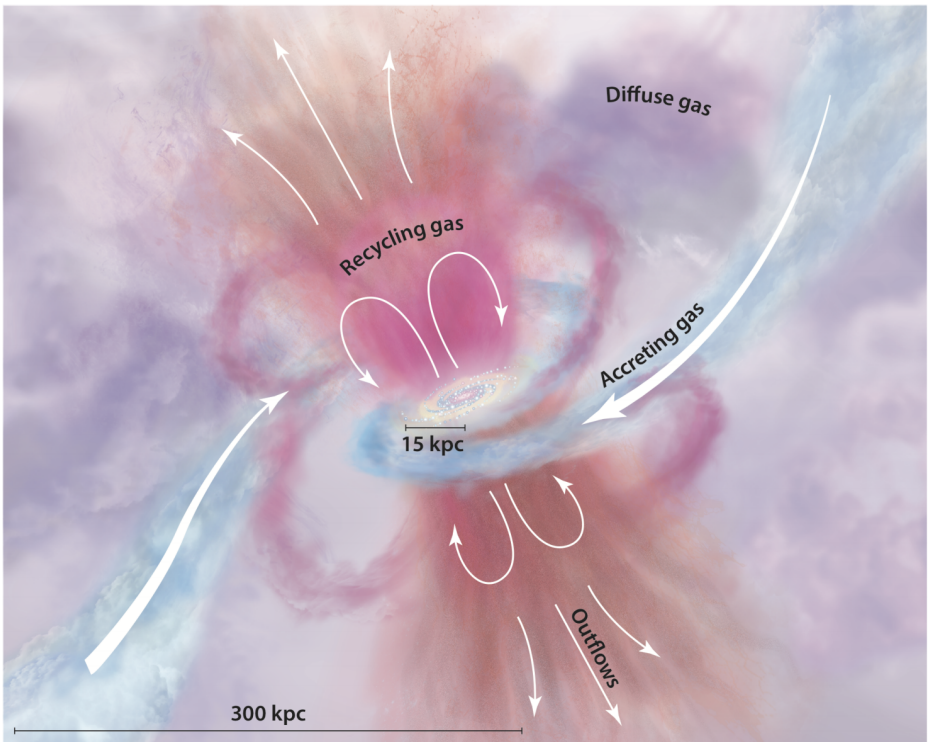

Figure 1.1: A cartoon view of the CGM. The galaxy gaseous disk is fed by filamentary accretion from the IGM (blue). Outflows emerge from the disk in pink and orange, while gas that was previously ejected is recycling. The "diffuse gas" halo in varying tones of purple includes gas that is likely contributed by all these sources and mixed together over time. From Tumlinson et al. (2017)

The key elements of the CGM are the inflows, outflows and the recycled materials (see Fig. 1.1). Inflows are fundamental in the formation of galaxies as they provide gas to form stars. This gas can come from interaction with other galaxies or from the IGM. More details about gas accretion from the IGM will be given in the following sections. Outflows are built up mainly from supernovae explosions, stellar winds and the ejecta of supermassive blackholes. They swept up the gas in the ISM towards the CGM and the IGM, depending on their velocity and the potential well of the galaxy. So, they reduce the metallicity of the galaxy and pollute the CGM and the IGM with the metals present in the ISM. The gas expelled by the galactic winds could be reaccreted onto the galaxy if the cooling time is short; this process is known as recycling. Although the timescales are not clear, simulations confirm the accretion of gas that has been previously in the ISM (Ford et al. 2014). However, most of the gas used to form stars is locked in low mass stars and stellar remnants, and never returns to the ISM.

With all this information, we know that the role of the CGM is fundamental in a galaxy as it provides them with fuel to maintain the star formation, coming both from the IGM and from the galaxies as recycled material. The interplay between these processes determines the evolution of galaxies (Kereš et al. 2005; Dekel & Birnboim 2006; Putman et al. 2012) Therefore, observations of the CGM are needed to confirm the models of galaxy evolution.

What is gas accretion?

As I explain in the previous subsection, one of the main mechanisms of disk formation is the accretion of gas from the IGM and the cosmic web, specially in the early Universe (Dekel et al. 2009; Silk & Mamon 2012; Fox & Davé 2017). The cosmic web refers to the large-scale distribution of galaxies in the Universe and, depending on its mass density, it is named as clusters, filaments, sheets and voids (Bond et al. 1996).

The gas from the cosmic web is accreted by the galaxy, through a process whose efficiency depends on the mass of the galaxy halo (Birnboim & Dekel 2003; Kereš et al. 2005). In galaxies with massive halos ($> 10^{12} M_{\odot}$), the accreted gas is heated to the virial temperature by shocks and needs long time to cool down and fall on to the galaxy disk. In galaxies with small halo, the accreted gas barely interacts with the halo. The gas can reach the protodisk in clumps and filaments and begins to form stars. This mode of cosmic web gas accretion is also known as cold-flow (Dekel et al. 2009). At high redshift (early universe) most of the galaxies are low mass, so cold-flow accretion is the main process of galaxy build up. In the local universe, cold-flow accretion is important in isolated dwarf galaxies (merger interaction is more important in

clusters, for example). These inflows are comparable in mass rate to the outflows produced by SN explosions and stellar feedback, so only a small fraction of the accreted gas is used to form stars (Davé et al. 2012; Shen et al. 2012).

The cold flows are expected to be partly ionized, low temperature ($10^4 \leq$ T $\leq 10^5$ K), and low-metallicity (van de Voort & Schaye 2012). One source of ionization is fluorescence of UV photons from the galaxy or the UV background. The inflow of gas is driven by gravity, so the velocity is similar to the Keplerian velocity of the outer parts of the disk ($50 - 100$ km s^{-1} depending on the halo mass). Also, the spatial scale of the gas in the IGM is several times the size of the galaxies. The effect of the gas accretion depends on the size of the gas stream; it could impact in a small portion of the galaxy or the whole disk. Although simulations predict rather broad cosmic gas streams, larger than the virial radius of a dwarf galaxy, the streams could develop small scale structures of the size of a galaxy or even smaller (e.g., Ceverino et al. 2010). See Fig. 1.1 for a cartoon.

Bathtub model

There is an interplay between the elements of the CGM and gas in the ISM of a galaxy. A simple model, known as bathtub model (Bouché et al. 2010; Dekel & Mandelker 2014; Sánchez Almeida et al. 2014a), has been used to gain physical insight into the fundamental processes. It assumes the galaxies to be 1-D objects characterized by a gas mass $\mathrm{M_g}$. Then the conservation of mass grants,

$$\frac{d\mathrm{M_g}}{dt} \equiv \dot{\mathrm{M}}_\mathrm{g} = -(1-R)\mathrm{SFR} + \dot{\mathrm{M}}_\mathrm{in} - \dot{\mathrm{M}}_\mathrm{out}, \tag{1.1}$$

where $\mathrm{M_g}$ is the gas mass available to form stars, R represents the fraction of the mass in stars that returns to the ISM through stellar winds and SN eyecta, SFR gives the star formation rate, $\dot{\mathrm{M}}_\mathrm{in}$ stands for the gas inflow rate, and $\dot{\mathrm{M}}_\mathrm{out}$ is the gas outflow rate. It is also assumed that the SFR is proportional to the gas mass, and the outflow rate to the SFR, with scaling factors being the time consumption timescale (τ_g) and the mass-loading factor (w) respectively,

$$\mathrm{SFR} = \frac{\mathrm{M_g}}{\tau_\mathrm{g}} \qquad ; \qquad \dot{\mathrm{M}}_\mathrm{out}(t) = w\,\mathrm{SFR}(t). \tag{1.2}$$

In this situation more gas mass means more star formation which reduces the gas mass available, producing self regulation of the system in a timescale given by τ_g. Assuming that the scaling factors are constant and that τ_g is much shorter than the other relevant timescales, a stationary-state is reached where the solution to Eq. (1.1) becomes,

$$\mathrm{SFR}(t) \simeq (1 - R + w)^{-1}\,\dot{\mathrm{M}}_\mathrm{in}(t). \tag{1.3}$$

It shows that the SFR in the stationary state is set by the gas infall rate (corrected for returned fraction R and outflows w). The value of R is provided by stellar evolution models, and varies in the range $0.2-0.3$ depending on the IMF (Initial Mass Function). The mass loading factor w varies with stellar mass, reaching large values in low mass galaxies (Veilleux et al. (2005); Christensen et al. (2016); we measure it in Chapter 2). When $w \gg 1$, the SFR is smaller than the accretion rate and most of the gas returns to the CGM and IGM without being used to form stars.

In addition, the mass of gas is also controlled by the infall rate to be the amount needed to sustain the SFR forced by the infall rate, i.e.,

$$\mathrm{M_g}(t) \simeq \tau_\mathrm{g}\,\mathrm{SFR}(t) \simeq \frac{\tau_\mathrm{g}}{1-R+w}\,\dot{\mathrm{M}}_\mathrm{in}(t). \tag{1.4}$$

We know from observations that τ_g goes from 0.5 to 2 Gyr for galaxies in the redshift range between 2 and 0 (Genzel et al. 2010; Gnedin et al. 2014). Equations (1.3) and (1.4) tell us that galaxies self-regulate to maintain the gas needed to produce a SFR set by the balance between inflows and outflows.

Observational evidences of gas accretion

Besides numerical simulations, there is no direct or clear observational evidence of cold-flow accretion. There is an ongoing quest for this cosmic gas, with only partial and/or indirect success (see Sancisi et al. 2008; Sánchez Almeida et al. 2014a; Sánchez Almeida 2017, and references therein). Lyα and metallic line absorptions on quasar spectra seem to be created by gas in the IGM (see, e.g., Fumagalli et al. 2011a). Gallego et al. (2018) found that the gas density in the CGM of galaxies increases in the direction towards its neighbours, on cosmological scales. Metallicity inhomogeneities in disk galaxies appear to be the result of pristine gas accretion (Cresci et al. 2010; Sánchez Almeida et al. 2013, 2015, 2018a; Hwang & et al. 2018; Sánchez-Menguiano et al. 2019). Cosmic web gas may explain some of the HI filaments found in blind HI surveys (Popping & Braun 2011), as well as some of the high velocity clouds detected around our galaxy (e.g., Sancisi et al. 2008). Also, the infall of metal poor gas could fix the mismatch between the observed stellar metallicity distribution in the solar neighbourhood with the values predicted by closed-box models of chemical evolution (the so-called *G-dwarf problem*; for the models see, e.g., Tinsley 1981; Matteucci 2004). Estimations of current accretion rates (0.2 $\mathrm{M_\odot}$ $\mathrm{yr^{-1}}$) are insufficient to sustain the star formation rate (≈ 1 $\mathrm{M_\odot}$ $\mathrm{yr^{-1}}$) in galaxies as massive as the Milky Way for long periods of time (Sancisi et al. 2008), needing extra accretion of gas. An anticorrelation has been found between the star formation rate (SFR) and the ionized gas metallicity (Cresci et al. 2010;

Lara-López et al. 2010; Pérez-Montero et al. 2013; Andrews & Martini 2013) for galaxies of the same mass. This can be explained as the infall of metal-poor gas that simultaneously enhances the star formation in these galaxies and drop their metallicity (Brisbin & Harwit 2012; Davé et al. 2012). Finally, Lyα emission has been detected in cosmic web filaments (Martin et al. 2014; Cantalupo et al. 2014; Wisotzki et al. 2016), and such emission becomes pervasive when going faint enough, so that any line-of-sight intercepts emitting gas between redshift 6 and 3 (Wisotzki et al. 2018). These findings are rather indirect, in the sense that connecting them with the numerical simulations still requires a significant dose of interpretation.

1.1.2 XMP galaxies

As we explained in the previous section, cold-flow accretion is an important process for the formation of galaxies, so it is fundamental to understand it. There is little observational evidence of it, even less in the local universe. In order to analyse how the cold-flow accretion works, we have chosen to study XMP galaxies which, as we will explain in detail later, seem to have star formation supported by gas accretion. They are local galaxies, so that they can be studied in much detail compared to other studies of gas accretion in high redshift.

What are XMPs?

XMP galaxies are, by definition, galaxies in which the star-forming gas has a metallicity smaller than a tenth of the solar metallicity (e.g., Kunth & Östlin 2000). They are also the least metallic galaxies in the local Universe. With the exception of primordial nucleosynthesis, the formation of elements heavier that He primarily occurs in stars and supernova explosions. It means that the star-forming gas in XMPs is chemically primitive compared with the rest of the galaxies.

In terms of their absolute magnitude, XMPs can be separated in two types. The first type is ultra-faint late-type galaxies, with $M_B \geq -12.5$. From the luminosity-metallicity relation (e.g., Skillman et al. 1989) we can expect than the most faint galaxies ($M_B \geq -12.5$) should be XMPs (Berg et al. 2012; Sánchez Almeida et al. 2017). These type of XMPs are particularly rare in surveys (e.g., James et al. 2015; Sánchez Almeida et al. 2017) due to several factors: the Malmquist bias, their low surface brightness, and the fact that the low luminosity range of their luminosity function is shallower than expected. The second type, with $M_B < -12.5$, are galaxies with lower metallicity than the expected from the luminosity-metallicity relation. As they have high surface

brightness, they dominate the catalogs of XMPs (Morales-Luis et al. 2011; Izotov et al. 2012; Sánchez Almeida et al. 2016), and they are the subject of our study. The evolutionary pathways of the two types probably differ. In this thesis the term XMP refers exclusively to the second type. XMPs represent less than 0.1 % of the objects in galaxy catalogs (e.g., Sánchez Almeida et al. 2016), they tend to appear in low-density environments with ∼75% of them residing in voids and sheets (Filho et al. 2015).

Measured properties

XMPs are local dwarf galaxies with one or several metal poor star-forming knots, while the host galaxy is between 5 and 10 times more metal-rich (Sánchez Almeida et al. 2013, 2015). The position of the main starburst does not usually match the photometric center of the galaxy, making the galaxy to have a cometary or tadpole morphology (Papaderos et al. 2008; Morales-Luis et al. 2011). This can be interpreted as a sign that XMPs are disks in early stages of assembly. They are very gas rich, with a gas to stellar mass ratio in excess of 10 ($M_{\rm HI}/M_\star \gtrsim 10$, Filho et al. 2013). XMP galaxies present low rotational motion compared with the velocity dispersion (e.g., Sánchez Almeida et al. 2013; Olmo-García et al. 2017). Under these conditions, gas mixes rapidly, in a rotation period (e.g., de Avillez & Mac Low 2002; Yang & Krumholz 2012), which suggests the recent arrival of the gas fuelling the present star-formation episode.

Origin of the metal poor gas

Several explanations have been proposed for the presence of metal-poor gas in XMPs; we summarise some of them here. One possibility is that the galaxy is forming its first generation of stars, however this is not consistent with the presence of higher metallicity gas in the same galaxy (Sánchez Almeida et al. 2014b) neither the presence of old stellar populations (Elmegreen et al. 2012b, 2016a). The inhomogeneities could be explained by the model of propagating star formation (Papaderos et al. 2008), where the surface brightness decreases and the age and metallicity increases as we move from the position of the current starburst. Sánchez Almeida et al. (2014b) discuss whether the metallicity inhomogeneities are real or can be caused by other things apart from cold flow accretion, like temperature or density fluctuations, not considering higher ionization states of oxygen, and escape of metals. As XMPs have very low mass, they can easily blow away the metals produced and ejected during SNa explosions (Mac Low & Ferrara 1999). This could produce a deficit of metals in the gas around the starburst, compared to the rest of gas in the galaxy. As I discuss in Sect. 1.1.1, this situation can not be maintained for long, since more

metal poor gas would be needed to feed the star formation, which cannot mix with the gas in the rest of the galaxy.

The most promising explanation for the origin of the metal-poor gas is accretion from an external near metal-free cloud, as expected from cold-flows in numerical simulations. The key is the presence of chemical inhomogeneities in XMPs, for two reasons. First, the timescale for mixing in disk galaxies is short, so the metal-poor gas must have been recently accreted. Second, the secular evolution produces disks with a metallicity decreasing inside-out (e.g., Vilchez et al. 1988; van der Kruit & Freeman 2011; Moran et al. 2012), which do not match the chemical behaviour of XMPs. It appears to be a lower limit in the observed metallicity of XMP galaxies. None of them have measured metallicity value below $\sim$1/50 of the solar metallicity, which roughly corresponds to the metallicity of the prototypical XMP galaxy IZw18 (Izotov & Thuan 1999). This threshold can be explained as the metallicity of the IGM gas at the present time, which is predicted to be around the observed limit (Fumagalli et al. 2011b).

Sample of XMP galaxies used in the thesis

In this thesis, I work with two lists of XMP galaxies; the first one was collected by Morales-Luis et al. (2011) and the second one was selected by Sánchez Almeida et al. (2016).

Morales-Luis et al. (2011) carried out an automated search for XMP galaxies in the Sloan Digital Sky Survey (SDSS) DR7. For the search, they use the fact that the ratio between the emission lines [NII]λ6584 and Hα is a proxy for the metallicity of the galaxy. They use the machine learning algorithm *k-means* to classify the spectrum around these lines. This algorithm classifies the spectra according to the shape of the spectrum, with no supervision. From the output of the algorithm, they selected the galaxies in the classes with minimum ratio between [NII] and Hα. They apply the algorithm several times rejecting some classes to improve the classification. Through this method they found 32 XMPs. They also perform a search of XMPs in the literature which, together with the previous objects, make a list of 141 XMPs.

Sánchez Almeida et al. (2016) search for XMP galaxies in the SDSS using the fact that the ratio of the lines [O III]λ4363 to [O III]λ5007 is a proxy for the electron temperature. As the gas in XMP galaxies have very little metals, it can not cool efficiently, so the gas must have a relatively high electron temperature. Again, they use *k-means* to classify the spectra. They select the two classes with the largest [O III]λ4363 emission and apply *k-means* again. They remove classes with noisy spectra and classes in which the source of excitation is the radiation from an active galactic nuclei (AGN) instead of HII regions. For the

selected candidates (1281), they measure the metallicity with the code H ii-CHImistry (Pérez-Montero 2014) (which is consistent with the direct method when [O III]λ4363 is available) and select those with an oxygen abundance below 7.69. This correspond to 1/10 of the solar oxygen abundance as measured by Asplund et al. (2009). The selection leads to 196 XMPs, or 332 XMPs depending on whether a rejection threshold of 3 times the noise or 2 times the noise is used to accept the measured fluxes (see Sánchez Almeida et al. (2016) for further details).

1.2 Rationale

The aim of this thesis is to investigate objects that could shed light into the process of cold-flow accretion in the local Universe, and to explore various possibilities to constrain it observationally. Explicitly, I will

(a) search for potential local galaxy candidates to detect the CGM and IGM around them. I looked for XMPs present in the deep images of the IAC Stripe 82 Legacy Project. I selected galaxies with non-axisymmetric structures and classified them according to morphological criteria. This search is described in appendix A. The target of the observations in Chapter 3 was chosen from the list of potential candidates included in the appendix.

(b) Characterize the kinematics of galaxies going through a gas accretion event at present. I want to know if their kinematic properties suggest a recent gas accretion event. I explore this question in Chapter 2, where I analyse the kinematics along the mayor axis of 9 XMPs. I study the parameters of the main Hα line to derive rotation curves and velocity dispersion. I also study the faint emission features in the wings of Hα that seem to be produced by expanding shell-like structures. I derive gas mass, mass loss rates, and mass loading factors.

(c) Detect and characterize the gas around galaxies that may be going through a gas accretion event at present. This gas is expected to emit recombination lines through fluorescence of UV photons or gravity-driven cooling, with surface brightness in the range of $25.6 - 36.8$ mag/arcsec^2. In a proof-of-concept observation to detect it, we took deep Hα imaging with the GTC telescope, targeting an XMP galaxy and its environment. The observations are described in detail in Chapter 3. The observing strategy and the reduction process were aimed at minimising the noise of the sky

residual, which is the main limiting factor in the detection of such faint sources.

(d) Find and characterize galaxies between gas accretion events. There should be galaxies with the properties of an XMP host but without metal-poor starbursts. In Chapter 4 I analyse the ultra-diffuse galaxy UGC2162, which has low surface brightness and relatively high metallicity, making it a candidate of being an XMP host.

The various chapters are uneven in length and scope. Each one is self-contained, so that eventually, all of them will end up as individual papers. The work presented in Chapter 2 and Chapter 4 are already published (Olmo-García et al. 2017; Sánchez Almeida et al. 2018b), whereas the contents of Chapter 3 are about to be submitted.

2

Kinematic properties of Extremely Metal-poor Galaxies[1]

2.1 Introduction

There is evidence pointing out that XMP galaxies are growing through cold-flow accretion. In particular, the presence of chemical inhomogeneities in most XMPs, since they show that star formation in XMPs is fed by external metal-poor gas (see Sect. 1.1.2). In order to put the presence of these inhomogeneities on a firm observational basis, Sánchez Almeida et al. (2015) (SA+15) measured the oxygen abundance along the major axes of ten XMPs, using a method based on models consistent with the direct method (Pérez-Montero 2014). In nine out of ten cases, sharp metallicity drops were found, leaving little doubt as to the existence and ubiquity of the drops.

In this chapter we follow up on the work of SA+15, and measure the kinematic properties of these XMPs. The spectra used to infer metallicities in SA+15 do not possess enough spectral resolution to carry out kinematic studies. Therefore, a new set of observations was obtained. For this reason, the overlap with the original XMP sample is not complete. However, most of the original galaxies are examined here and show evidence for the star-forming regions having coherent motions, which also hints at the external origin of the galaxy gas. In addition, the Hα line presents multiple side lobes that seem to trace feedback processes of the star formation on the ISM (interstellar medium)

[1]Based on the work of Olmo-García et al. (2017)

of the galaxies. Since we use Hα, our measurements characterize the properties of the ionized gas near the sites of star formation.

The chapter is organized as follows: Sect. 2.2 describes the observations and data reduction, emphasizing the aspects required to obtain the spectral resolution needed for the kinematic analysis. Sect. 2.3 describes how physical parameters are obtained from the calibrated spectra. It is divided into various parts; one for the main Hα signal (Sect. 2.3.1), and three for the secondary lobes (Sects. 2.3.2, 2.3.3, and 2.3.4). The overall properties, such as rotation, turbulent motions, and global expansion, are presented in Sect. 2.4. In this section, I also study the change of the N/O ratio along the major axis of the galaxies. The properties of the multiple secondary components bracketing the main Hα component are presented and interpreted in Sect. 2.5. They appear to trace gas swept by the star formation process, and in Sect. 2.6 we predict the properties when this gas reaches the CGM (circumgalactic medium). Our results are summarized and discussed in Sect. 2.7. The emission expected from an expanding dusty shell of gas is formulated in Appendix 2.8.

2.2 Observations and data reduction

2.2.1 Observations

For the study of the kinematics of XMPs, we selected a sample of 9 galaxies, 8 of which were previously studied in SA+15 (see Table 2.1), and thus have spatially resolved measurements of oxygen abundance. This time the galaxies were observed with the ISIS[2] instrument on the 4.2 m William Herschel Telescope (WHT), using high resolution gratings[3] (R1200R and R1200B). The slit of the spectrograph was positioned along the major axis of the galaxies (see Fig. 2.1), overlaying the slit used in SA+15. The slit width was selected to be 1 arcsec, according to the seeing at the telescope and also matching the value of our previous observation of these galaxies in SA+15. The spectrograph has two arms, the red and the blue arm, each one with its own detector. All galaxies were observed in both arms, except for HS0822, where we only had the red spectrum. A 2×2 binning of the original images was performed to reduce oversampling. After binning, the dispersion turns out to be 0.52 Å pix^{-1} for the red arm and 0.46 Å pix^{-1} for the blue arm. Similarly, the spatial scale is 0.44 arcsec pix^{-1} for the red arm and 0.40 arcsec pix^{-1} for the blue arm. The wavelength coverage for the blue arm is 940 Å centered at Hβ (from 4390 Å to

[2]Intermediate dispersion Spectrograph and Imaging System. http://www.ing.iac.es/Astronomy/instruments/isis/

[3]`http://www.ing.iac.es/astronomy/telescopes/wht/`

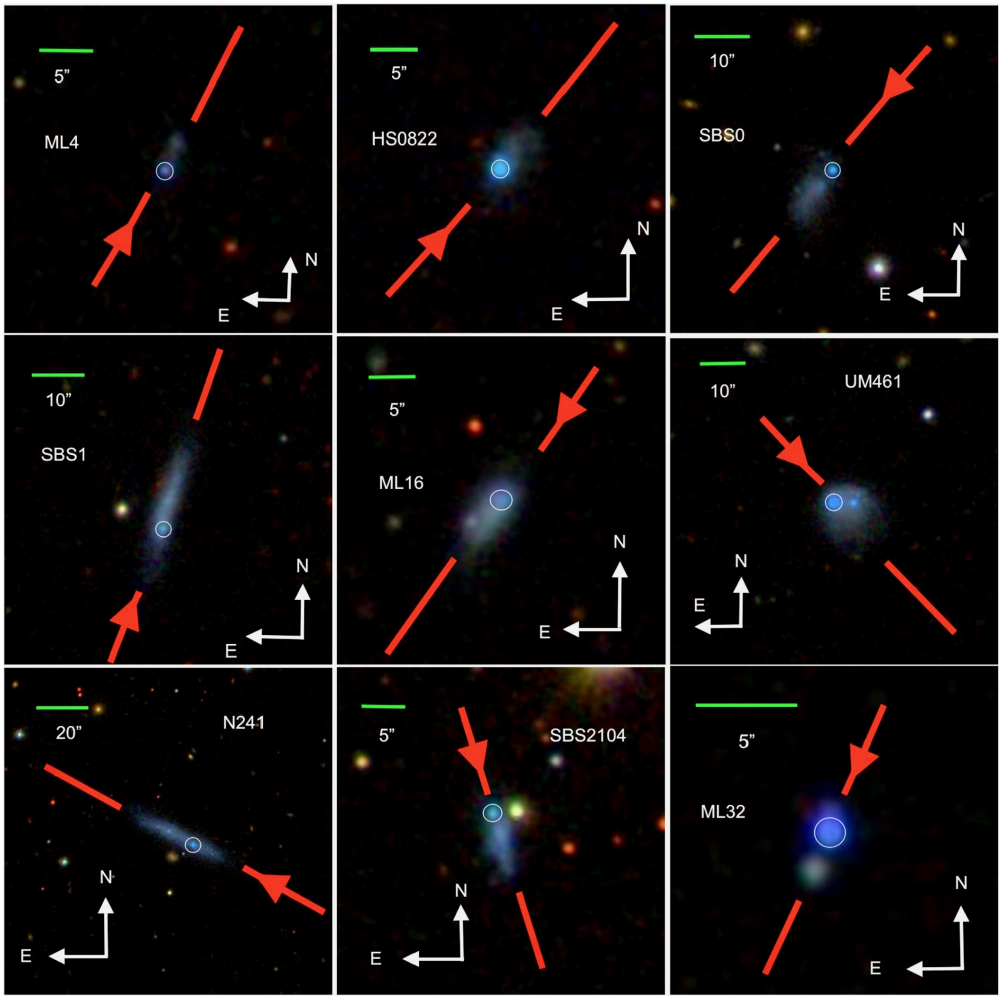

Figure 2.1: SDSS color images of the galaxies observed in this work, with the red bar indicating the position of the spectrograph slit. It will be the spatial axis in the following figures, and the arrow points in the direction in which the distance increases. The green bar provides the scale on the sky. The circles enclose the main star-forming region in each galaxy. These images had been tweaked to appear brighter and be seen clearly in the printed version.

5330 Å), whereas the red arm covers 1055 Å around Hα (from 6035 Å to 7090 Å). The total exposure time per target was approximately two hours (Table 2.1), divided in snapshots of 20 minutes as a compromise to simultaneously minimize cosmic-ray contamination and readout noise.

The spectral resolution was measured from the FWHM (full width at half maximum) of several telluric lines, using the calibrated data described in the next section. They yield a value of approximately 40 $\mathrm{km\,s^{-1}}$ (Table 2.1), which renders a spectral resolution close to 7500 at Hα. This resolution is in good agreement with the value expected for the 1 arcsec slit, once the anamorphic magnification of ISIS is taken into account (Schweizer 1979).

The angular resolution during observations ranges from fair (1.3 arcsec) to good (0.5 arcsec), as measured by the seeing monitor at the telescope (Table 2.1). Additional information on the galaxies and the observations is included in Table 2.1.

2.2.2 Data reduction

The spectra were reduced using standard routines included in the IRAF[4] package. The process comprises bias subtraction, flat-field correction using both dome and sky flat-fields, removal of cosmic-rays (van Dokkum 2001), and wavelength calibration using spectral lamps. In order to evaluate the precision of the wavelength calibration, we measured the variation of the centroids of several sky emission lines along the spatial direction (if the calibration were error-free, the telluric line wavelength should not vary). For different galaxies and emission lines, the root mean square (RMS) variation of the centroids ranges from 0.036 Å to 0.072 Å, which corresponds to 1.6 $\mathrm{km\,s^{-1}}$ and 3.3 $\mathrm{km\,s^{-1}}$, respectively. It drops even further if only strong telluric lines are considered.

The sky subtraction, the geometrical distortion correction, and the combination of the spectra of each single source were carried out using Python custom-made routines. For the sky subtraction, we performed a linear fit, sampling the sky on both sides of the galaxy spectrum. This model sky emission was then subtracted from each wavelength pixel. The effect of the geometrical distortion is that the spatial and wavelength direction are not exactly perpendicular to each other on the detector. We determine the angle between the two directions as the angle between the continuum emission of the brightest point in the galaxy and the telluric lines. A linear fit allowed us to model the geometric transformation needed to make the spatial and wavelength axes perpendicular.

[4] `http://iraf.noao.edu/` IRAF is distributed by the National Optical Astronomy Observatory, which is operated by the Association of Universities for Research in Astronomy (AURA) under cooperative agreement with the National Science Foundation.

Table 2.1: Parameters of the observed XMP galaxies.

Our ID	Galaxy name	Obs. Date dd/mm/yyyy	Seeing [b] [arcsec]	W_{Ui} [c] [km s^{-1}]	D [d] [Mpc]	Scale [d] [pc arcsec^{-1}]	Exp. Time [s]	$\log M_\star$ [e] [M$_\odot$]
ML4	J030331.26 − 010947.0	16/08/2012	0.5	38.1 ± 2.7	125 ± 9	608	3600	8.33 ± 0.33
HS0822	J082555.52 + 353231.9	02/02/2013	1.4	37.8 ± 1.6	9.6 ± 0.7	47	7200	6.04 ± 0.03
SBS0	J094416.59 + 541134.3	15/03/2015	0.9	41.1 ± 3.2	23.1 ± 1.6	112	4800	7.05 ± 0.05
SBS1	J113202.41 + 572245.2	15/03/2015	1.2	40.4 ±3.6	22.5 ± 1.6	109	7200	7.53 ± 0.48
ML16	J114506.26 + 501802.4	15/03/2015	1.0	40.1 ± 4.0	23.6 ± 1.7	114	7200	6.71 ± 0.07
UM461	J115133.34 − 022221.9	15/03/2015	1.2	40.6 ± 4.0	12.6 ± 0.9	61	6400	6.7 ± 1
N241[a]	J144412.89 + 423743.6	15/03/2015	1.0	40.3 ± 4.0	10.2 ± 0.7	49	6000	6.52 ± 0.07
SBS2104	J210455.31 − 003522.3	16/08/2012	0.5	39.0 ± 2.2	20.1 ± 1.7	97	7200	6.19 ± 0.05
ML32	J230209.98 + 004939.0	16/08/2012	0.5	42 ± 5	138 ± 10	666	7200	8.39 ± 0.33

[a] Target not included in SA+15.
[b] Mean value of the seeing parameter during the observation of each object, measured by RoboDIMM@WHT (http://catserver.ing.iac.es/robodimm/).
[c] Mean FWHM of the telluric lines measured in each spectrum.
[d] Distance and scale at the position of the source, from NED (NASA/IPAC Extragalactic Database).
[e] Total stellar mass of the galaxy from MPA-JHU (Brinchmann et al. 2004; Salim et al. 2007, see SA+15).

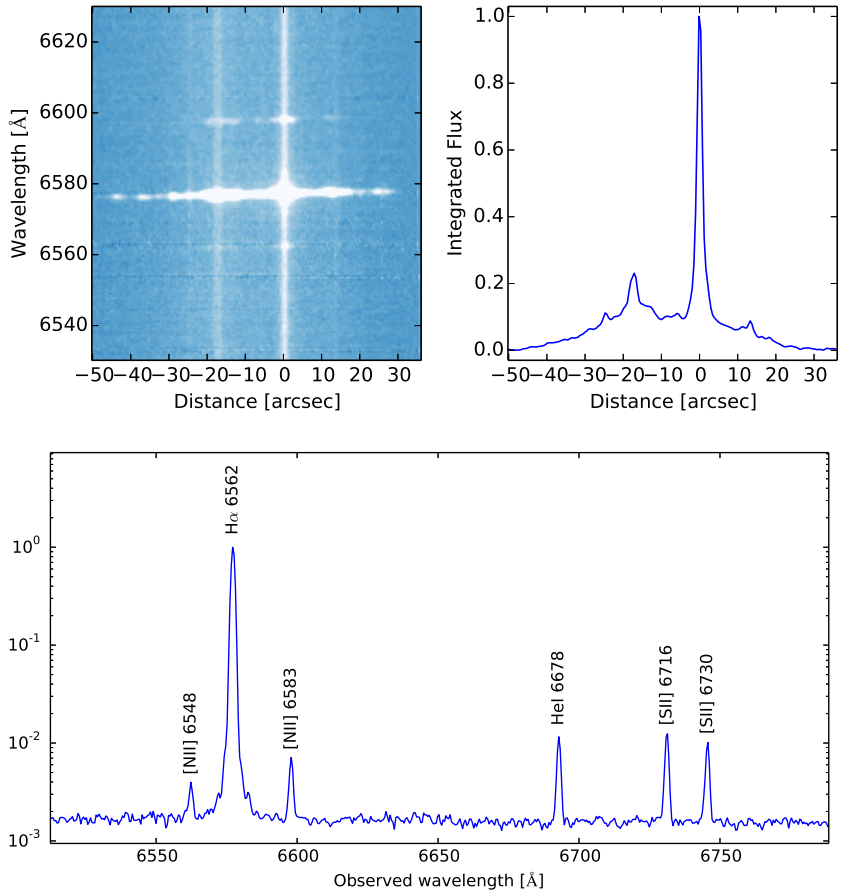

Figure 2.2: Reduced spectrum of the galaxy N241, shown as an example. Top left: 2D representation of the spectrum with the observed wavelength in the vertical axis and the spatial position in the horizontal axis. The three emission lines that appear in the image are Hα and the [NII] doublet. Top right: wavelength-integrated flux normalized to the maximum value. The peak emission traces the the brightest clump in the galaxy, and it defines the origin of the spatial scale. Bottom: spectrum at the brightest clump, in logarithmic units and normalized to the peak Hα emission. The main spectral lines used in this work are labeled.

The spectra from different exposures of the same galaxy were re-aligned before combining them. The left panel in Fig. 2.2 illustrates the final result of the reduction procedure. It contains the spectrum around Hα of the galaxy N241. The signal-to-noise ratio (S/N) in continuum pixels has an average value of approximately 5 in the inner 10 arcsec around the brightest HII region of the galaxy. The S/N in Hα ranges from 200 to 900 at the brightest point in the galaxy, decreasing toward the outskirts. Because our main goal is the kinematic analysis, we only performed a rough flux calibration by comparison with the calibrated Sloan Digital Sky Survey spectra of the galaxies (SDSS DR-12; Alam et al. 2015), re-scaling the flux by accounting for the difference between our 1 arcsec slit and the 3 arcsec diameter of the SDSS fiber. Specifically, the flux integrated over the central 3 arcsec of the galaxies is scaled to be equal to 0.42 times the SDSS flux, where 0.42 is the ratio between the areas covered by the slit and the fiber. SDSS spectra of SBS1 and UM461 are not available. Therefore, we use for calibration the spectra of these galaxies analyzed in SA+15.

Since the photometric calibration is only approximate, we have preferred not to correct the spectra for internal reddening in the HII region. This correction is based on comparing the observed Balmer decrement with its theoretical value (e.g., Emerson 1996), which in practice implies comparing fluxes of spectra taken with the red arm (Hα) and the blue arm (Hβ) of the spectrograph. Rather than carrying out an uncertain correction, we have preferred to neglect the small expected reddening (e.g., Sánchez Almeida et al. 2016). If one uses the SDSS spectra of our targets to estimate the Balmer decrement, the ensuing reddening correction implies increasing Hα by 50 % or less. Neglecting this correction does not modify any of the conclusions drawn in this work.

2.3 Equations used to determine physical parameters

2.3.1 Parameters from the main Hα emission

Mean velocities, velocity dispersions, and rotation curves of the emitting gas are estimated following Sánchez Almeida et al. (2013, Sect. 3), and we refer to this work for details. For the sake of completeness, however, the main assumptions and the resulting equations are provided in the following.

The velocity, U, was calculated from the global wavelength displacement of the Hα emission. It was derived from the centroid of the line, and also from the central wavelength of a Gaussian fitted to the emission line. Both values generally agree with differences $< 1\,\mathrm{km\,s^{-1}}$ in the regions of interest. The error in velocity was estimated assuming the RMS of the continuum variations to be

given by noise, and then propagating this noise into the estimated parameter (e.g., Martin 1971). In the case of the centroid, the expression is analytic. For the Gaussian fit, it is the standard error given by the covariance matrix of the fit (e.g., Press et al. 1986, chapter 14). The spatially unresolved velocity dispersion, W_U, was calculated from the width of the Gaussian model fitted to the line, but also directly from the line profile. We correct the observed FWHM, W_{U0}, for the instrumental spectral resolution, W_{Ui} ($\simeq 40$ km s^{-1}; see Sect. 2.2.1 and Table 2.1), for thermal motions, W_{Ut} ($\simeq 25$ km s^{-1}, corresponding to H atoms at 1.5×10^4 K, a temperature typical of the HII regions in our galaxies; see Table 2.2), and for the natural width of Hα, W_{Un} ($\simeq 7$ km s^{-1}), so that

$$W_U^2 = W_{U0}^2 - W_{Ui}^2 - W_{Ut}^2 - W_{Un}^2. \tag{2.1}$$

The velocity at each spatial pixel along the major axis of the galaxy was fitted with the universal rotation curve by Salucci et al. (2007), i.e.,

$$U(d) = U_0 + U_1 \frac{d - d_0}{\sqrt{\Delta^2 + (d - d_0)^2}}, \tag{2.2}$$

where $U(d)$ stands for the observed velocity at a distance d, U_0 represents the systemic velocity, i.e., the velocity at the dynamic center $d = d_0$, Δ gives a spatial scale for the central gradient of the rotation curve and, finally, U_1 provides the amplitude of the rotational velocity.

The dynamical mass enclosed within a distance d, $M(d)$, follows from the balance between the centrifugal force and the gravitational pull, and it is given by,

$$M(d)\, \sin^2 i = (2.33 \times 10^5\, \mathrm{M}_\odot)\, (d - d_0)\, U^2(d), \tag{2.3}$$

where i stands for the inclination of the disk along the line-of-sight, and where distances are in kpc, and velocities in km s^{-1}. The velocity U in Eq. (2.3) should be the component along the line-of-sight of the circular velocity, $v_c \sin i$. In the case of a purely stellar system, $U/\sin i$ and v_c differ because the stellar orbits are not circular, with the difference given by the so-called asymmetric drift (e.g., Hinz et al. 2001; Binney & Tremaine 2008). In our case, where the velocity of the gas is measured, they also differ because gas pressure gradients partly balance the gravitational force, and this hydro-dynamical force has to be taken into account in the mechanical balance (e.g., Dalcanton & Stilp 2010). In a first approximation (e.g., Dalcanton & Stilp 2010; Read et al. 2016),

$$v_c^2 \simeq U^2/\sin^2 i + 0.06\, W_U^2\, (d - d_0)/R_\star, \tag{2.4}$$

Table 2.2: Physical parameters for the main star-forming region in the galaxies.

ID	HII size [arcsec]	$L_{H\alpha}$ [10^{38} erg s^{-1}]	SFR [$M_\odot$ yr^{-1}]	$\langle 12 + \log(O/H) \rangle$ [a]	$\langle T_e \rangle$ [a] [10^4 K]	$\langle n_e \rangle$ [b] [cm^{-3}]	R_e [c] [kpc]	W_U [d] [km s^{-1}]	$\log M_{dyn,turb}$ [e] [$M_\odot$]
ML4	1.4	30 ± 4	0.016 ± 0.002	7.76 ± 0.06	1.57	13	0.435 ± 0.012	62 ± 2	8.3 ± 0.03
HS0822	1.1	1.9 ± 0.3	0.00101 ± 0.00015	7.69 ± 0.07	1.56	38	0.027 ± 0.006	36 ± 2	6.61 ± 0.1
SBS0	1.0	7.1 ± 1	0.0038 ± 0.0005	7.63 ± 0.06	1.67	129	0.052 ± 0.011	38 ± 3	6.95 ± 0.12
SBS1	1.1	2.3 ± 0.3	0.00121± 0.00017	7.61 ± 0.09	1.44	84	0.059 ± 0.018	51 ± 3	7.27 ± 0.14
ML16	2.4	7.5 ± 1.1	0.004 ± 0.0006	7.92 ± 0.04	1.46	48	0.139 ± 0.005	35 ± 5	7.3 ± 0.12
UM461	1.2	1.32 ± 0.19	0.00071 ± 0.0001	7.38 ± 0.09	2.47	212	0.036 ± 0.009	42 ± 4	6.88 ± 0.14
N241	1.4	87 ± 13	0.047 ± 0.007	7.11 ± 0.28 [f]	1.5 [g]	73	0.035 ± 0.003	48 ± 3	6.99 ± 0.07
SBS2104	1.4	4.1 ± 0.7	0.0022 ± 0.0004	7.48 ± 0.08	1.58	113	0.069 ± 0.002	18 ± 5	6.4 ± 0.2
ML32	1.3	190 ± 30	0.103 ± 0.015	7.7 ± 0.05	1.68	13	0.434 ± 0.013	55 ± 4	8.19 ± 0.06

[a] Mean value taken from SA+15.
[b] Inferred from the ratio between [SII]λ6716 and [SII]λ6731 (e.g., Osterbrock 1974).
[c] Half-light radius of the clump, measured from the FWHM of the Hα flux distribution.
[d] Velocity dispersion of the clump, calculated from the Hα line of the clump-integrated spectra.
[e] Dynamical mass of the clump from Eq. (2.5). Errors do not include the uncertainty in the thermal motion subtraction.
[f] From Sánchez Almeida et al. (2016).
[g] Assumed to be similar to the value in the other objects.

where the coefficient that gives the correction has been inferred assuming the gas density to drop exponentially with the distance to the center ($|d - d_0|$), with a length scale around three times the length scale of the stellar disks $R_\star$. This difference between the gaseous and the stellar disk is typical of XMPs (Filho et al. 2013). Since $|d - d_0| \sim R_\star$, Eq. (2.4) predicts that even for a large turbulent velocity ($W_U \simeq U/\sin i$), the difference between v_c and $U/\sin i$ is small. Since we do not know the inclination angle of the galaxies, we cannot apply the correction for pressure gradients in Eq. (2.4). Thus, we employ U in Eq. (2.3), knowing that the resulting dynamical masses slightly underestimate the true masses in an amount given by $W_U/\sin i$ and Eq. (2.4).

Our targets have distinct star-forming regions (see Fig. 2.1), also denoted here as star-forming clumps or starbursts. I refer to the brightest clump in each galaxy as the *main* star-forming region, to be distinguished from other fainter clumps that appear in some galaxies. They have been highlighted in Fig. 2.1. The dynamical masses of the individual star-forming clumps are calculated from the velocity dispersion, assuming virial equilibrium,

$$M_{\rm dyn,turb} = (1.20 \times 10^5\,{\rm M}_\odot)\ R_e\,{W_U}^2. \tag{2.5}$$

The half-light radius, R_e, is calculated as in SA+15, from the FWHM of a 1D Gaussian fitted to the Hα flux of the star-forming clump, which is subsequently corrected for seeing (Table 2.1). W_U in Eq. (2.5) is calculated from the Hα line resulting from integrating all the spectra along the spatial axis, from $-R_e$ to $+R_e$, with the interval centered at the clump. R_e in Eq. (2.5) is given in kpc, and W_U in km s^{-1}. The use of W_U to estimate dynamical masses implies excluding thermal motions in the virial equilibrium equation (Eq. [2.1]). This approximation may be more or less appropriate depending on the structure of the velocity field in the emitting gas. In practice, however, thermal motions are always smaller than W_U, so that including them does not significantly modify the masses estimated through Eq. (2.5).

Our long-slit spectra only provide cuts across the star-forming regions. In order to obtain the total luminosity, $\pounds_{\rm H\alpha}$, we assume the region to be circular, with a radius R_e. Then the flux obtained by integrating the observed spectra from $-R_e$ to $+R_e$, $F_{\rm H\alpha}$, is corrected according to the ratio between the observed area, $2\,R_e \times 1$ arcsec, and the circular area, $\pi\,R_e^2$, which renders

$$\pounds_{\rm H\alpha} = 2\pi^2\,D^2\,\frac{R_e}{1\ {\rm arcsec}}\,F_{\rm H\alpha}, \tag{2.6}$$

with D the distance to the source. We take D from NED, as listed in Table 2.1. SFRs are inferred from $\pounds_{\rm H\alpha}$ using the prescription by Kennicutt & Evans (2012) to be given in Eq. (2.20).

2.3.2 Characterization of the secondary components in the wings of Hα

When the S/N is sufficiently good, the observed Hα profiles show faint broad emission, often in the form of multiple pairs of separate emission-line components (see Fig. 2.3). The existence of pairs of components is particularly interesting from a physical standpoint, since they may reveal the feedback of star formation on the surrounding medium, or the presence of a black hole (BH; to be discussed in Sect. 2.5.2).

In order to determine the properties of the secondary lobes (number, wavelength shifts, relative fluxes, etc.), we performed a multi-Gaussian fit to Hα using the Python package LMFIT (Newville et al. 2014). The fitting is not unique unless the free parameters are constrained, which we do by attempting to reproduce Hα in the brightest pixel of the galaxy as a collection of discrete components, with widths similar to that of the central component. The procedure is detailed below. Several examples of the fit in various S/N conditions are given in Fig. 2.3. We initialize the fit in the spatial pixel with highest S/N in continuum, where the secondary components clearly stand out. This pixel corresponds to the brightest star-forming region of the galaxy (the bright blue knots in Fig. 2.1). Then the rest of the pixels are fitted, using as starting values the free parameters obtained in the fit to the adjacent pixel. The number of secondary components is set at the central brightest pixel, where the S/N needed to detect them is highest, and we fix this number for each galaxy. In order to follow each component across the spatial direction, we put two constraints on their spatial variation, namely, (1) the center does not deviate from the previous value by more than twice the wavelength sampling ($\sim$1 Å), and (2) the velocity dispersion is bound between a minimum set by the spectral resolution, and twice the value in the previous pixel. These constraints implement the fact that neighbouring pixels are not independent, since our sampling grants at least two pixels per spatial resolution element. As a sanity check, we verified that the constraint on the center of the components does not affect the inferred velocities. The maximum wavelength displacement between two adjacent pixels for all secondary components in the clumps is approximately half the wavelength sampling. Although the S/N decreases with the distance to the brightest pixel, we checked that each detected secondary component has signal at least twice the noise in continuum in all the spectra used to characterize the star-forming regions.

The uncertainties in each parameter can be derived from the covariance matrix of the fit (e.g., Press et al. 1986). However, when the fitted parameters are near the values set by the constraints, the covariance matrix cannot be

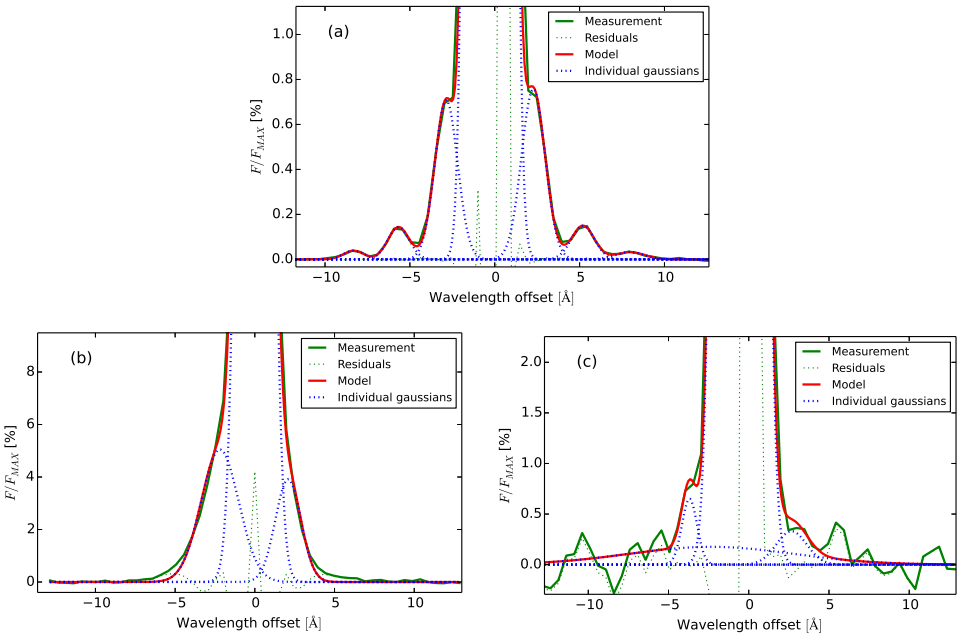

Figure 2.3: Hα line with the central component saturated to be able to distinguish the secondary components. (a) Hα line at the bright core of the galaxy UM461. The observed spectrum (the green solid line) clearly shows seven components: the central one plus three pairs. Our fit reproduces the observation very well (the red solid line) as a superposition of Gaussian functions of various amplitudes, widths, and shifts (the blue dotted lines). The residuals of the fit are also included as the green dotted line. (b) Hα at the bright core of the galaxy SBS1, where the components are not very well separated in wavelength. (c) Hα at a bright spot of N241, which portrays a case where the S/N is poor compared to the previous cases. The wavelengths are referred to the centroid of the main component, and the fluxes are given in % relative to the maximum flux of the Hα profile. Each spectrum corresponds to a single spatial pixel.

computed and the uncertainties provided by the Python routine turn out to be unreliable. Therefore, errors are estimated running a MonteCarlo simulation. The best fit profile is contaminated with random noise having the observed S/N. This simulated observation is processed as a true observation, and the exercise is repeated 80 times with independent realizations of the noise. The RMS fluctuations of the parameters thus derived are quoted as 1-sigma errors.

2.3.3 Mass loss rates

In order to estimate the mass, the mass loss rate, and the kinetic energy corresponding to the secondary components observed in the wings of Hα (Fig. 2.3), we follow a procedure similar to that described in Carniani et al. (2015). It is detailed here both for completeness, and to tune the approach to our specific needs.

We assume that the small emission-line components in the wings of the main Hα profile are produced by the recombination of H. Then the luminosity in Hα, $L_{\mathrm{H}\alpha}$, is given by,

$$L_{\mathrm{H}\alpha} = \int f\, n_e\, n_p\, j_{\mathrm{H}\alpha}\, dV, \tag{2.7}$$

where the integral extends to all the emitting volume, and n_e, n_p, and $j_{\mathrm{H}\alpha}$ represent the number density of electrons and protons, and the emission coefficient, respectively. The symbol f stands for a local filling factor that accounts for a clumpy medium, so that only a fraction f is contributing to the emission. In a tenuous plasma, the emission coefficient is given by (Osterbrock 1974; Lang 1999),

$$j_{\mathrm{H}\alpha} \simeq 3.56 \times 10^{-25}\, t_4^{-1} \ \ \mathrm{erg\,cm^3\,s^{-1}}, \tag{2.8}$$

where t_4 is the temperature in units of 10^4 K. The mass of emitting gas turns out to be,

$$M_g = \int f\, m_{\mathrm{H}}\, n_{\mathrm{H}}\, X^{-1}\, dV, \tag{2.9}$$

where n_{H} is number density of H (neutral and ionized), m_{H} stands for the atomic mass unit, and X is the fraction of gas mass in H. If the gas is fully ionized[5] ($n_{\mathrm{H}} = n_p$), and the electron temperature and the H mass fraction are constant, then Eqs. (2.7), (2.8) and (2.9) render,

$$M_g = \frac{m_{\mathrm{H}}\, L_{\mathrm{H}\alpha}}{X\, j_{\mathrm{H}\alpha}\, \langle n_e \rangle_1}, \tag{2.10}$$

[5] If it is not, then M_g and the other parameters inferred from this mass refer to the mass of ionized gas.

with the mean electron density defined as,

$$\langle n_e \rangle_1 = \frac{\int f\, n_p\, n_e\, dV}{\int f\, n_p\, dV}. \tag{2.11}$$

Using astronomical units, and assuming $X = 0.75$ (which corresponds to the solar composition; e.g., Asplund et al. 2009), Eq. (2.10) can be written as

$$M_g = 3.15 \times 10^3\, \mathrm{M}_\odot\; t_4\, \frac{L_{\mathrm{H}\alpha}/10^{38}\,\mathrm{erg\,s^{-1}}}{\langle n_e \rangle_1 / 10^2\,\mathrm{cm^{-3}}}. \tag{2.12}$$

Assume that the motions associated with the weak emission-line components in the wings of the main profile trace some sort of expansion. The mass loss rate, $\dot{M}_g$, is defined as the total mass carried away per unit time by these motions. It can be computed as the flux of mass across a closed surface around the center of expansion,

$$\dot{M}_g = \int f\, \rho_g\, \mathbf{v} \cdot \mathbf{d\Sigma}, \tag{2.13}$$

where ρ_g is the gas density at the surface and $\mathbf{v}$ represents the velocity of the flow. Assuming that motions are radial, and that the density and filling factor are constant at the surface, the previous integral can be simplified considering a spherical surface of radius R,

$$\dot{M}_g = 4\pi\, R^2\, f\, \rho_g v_{\mathrm{out}}, \tag{2.14}$$

with the radial speed $v_{\mathrm{out}} = |\mathbf{v}|$. If the moving mass forms a shell of width ΔR (Fig. 2.4), then $M_g = 4\pi\, R^2\, f \rho_g\, \Delta R$, so that the mass loss rate turns out to be

$$\dot{M}_g \simeq M_g\, v_{\mathrm{out}}\, \Delta R^{-1}. \tag{2.15}$$

If the moving mass is distributed on a sphere, then $M_g = 4\pi\, R^3\, f\rho_g/3$, and the mass loss rate is still given by Eq. (2.15) provided that $\Delta R/R \simeq 1/3$. In other words, by using $\Delta R/R \simeq 0.3$ in Eq. (2.15) one approximately considers the full range of geometries between shells and spheres (for further discussion on the assumptions made to estimate $\dot{M}_g$ see, e.g., Maiolino et al. 2012; Keller et al. 2014; or Carniani et al. 2015).

Once the expanding shell geometry has been assumed, the radius of the shell is set by the gas mass and the electron density, since Eq. (2.9) can be written as,

$$M_g \simeq \frac{8\pi\, m_H}{1+X}\, \langle n_e \rangle_2\, \langle f \rangle_3\, R^2\, \Delta R, \tag{2.16}$$

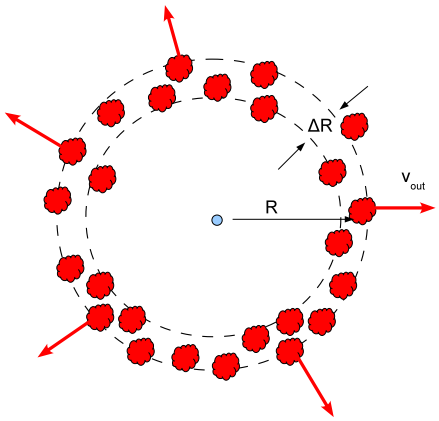

Figure 2.4: Schematic of the geometry used to estimate mass loss rates. The gas is represented in red as clumps which do not fill the full space. The schematic includes the characteristic length-scales, size (R) and width (ΔR), and expansion velocity ($v_{\rm out}$). The blue dot points out the center of expansion.

with the mean values given by

$$\langle n_e \rangle_2 = \frac{\int f\, n_e\, dV}{\int f\, dV},$$

$$\langle f \rangle_3 = \frac{\int f\, dV}{\int dV}.$$

Equation (2.16) assumes the gas to be composed of fully ionized H and He, so that

$$n_e \simeq n_{\rm H} + 2n_{\rm He} \simeq n_{\rm H} \frac{1+X}{2X}, \tag{2.17}$$

which is a reasonable estimate considering that we are dealing with metal-poor gas, such that the metals do not contribute to the electron density. Equation (2.16) provides a way to estimate the size of the emitting region in terms of the electron density, the filling factor, and the relative width of the shell, explicitly,

$$\left[\frac{R}{14.7\ {\rm pc}}\right]^3 = \left[\frac{M_g}{10^4\ {\rm M}_\odot}\right]\left[\frac{\langle n_e \rangle_2}{10^2\ {\rm cm}^{-3}}\frac{\langle f \rangle_3}{0.3}\frac{\Delta R/R}{0.3}\right]^{-1}. \tag{2.18}$$

The expansion velocity and the radius allow us to estimate the age of the expanding shell, or the time-lag from blowout,

$$Age = R/v_{\rm out}, \tag{2.19}$$

where $v_{\rm out}$ is assumed to be constant in time. Since the expansion decelerates, *Age* in Eq. (2.19) represents an upper limit to the true age.

A convenient (and intuitive) way of expressing the mass loss rate in Eq. (2.15) is re-writing the expression in terms of the Star Formation Rate (SFR) estimated using the prescription by Kennicutt & Evans (2012)[6],

$$\frac{\rm SFR}{1{\rm M}_\odot{\rm yr}^{-1}} \simeq \frac{\pounds_{\rm H\alpha}}{1.86\times10^{41}\,{\rm erg\,s^{-1}}}, \tag{2.20}$$

which depends only on the total Hα flux of the region, $\pounds_{\rm H\alpha}$. We parameterize the Hα flux in a weak emission-line component, $L_{\rm H\alpha}$, in terms of total Hα flux,

$$L_{\rm H\alpha} = \varepsilon \pounds_{\rm H\alpha}, \tag{2.21}$$

with ε the scaling factor inferred from the fits described in Sect. 2.3.2. We do not correct $\pounds_{\rm H\alpha}$ for extinction in Eq. (2.20) because the photometric calibration needed to infer it from the Balmer decrement is uncertain (Sect. 2.2.2), because the main Hα lobe and the weak emission components do not necessarily have the same extinction, and because the expected extinction is very low (reddening coefficient around 0.1; Sánchez Almeida et al. 2016). Using Eqs. (2.20) and (2.21), Eq. (2.15) can be expressed as

$$\frac{\dot{M}_g}{\rm SFR} \simeq 0.20 \frac{\varepsilon}{10^{-3}} \frac{v_{\rm out}}{10^2\,{\rm km\,s^{-1}}}\, t_4 \left[\frac{\Delta R}{3\,{\rm pc}}\,\frac{\langle n_e\rangle_1}{10^2\,{\rm cm^{-3}}}\right]^{-1}. \tag{2.22}$$

Another important parameter derived from the gas mass and velocity is the kinetic energy involved in the outflow,

$$E_k = \frac{1}{2} M_g\, v_{\rm out}^2 \simeq 10^{51}\,{\rm erg}\,\frac{M_g}{10^4\,{\rm M}_\odot}\left[\frac{v_{\rm out}}{10^2\,{\rm km\,s^{-1}}}\right]^2. \tag{2.23}$$

The equation has been written in units of 10^{51} erg, which is the typical kinetic energy released in a core-collapse supernova (SN; e.g., Leitherer et al. 1999; Kasen & Woosley 2009), corresponding to the explosion of a massive star.

This energy range is also within reach of accreting BH of intermediate mass, like the direct collapse 10^5 M$_\odot$ BH seeds needed to explain the existence of super-massive BHs in the early Universe (e.g., Volonteri 2010; Ferrara et al. 2014; Pacucci et al. 2016). Assuming that the BH releases kinetic energy at a fraction of the Eddington limit, ψ, and that the accretion event has a duration, Υ, then

$$E_{BH} \simeq 10^{51}\,{\rm erg}\,\frac{\psi}{0.1}\,\frac{\Upsilon}{25\ {\rm yr}}\,\frac{M_{BH}}{10^5\,{\rm M}_\odot}, \tag{2.24}$$

with M_{BH} the BH mass (e.g., Frank et al. 2002).

[6]This SFR is 30% smaller than the classical value in Kennicutt (1998).

2.3.4 Mass of the central object

In principle, the observed faint emission-line pairs in the wings of Hα might also be generated in a rotating disk around a massive object (e.g., Epstein 1964). Then the approximation used to estimate the radius of the shell in Eq. (2.18) still holds, except that

$$\Big[\frac{R}{27.6\ \mathrm{pc}}\Big]^3 = \Big[\frac{M_g}{10^4\,\mathrm{M}_\odot}\Big]\Big[\frac{\langle n_e\rangle_2}{10^2\,\mathrm{cm}^{-3}}\frac{\langle f\rangle_3}{0.3}\frac{\Delta R/R}{0.3}\frac{\Delta z/R}{0.3}\Big]^{-1}, \tag{2.25}$$

where ΔR represents the difference between the inner and outer radii, and Δz stands for the thickness of the disk. This size, together with the circular velocity, v_c, directly inferred from the spectra, allow us to estimate the mass of the central object, $M_\bullet$, from the balance between gravity and centrifugal force,

$$M_\bullet \simeq 7.0\times10^7\,\mathrm{M}_\odot\,\frac{R}{30\,\mathrm{pc}}\Big(\frac{v_c}{10^2\,\mathrm{km\,s}^{-1}}\Big)^2. \tag{2.26}$$

2.4 Rotation, turbulent motions, and chemical properties

Figure 2.5 shows the rotation curve of all the galaxies analyzed in this study. It represents the velocities inferred from the Gaussian fit, but the results are similar when using centroids (Sect. 2.3.1). Most galaxies seem to rotate, although HS0822 and SBS0 do not. The rotation curve of UM461 may suggest some rotation, but it may also be compatible with the absence of rotation. The difficulty in detecting rotation in UM461 could be due to projection effects; UM461 appears face-on in the SDSS image, with the galaxy showing a rounded faint envelope enclosing its two bright knots (Fig. 2.1). All rotation curves present small-scale velocity irregularities, often with an amplitude comparable to the velocity gradient across the whole galaxy. The rotation of the galaxies ML4, SBS1, N241 is clear, whereas other galaxies are more affected by these small-scale irregularities. Galaxies SBS2104 and ML32 could host counter-rotating components, like those found in tadpole galaxies by Sánchez Almeida et al. (2013), although, in this case, the center of the counter-rotating structure does not match the main star-forming region. Figure 2.6 shows the FWHM velocity dispersion inferred from Hα. Typical values at the position of the main starburst are between 20 and 60 $\mathrm{km\,s}^{-1}$ (Table 2.2). We note that the regions with possible counter-rotating components also show an increase in the velocity dispersion: c.f., Figs. 2.5 and 2.6 for SBS2104 ($d \simeq 4$ arcsec) and ML32 ($d \simeq 2$ arcsec).

We fitted the universal rotation curve by Salucci et al. (2007), given in Eq. (2.2), to the observed velocities. The four free parameters of the non-linear

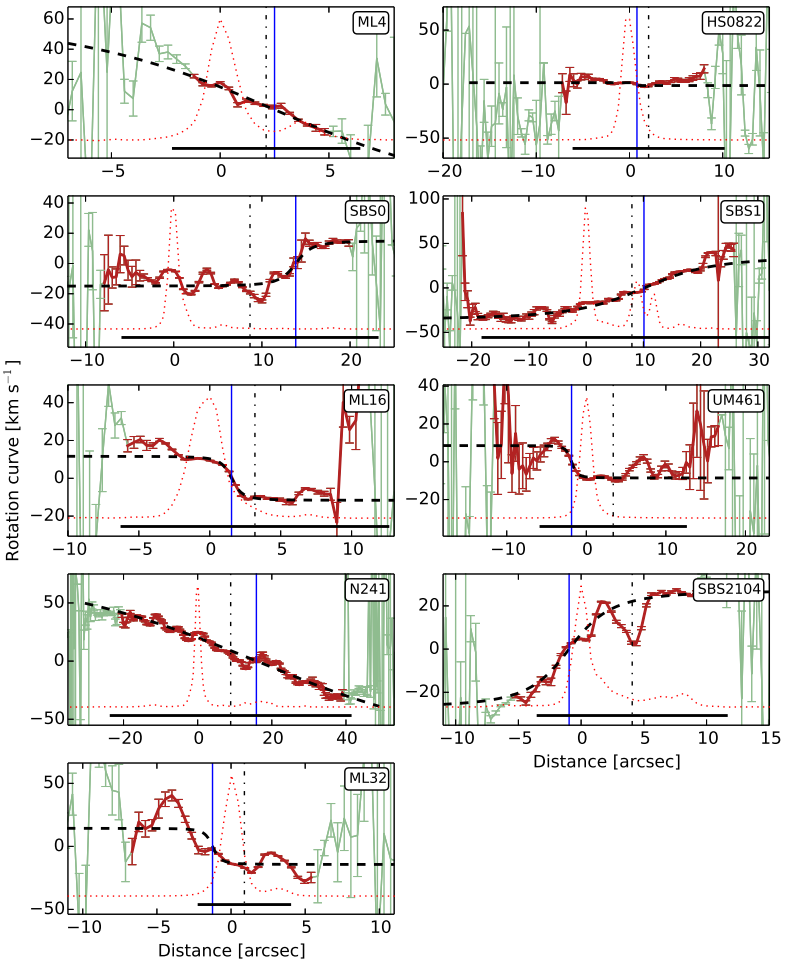

Figure 2.5: Rotation curves for the XMPs, i.e., velocity versus position along the slit. The velocities were derived using a Gaussian fit to the Hα line profile. The actual observed points show error bars joined by a continuous line, which is either green or red, depending on whether the S/N of the spectra in the continuum is smaller (green) or larger (red) than one. Only the points in red have been used to fit the universal rotation curve, shown as the black dashed line, with the vertical blue line identifying the position of the dynamical center inferred from the fit. The zero of the velocity scale is set by the fit at the dynamical center. The red dotted line represents the Hα flux scaled from zero to the maximum value. Distances are referred to the point with largest Hα flux. The horizontal solid black line gives the galaxy diameter, inferred from the 25 mag arcsec^{-2} isophote, and provided by NED. It is centered in the photometric midpoint marked by the vertical dotted-dashed line.

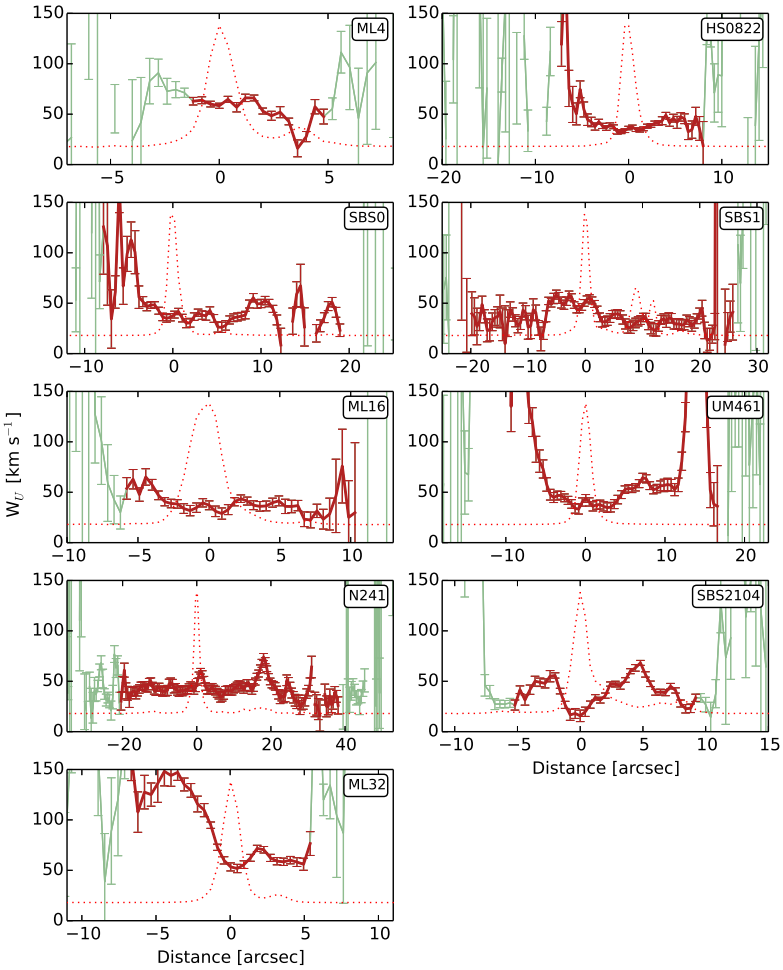

Figure 2.6: Similar to Fig. 2.5 with the FWHM velocity dispersion. The range in abscissas is the same as in Fig. 2.5.

fit (U_0, U_1, d_0, and Δ) were derived using the Python package LMFIT (Newville et al. 2014). The fits are shown as black dashed lines in Fig. 2.5. The fits are not particularly good, but they allow us to have an idea of the amplitude of the rotation curve and the dynamical center of the galaxies. These properties are summarized in Table 2.3. Even though the position of the dynamical center is very uncertain (see Fig. 2.5), they do not seem to overlap with the position of the main star-forming region.

Independently of the properties of the rotation, we do find a recurrent behavior for the velocity and velocity dispersion at the star-forming region. The velocity tends to be constant within the spatial extent of the clump. This is clear in, e.g., SBS2104 and ML16 (see the velocity curves in Fig. 2.5 at the point where the Hα emission peaks). If the spatial resolution of the observations were insufficient to resolve the individual clumps, then one would expect that the velocity, and all the other properties inferred from the shape of the Hα line, would be constant within the spatially unresolved clump. However, insufficient spatial resolution is not responsible for the observed behavior for two reasons: (1) many clumps are well resolved; e.g., ML16 has a FWHM of 3 arcsec (Fig. 2.5) when the seeing was only 1 arcsec FWHM (Table 2.1), and (2) the velocity dispersion is not constant within the starburst clump (see Fig. 2.6).

These two properties, i.e., constant velocity with varying velocity dispersion, are clearer in Fig. 2.7. It shows the Hα flux across all the clumps of the individual galaxies (the dotted lines in all the panels). They have been re-scaled in abscissa and ordinate so that all of the Hα flux profiles look approximately the same in this representation (we normalize each profile to its maximum flux and to its size). The figure also includes the rotation curve around the star-forming region (bullet symbols and solid lines), once the average velocity in the region has been removed. Note that all rotation curves tend to flatten at the location of the star-forming clump. The velocity is uniform, as if the star-forming region were a kinematically distinct entity. Note also how the velocity dispersion (shown as asterisks joined by solid lines in Fig. 2.7) varies across the clump. Three patterns for the variation of the velocity dispersion can be distinguished, namely, the velocity dispersion has a local maximum coinciding with the center of the star-forming clump (Fig. 2.7, top panel; Type 1), the velocity dispersion increases across the clump (Fig. 2.7, middle panel; Type 2), and the velocity dispersion presents a minimum at the center of the clump (Fig. 2.7, bottom panel; Type 3).

The first case may be qualitatively understood if the star-forming region is undergoing a global expansion. The velocity dispersion peaks in the central part, where the Doppler signal of the approaching and receding parts is largest.

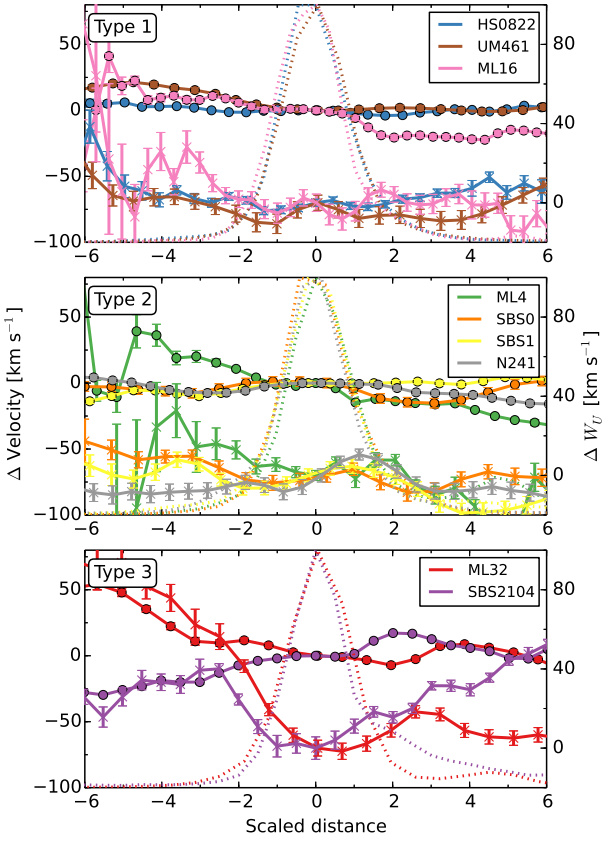

Figure 2.7: Variation of the velocity (bullet symbols) and velocity dispersion (asterisks) across the star-forming regions of the XMPs. Distances, in the abscissa axis, are referenced to the position of the star-forming region and normalized to its size. For this reason, the variation of the Hα flux across the region, shown as dotted lines, is always centered at distance zero, and always has the same width. The velocity turns out to be constant within the star-forming clump, whereas the velocity dispersion follows three distinct patterns, labelled as Type 1 (shown in the top panel), Type 2 (middle panel), and Type 3 (bottom panel). In Type 1, the dispersion presents a local maximum at the center of the starburst. In Type 2, however, the dispersion increases across the region towards the position that is closest to the galaxy photometric center. The Type 3 pattern presents a minimum at the center of the star-forming region. Different colors refer to different galaxies, as indicated by the insets. The monikers used for the XMPs are in Table 2.1. The average velocity and velocity dispersion in each star-forming clump have been subtracted from the plots, so that the velocity and velocity dispersion are zero at the clump.

In this instance, the velocity remains constant, tracing the rotational velocity at the origin of expansion[7]. The difference between the velocity dispersion at the center and at the sides of the starburst can be used to estimate the expansion velocity of the region. If the difference is of the order of 20 %, and W_U is around 40 km s^{-1} (see HS0822, UM461, and ML16 in Table 2.2), then an expansion able to create the observed excess of central velocity dispersion has to be of the order of 13 km s^{-1}. We have assumed that the turbulent and expansion velocity add up quadratically in their contribution to W_U. The mass loss rate resulting from the possible global expansion is worked out in Sect. 2.6.

In the second case (Type 2; Fig. 2.7), the dispersion always increases towards positive distances which, by construction, point to the photometric center of the galaxies. In other words, it is largest in the part of the star-forming clump that is closest to the galaxy center. As we discussed above, this is not an observational bias due to insufficient spatial resolution. Although we can only speculate at this point, the result is very suggestive. The excess velocity dispersion in the center-side of Types 2 may indicate an intensification of the turbulence of the gas in that particular part of the starburst. Such an increase may indicate the collision of the starburst gas with the ISM of the host galaxy, as if the star-forming regions were inspiraling towards the galaxy center. This migration to the galaxy center is expected from tidal forces acting upon massive gas clumps (see, e.g., Elmegreen et al. 2008; Ceverino et al. 2016; Hinojosa-Goñi et al. 2016); the large starbursts in our XMPs may be going through such a process at this moment.

The Type 3 pattern presents a minimum velocity dispersion, coinciding with the starburst (Fig. 2.7); it may reflect the past expansion of the region. As an adiabatic contraction increases the turbulence in a contracting medium (e.g., Murray & Chang 2015), an expansion leads to adiabatic cooling and to a drop of the turbulence (e.g., Robertson & Goldreich 2012). A past expansion phase may have produced the observed decrease in velocity dispersion, even if the phase is already over and it does not appear in the form of a Type 1 pattern. The same kind of local minima in velocity dispersion has been observed in young star cluster complexes of nearby galaxies (e.g., Bastian et al. 2006).

We have calculated the dynamical mass that accounts for the velocity dispersion if the clump was in virial equilibrium, as described by Eq. (2.5). The results are in Table 2.2. They are similar to the total stellar mass of the galaxy and thus, very large. They are also comparable to the dynamical mass of the galaxy inferred from the rotation curve (Table 2.3), even though these masses

[7]Even if the original region had some rotation, it would have been washed out by the expansion, due to angular momentum conservation.

are lower limits because of the (unknown) inclination of the galaxies, and because of the existence of pressure gradients (see the discussion in Sect. 2.3).

The fact that the star-forming regions have well defined kinematical properties, suggests that they are distinct entities within the host galaxy.

Table 2.3: Properties of the rotation curve.

ID	U_1 [a] [$\mathrm{km\,s^{-1}}$]	d_0 [b] [arcsec]	$\log(M \sin^2 i)$ [c] [$\mathrm{M_\odot}$]	$\lvert d_l - d_0 \rvert$ [c] [arcsec]
ML4	-70 ± 200	2 ± 2	8.4	3.7
HS0822	-1.3 ± 0.2	0.8 ± 80	5.2	7.5
SBS0	15 ± 1.2	13.8 ± 0.5	8.1	21.7
SBS1	36 ± 4	10.1 ± 0.08	9.0	31.7
ML16	-11.7 ± 0.7	1.53 ± 0.09	7.4	7.6
UM461	-8.6 ± 0.7	-1.85 ± 0.08	7.2	13.4
N241	-90 ± 50	16 ± 10	9.0	40.8
SBS2104	27 ± 8	-1 ± 0.9	8.2	10.2
ML32	-14 ± 7	-1.2 ± 0.4	8.3	6.6

[a] Amplitude resulting from fitting Eq. (2.2) to the observed rotation curve.
[b] Dynamical center resulting from fitting Eq. (2.2) to the observed rotation curve.
[c] Dynamical mass of the galaxy. Based on Eq. (2.3), considering up to the largest distance from d_0 with sensible velocity measurements, $\mathrm{d_l}$.

2.4.1 Chemical properties

A separate, but important, result from the analysis of the spectra deals with the metallicity. Most of the XMPs that we study are characterized by having a drop in gas-phase metallicity associated with the main starburst (SA+15). We searched for possible relationships between such metallicity inhomogeneities and the kinematic properties described above but found no correlation. What we found, however, is a notable lack of correlation between the metallicity (as traced by O/H) and the ratio N/O. It appears in Fig. 2.8, where the variation of the metallicity, SFR and N/O ratio is displayed. The N/O ratio was estimated from [NII]λ5583 and [SII]λ6716,6731 following the calibration by Pérez-Montero & Contini (2009), which is almost independent of dust reddening (it could not be estimated in SA+15 because of the difficulty in separating [NII] from Hα, given the limited wavelength resolution of those spectra). Figure 2.8 shows that the N/O ratio remains fairly constant along the galaxy, even at the position of the main starbursts, where the Hα flux peaks and the metallicity drops. The lack of correlation between the ratios N/O and O/H is the general behavior. This observational fact is consistent with the gas accretion scenario.

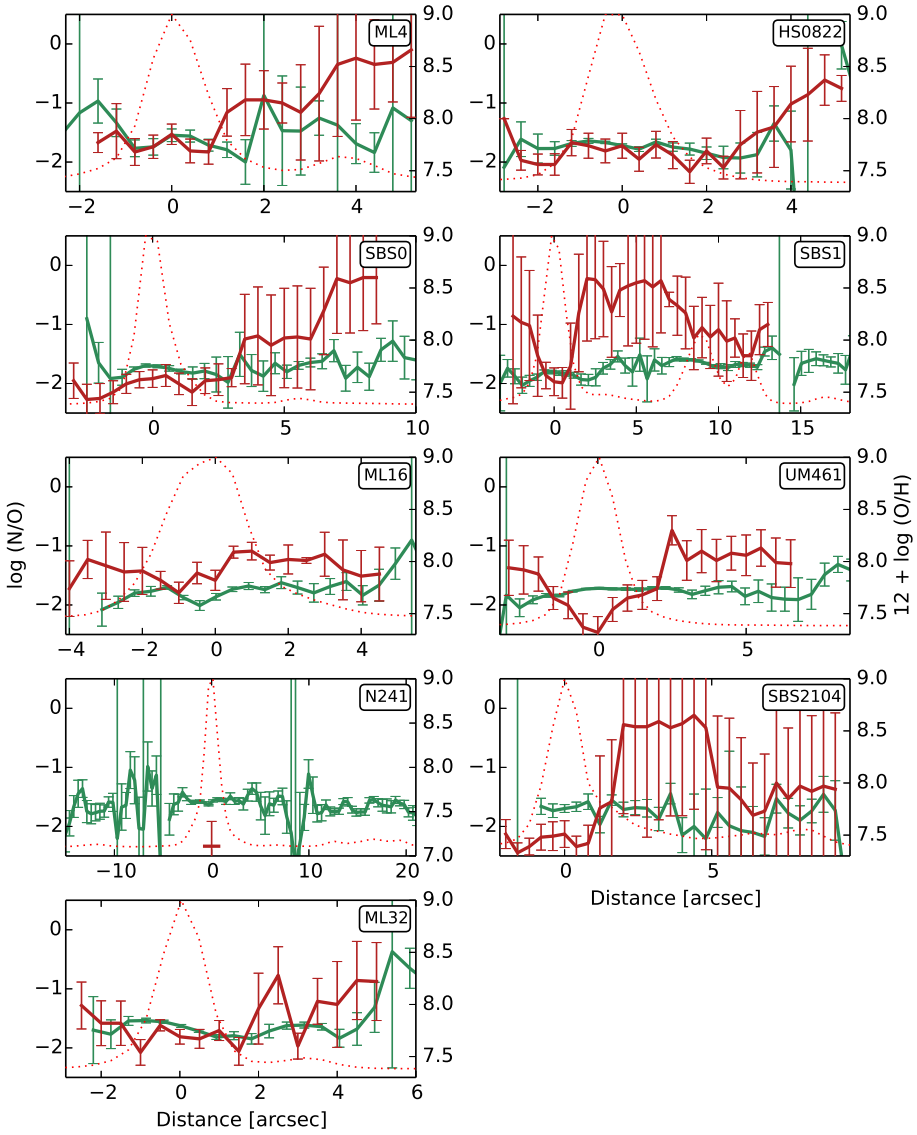

Figure 2.8: Variation of the metallicity ($12 + \log[O/H]$), N/O ratio, and SFR along the major axis of the XMPs. The red solid line is the metallicity of the galaxy from SA+15, except for N241, where a mean value for the clump was obtained from Sánchez Almeida et al. (2016). The green solid line is the variation of the N/O ratio. The red dotted line represents the Hα flux scaled to the maximum value at the clump, which is a proxy for SFR.

If the accretion of metal-poor gas is triggering the observed starburst, then the fresh gas would locally reduce the O/H ratio in the star-forming region relative to the rest of the galaxy. However, mixing with external gas cannot modify the pre-existing ratio between metals, leaving the N/O ratio unchanged. This argument has been put forward before to support the gas accretion scenario (Amorín et al. 2010, 2012; Sánchez Almeida et al. 2014a). The value for log(N/O) that we infer, around -1.5, is also consistent with the N/O ratio found in metal-poor $\alpha-$enhanced stars in the solar neighborhood (e.g., Israelian et al. 2004; Spite et al. 2005). Since the star formation is enhanced where the O/H ratio drops, the lack of correlation between the ratios N/O and O/H reveals a lack of correlation between N/O and the SFR. This property seems to be common among star-forming galaxies at all redshifts (e.g., Pérez-Montero et al. 2013), and supports the metal-poor nature of the gas that forms stars.

2.5 Properties of the multiple components

2.5.1 Expanding shell interpretation

The first significant result is the mere existence of multiple components in the wings of Hα, which are often paired, so that for each red component there is a blue component with a similar wavelength shift and amplitude (see the example in Fig. 2.3a). This fact discards spatially-unresolved, optically-thin, uniform expanding shells as the source of emission in the line wings, since they produce a top-hat line profile without individual emission peaks (e.g., Zuckerman 1987; Cid Fernandes & Terlevich 1994; Tenorio-Tagle et al. 1996, and also Appendix 2.8). However, the two-hump emission can be caused by a non-spherically-symmetric shell, or a shell having internal absorption (the other alternatives are analyzed and discarded in Sect. 2.5.2). Even though the observed amplitudes are similar, the blue component of each pair tends to be larger than the red component. Figure 2.9 shows the ratio between the area of the red and the blue components, and in all but one case, this ratio is one or smaller, considering error bars. Moreover, if one of the components is missing, it tends to be the red one. These two facts suggest a dusty expanding shell model, where the receding cap of the shell is obscured by the approaching cap (see Appendix and Fig. 2.17). These issues are discussed in detail in Sect. 2.5.2. The color code employed in Figs. 2.9 — 2.15 assigns a color to each galaxy, and then the different symbols of the same color correspond to the various pairs of secondary components in that galaxy.

Using the equations in Sect. 2.3.3, we have estimated the mass, mass loss rate, and kinetic energy associated with all the weak components in the Hα

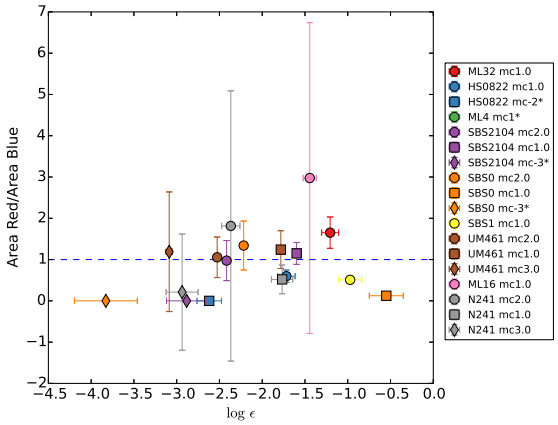

Figure 2.9: Area ratio between the blue and red emission of paired components versus mean strength of the secondary components relative to the central component, i.e., area ratio versus ε. Each point corresponds to one pair in one of the galaxies, as indicated in the inset – each galaxy has a color, and the different symbols with same color correspond to different weak components of the same galaxy. When only one component exists, it tends to be the blue one (they are marked with an asterisk in the inset). We show unpaired components as having an area ratio equal to zero. Except for ML32, the ratio is consistent with one or smaller. There is no obvious trend in the observed scatter plot.

wings (Sect. 2.3.2; Fig. 2.3). The mean values, as well as the errors, are given in Table 2.4.

The velocities and the ratio between the secondary components and the central component, ε, are provided directly by the multi-Gaussian fit described in Sect. 2.3.2. In the case of paired components, the velocity is the mean of the absolute value of the two velocities, and ε is the total ε of the pair. The estimates also depend on the temperature and electron density of the emitting plasma, as well as on the relative thickness of the shell, $\Delta R/R$, and the filling factor, f.

The electron temperature is taken from the data used to determine oxygen abundance in SA+15. Specifically, we use the mean over the main star-forming region of the galaxy. The electron density has been inferred from the ratio of the emission lines [SII]λ6716 and [SII]λ6731, following the standard procedure (e.g., Osterbrock 1974), using the mean value over the whole star-forming region. These two lines are present within the spectral range observed with the WHT. Electron densities and temperatures are listed in Table 2.2. As for the thickness of the shell, we use $\Delta R/R = 0.3$ (see Sect. 3.3). The filling factor, f, is assumed

Table 2.4: Parameters for the weak components in the Hα wings [a].

ID [b]	Velocity [c] [km s^{-1}]	ε [d]	red/blue [e]	M_g [10^3 M$_\odot$]	R [pc]	$\dot{M}_g$ [M$_\odot$ yr^{-1}]	E_k [10^{51} erg]	Age [10^4 yr]
ML4-1. *	98 ± 8	0.031 ± 0.012	—	37 ± 15	30 ± 4	0.41 ± 0.17	3.5 ± 1.5	30 ± 5
HS0822-1.0	114 ± 6	0.019 ± 0.005	0.6 ± 0.15	0.47 ± 0.13	4.9 ± 0.5	0.037 ± 0.011	0.061 ± 0.018	4.2 ± 0.5
HS0822-2 *	−248 ± 9	0.0024 ± 0.0008	—	0.06 ± 0.02	2.5 ± 0.3	0.02 ± 0.008	0.036 ± 0.013	0.97 ± 0.12
SBS0-1.0	16 ± 8	0.28 ± 0.13	0.12 ± 0.03	8 ± 4	8.5 ± 1.3	0.05 ± 0.04	0.02123 ± 0.02	50 ± 30
SBS0-2.0	211 ± 0.4	0.0061 ± 0.0005	1.3 ± 0.6	0.18 ± 0.03	2.35 ± 0.13	0.054 ± 0.009	0.079 ± 0.013	1.09 ± 0.06
SBS0-3 *	−370 ± 20	0.00015 ± 0.00013	—	0.004 ± 0.004	0.68 ± 0.2	0.008 ± 0.007	0.006 ± 0.005	0.18 ± 0.05
SBS1-1.0	98 ± 3	0.11 ± 0.03	0.51 ± 0.03	1.3 ± 0.4	5.3 ± 0.6	0.08 ± 0.03	0.12 ± 0.04	5.3 ± 0.6
ML16-1.0	110 ± 40	0.036 ± 0.006	3 ± 4	2.6 ± 0.6	8 ± 0.6	0.12 ± 0.05	0.3 ± 0.2	7 ± 2
UM461-1.0	116 ± 3	0.0165 ± 0.002	1.2 ± 0.5	0.08 ± 0.015	1.53 ± 0.09	0.021 ± 0.004	0.011 ± 0.002	1.29 ± 0.09
UM461-2.0	248 ± 3	0.00297 ± 7e-05	1.1 ± 0.5	0.014 ± 0.002	0.86 ± 0.04	0.014 ± 0.002	0.0088 ± 0.0013	0.34 ± 0.017
UM461-3.0	372 ± 4	0.00082 ± 7e-05	1.2 ± 1.4	0.0039 ± 0.0007	0.56 ± 0.03	0.0089 ± 0.0016	0.0054 ± 0.0009	0.148 ± 0.008
N241-1.0	115 ± 4	0.017 ± 0.005	0.5 ± 0.3	10 ± 3	10.7 ± 1.2	0.35 ± 0.12	1.3 ± 0.4	9.2 ± 1
N241-2.0	236 ± 9	0.0043 ± 0.0011	2 ± 3	2.4 ± 0.7	6.8 ± 0.6	0.28 ± 0.09	1.3 ± 0.4	2.8 ± 0.3
N241-3.0	395 ± 7	0.0012 ± 0.0005	0.2 ± 1.4	0.6 ± 0.3	4.4 ± 0.7	0.2 ± 0.1	1 ± 0.5	1.08 ± 0.17
SBS2104-1.0	112 ± 2	0.025 ± 0.002	1.1 ± 0.3	0.46 ± 0.09	3.4 ± 0.2	0.052 ± 0.01	0.057 ± 0.011	2.96 ± 0.19
SBS2104-2.0	246 ± 4	0.0038 ± 0.0002	1 ± 0.5	0.07 ± 0.013	1.8 ± 0.11	0.032 ± 0.006	0.042 ± 0.008	0.72 ± 0.04
SBS2104-3 *	−372 ± 10	0.0013 ± 0.0007	—	0.024 ± 0.014	1.3 ± 0.2	0.024 ± 0.014	0.033 ± 0.019	0.33 ± 0.06
ML32-1.0	93 ± 9	0.062 ± 0.014	1.7 ± 0.4	490 ± 130	71 ± 6	2.2 ± 0.7	42 ± 14	74 ± 10

[a] The error bars in this table represent the standard deviation across the starburst (velocity, ε, and area ratio), or errors for the value obtained from the mean Hα line of the starburst (the rest).
[b] The number added to the galaxy name identifies each one of the pairs of components in the line profiles, with '1.0' representing the pair of lowest velocity, '2.0' the second lowest velocity, and so on.
[c] Velocity of the center of the component. Negative, when there is no red counterpart to the blue component. In paired components, mean of the absolute value of the pair.
[d] Area ratio between the secondary component and the main component. In paired components, total ε of the pair.
[e] Area ratio between the red and blue emissions in the case of paired components.
∗ Unpaired component.

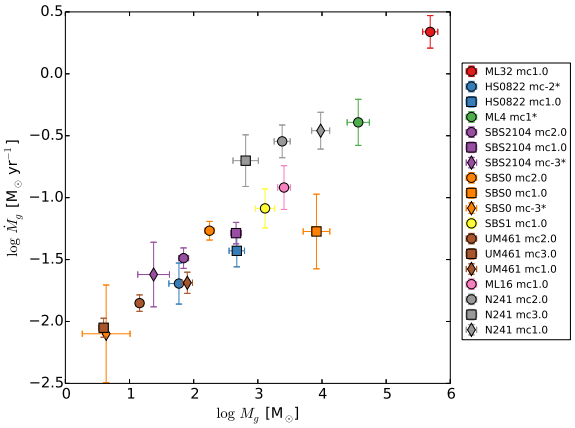

Figure 2.10: Mass loss rate versus gas mass for the faint components observed in the wings of Hα. The color code and symbols have the same meaning as in the previous figure, which is indicated in the inset.

to be one.

The velocities of the weak secondary components are typically in excess of 100 km s^{-1} (see Table 2.4). These velocities are very large compared with the rotational and turbulent velocities of the galaxies (Sect. 2.4), and, hence, are almost certainly larger than the escape velocity of the galaxy, expected to be of the order of the rotational plus turbulent velocity in the disk (e.g., Binney & Tremaine 2008). Assuming that the components in the wings correspond to outflows in expanding shells, it is still unclear whether or not the involved mass will finally escape from the galaxy. It all depends on the ISM of the host galaxy, and the pressure it exerts on the expanding shell. The issue is analyzed in Sect. 2.5.2, with the conclusion that the gas will likely escape. The mass involved in these motions is given in Table 2.4 and summarized in Fig. 2.10. The masses are in the range between 10 M$_\odot$ and 10^5 M$_\odot$, and they represent a few percent of the total gas mass in the HII region (the parameter ε in Table 2.4 gives the flux ratio between the secondary and the main emission lobe, and it has been taken as a proxy for the mass ratio; see Eqs. [2.21] and [2.22]). These masses are very small compared to the stellar masses and the dynamical masses of the entire galaxies (Tables 2.1 and 2.3).

Figure 2.10 shows that the mass loss rate scales with the gas mass, since the velocities and radii of the different components and galaxies are similar. The weak components have associated mass loss rates between 10^{-2} and 1 M$_\odot$ yr^{-1}. They are very significant compared with the SFRs, as is attested in Fig. 2.11,

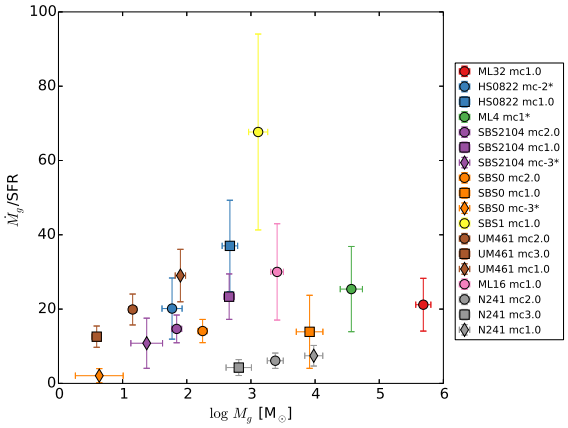

Figure 2.11: Mass loading factor ($\dot{M}_g$/SFR) versus gas mass, for the weak components observed in the wings of Hα. All factors are larger than one, meaning that for every unit mass transformed in stars, several units are swept away by the expansion. The color code and symbols have the same meaning as in previous figures, which is indicated in the inset.

which shows the mass loading factor, $\dot{M}_g$/SFR. Most mass loading factors are in excess of one, meaning that for every mass unit transformed into stars, several mass units are swept away. Whether this mass escapes the HII region, and later on, the galaxy, we cannot know from our observations. However, cosmological numerical simulations predict large mass loading factors in low mass galaxies (10 is not uncommon; see, e.g. Peeples & Shankar 2011; Davé et al. 2012; Oppenheimer et al. 2012; Bournaud et al. 2014; Thompson & Krumholz 2016). Mass loading factors observed in high redshift objects are generally lower than the ones we infer (say, of the order of 2, e.g., Newman et al. 2012; Martin et al. 2012), likely because they refer to massive galaxies ($\log(M_\star/M_\odot) > 10$). However, it is not uncommon to find factors up to 10 in local dwarfs (e.g., Martin 1999; Veilleux et al. 2005). A caveat is in order, though. We are assuming the density of the shell to be the same as the mean density of the star-forming region. If the expanding shell builds up mass by sweeping gas around the explosion site, its density is expected to be higher than the mean density of the region. This increase of density would reduce our mass loading factor estimates (see Eq. [2.22]).

Figure 2.12 shows the kinetic energy associated with the weak components. As with the mass loss rate, it scales with the mass of gas that is involved in the motion. Figure 2.12 also shows the energy typically associated with a core-

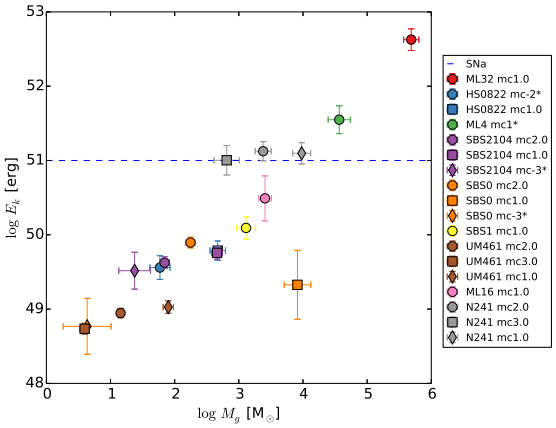

Figure 2.12: Kinetic energy versus gas mass, for the weak components observed in the wings of Hα. The line at 10^{51} erg corresponds to the typical kinetic energy released by a core-collapse SN, characteristic of massive stars. The color code and symbols have the same meaning as in previous figures, which is indicated in the inset.

collapse SN explosion, of the order of 10^{51} ergs (e.g., Leitherer et al. 1999). The energies involved in the observed motions are usually around this value, albeit smaller; ML32 is a bold exception. Therefore, energy-wise, the components may be tracing shells produced by individual SN explosions. ML32 would require some 10 SN exploding simultaneously.

Depending on the IMF (initial mass function), population synthesis models predict a SN rate between 0.02 and 0.005 yr^{-1} for a constant SFR=1 M$_\odot$ yr^{-1} (Leitherer et al. 1999). Using a value in between these two extremes, say 0.01 yr^{-1}/(M$_\odot$yr^{-1}), the SFRs of our star-forming regions (Table 2.2) allow us to estimate the expected SN rates assuming the observed SFRs to be constant. The predicted SN rate turns out to be between 10^{-3} and 10^{-5} yr^{-1}, which corresponds to a time-lag between SN explosions (τ_{SN}, defined as the inverse of the SN rate) from 1000 yr to 0.1 Myr. These rates suffice to maintain the observed signals. Figure 2.13 provides Age/τ_{SN} for individual shells. $Age > \tau_{SN}$ in half of the cases, which implies expecting more than one SN signal at a time, as we observe.

Ages are estimated from the measured velocity and the estimated radius of the shell (Eq. [2.19]). These radii are small compared to the size of the star-forming regions. Figure 2.13 shows the radius relative to the effective radius of the region, with the typical ratio being around 10 % or smaller. Therefore, it is important to keep in mind, for interpreting the weak emission components

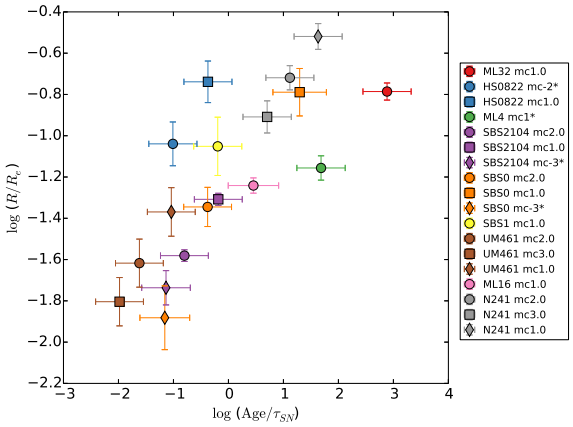

Figure 2.13: Radius of the shell in terms of the radius of the star-forming region (R/R_e) versus *Age* of the shell relative to the expected time-lag between SN explosions (τ_{SN}). The color code and symbols have the same meaning as in previous figures, which is indicated in the inset.

in the wings of Hα, that there are one or several (probably non-concentric) expanding shells embedded in a large star-forming region. This substructure is common in giant HII regions, such as 30 Doradus in the large Magellanic cloud (e.g., Meaburn 1984; Sabbi et al. 2013; Camps-Fariña et al. 2015). Shells and holes appear in Hubble Space Telescope (HST) images of the large starburst in Kiso 5639, a tadpole galaxy very similar to the XMPs studied here (Elmegreen et al. 2016b).

We do not see a dependence of the properties of the weak emission-line components on the mean metallicity of the starburst, except perhaps for the mass loading factor. Figure 2.14 shows the scatter plot of metallicity versus mass loading factor, and it hints at an increase of the factor with increasing metallicity. The trend may be coincidental, due to the small number of points in the plot. However, it may also indicate the contribution of stellar winds to the energy and momentum driving the observed expansion. The winds of massive stars can provide a total kynetic energy comparable to the energy released during their SN explosions (e.g., Fierlinger et al. 2016), and these radiation-pressure driven winds have mass loss rates that increase with increasing metallicity (e.g., Martins 2015). The metallicities represented in Fig. 2.14 correspond to the metallicity averaged over the starburst and, thus, due to the variation of metallicity across the star-forming region, their value is slightly higher than the values quoted in SA+15. ML16, the point of highest metallicity in Fig. 2.14, is

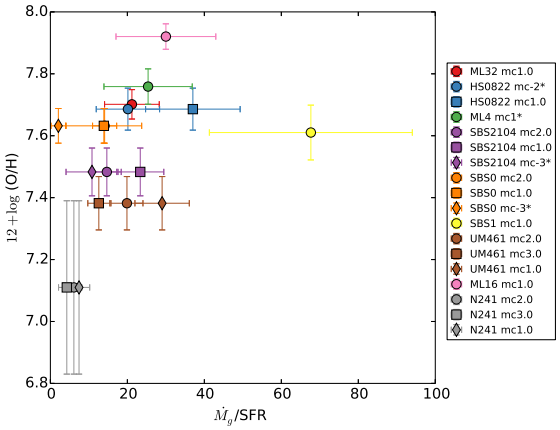

Figure 2.14: Mean metallicity of the star-forming region versus mass loading factor. The color code and symbols have the same meaning as in previous figures, as indicated in the inset.

also the galaxy with no detected metallicity inhomogeneity in SA+15.

2.5.2 Other interpretations

One can think of several alternatives to explain the existence of multiple paired emission-line components in the wings of Hα. The previous section analyzes the possibility of being produced by spatially-unresolved expanding shells driven by SN explosions. Here we discuss other options, such as (1) spatially-unresolved rotating structures, (2) spatially-resolved expanding shells, (3) bipolar outflows, (4) blown out spherical expansion leading to expanding rings, and (5) spatially-unresolved expanding shells driven by BH accretion feedback.

(1) *Spatially-unresolved rotating disk-like structures.* Rotation naturally produces double-horned profiles (e.g., Epstein 1964). Therefore, one of the possibilities to explain the existence of blue and red paired emission peaks is the presence of a gaseous structure rotating around a massive object. The mass of the required central object can be estimated from the size of the rotation structure and the velocity (Sect. 2.3.4). Figure 2.15 shows that the mass of the central object needs to be around three orders of magnitude larger than the gas mass involved in the motions, with central masses, $M_\bullet$, ranging from 10^6–10^8 M$_\odot$. This mass turns out to be of the order of the stellar mass of the whole galaxy (Table 2.1), which rules out the stellar nature of the required central concentration. If, on the other hand, it were a BH, then it would have to have $M_\bullet \sim M_\star$, which is completely out of the so-called Magorrian-relationship

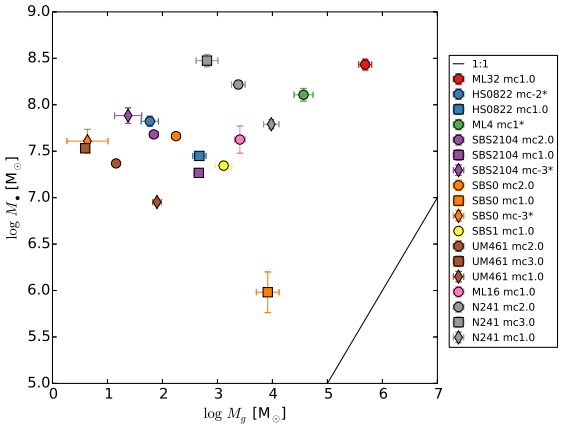

Figure 2.15: Mass of the central object versus gas mass if the pairs of faint emission components are interpreted as caused by a gaseous disk orbiting around a central massive object. The solid line represents the one-to-one relationship. The masses of the required central objects turn out to be unrealistically large, which disfavors this interpretation. The color code and symbols have the same meaning as in previous figures, which is indicated in the inset.

between the central BH mass and the stellar mass of the galaxy, for which $M_\bullet/M_\star \sim 10^{-3}$ (e.g., Kormendy & Ho 2013). Thus, the exotic nature of the required central mass disfavors the interpretation of the weak emission in the wings of Hα as caused by a disk orbiting around a massive central object, such as a BH.

(2) *Spatially-resolved expanding shells.* The inner part of a spatially resolved expanding shell also produces double peak emission-line profiles, since the outer parts of the shell, contributing to the line core, are excluded (e.g., Zuckerman 1987). We often see several pairs of emission peaks (Fig. 2.3a), therefore, this interpretation requires the existence of several resolved concentric shells, which is unrealistic since the first shell would have already swept the ISM around the center of the expansion. Moreover, the size of the shell is estimated to be smaller than the typical spatial resolution, so that the expanding regions cannot be spatially resolved.

(3) *Bipolar outflows.* Insofar as they comply with the energetics required to explain the observed motions, bipolar flows cannot be easily discarded. They create two-horned profiles, and several of them coexisting in the resolution element could explain the presence of multiple paired components. In fact, bipolar flows are extreme cases of non-spherically-symmetric shells, where double-horned line profiles appear naturally (e.g., Gill & O'Brien 1999).

(4) *Blown out spherical expansion leading to expanding rings.* If the radius of the shell exceeds the scale height of the disk of the galaxy, it may break up, leading to a ring-like expanding structure that produces two-horned profiles when observed edge-on. This possibility can be discarded since the ring would have to be as large as the disk thickness, which is incompatible with the small size of the expanding structures (Table 2.4).

(5) *Spatially-unresolved expanding shells driven by BH accretion feedback.* Energywise, intermediate mass BHs of 10^5 $M_\odot$ can also power the expanding shells that we characterize in Sect. 2.5.1 (see Eq. [2.24]). However, the observations also disfavor this option for a number of reasons. It is unclear how a primordial BH seed can coincide spatially with a star-forming region unless there are many such BHs lurking in the galaxy, or the BH is born in situ. 10^5 $M_\odot$ BHs can be produced by direct collapse in the early universe, but this explanation can be discarded, since they are very rare (e.g., van Wassenhove et al. 2010) and many of them are needed. On the other hand, 100 $M_\odot$ BHs are expected to be more common, left as remnants from population III stars formed in the early universe or even today (e.g., Kehrig et al. 2015). However, this alternative is also very unlikely, since HII regions are short-lived (a few tens of Myr; e.g., Leitherer et al. 1999), and a BH requires several hundred Myr of continuous feeding to grow from 100 to 10^5 $M_\odot$ (see, e.g., Volonteri 2010). Finally, accreting BHs are expected to be luminous X-ray sources. Five of our XMPs were observed with the X-ray satellite Chandra: HS0822, SBS1, N241, SBS2109, and UM 461 (Kaaret et al. 2011; Prestwich et al. 2013). Only one of them shows a signal above the noise, namely, SBS1, with an X-ray luminosity around 10^{39} erg s^{-1}. This level of emission is consistent with young SNe (e.g., Filho et al. 2004; González-Martín et al. 2006; Dwarkadas & Gruszko 2012).

2.6 The fate of the swept out material

Independently of the details on whether the shells are symmetric, or if they have internal extinction, the expanding shell model appears to be the best explanation to reproduce the weak emission features observed in the Hα wings. One of the consequences of this interpretation is that the mass loading factor that we infer may be reflecting the feedback of the star formation process on the medium in, and around, the galaxy. The measured mass loading factor is very large, of the order of ten or larger (Fig. 2.11), which implies that for every solar mass of gas transformed into stars, at least ten times more gas is swept away from the region. How far this swept gas goes is impossible to tell from the data alone. However, a significant fraction may escape from the galaxy to the CGM and even the intergalactic medium (IGM). The speeds, larger than 100 km s^{-1}

and up to 400 $\mathrm{km\,s^{-1}}$ (Table 2.4), likely exceed the escape velocity of the galaxy. The final fate of the gas depends on whether the gas pressure in the ISM of the galaxy suffices to slow down and confine the expansion. Even though we do not know the gas pressure of the ISM, it must be similar to the turbulent pressure in the star-forming region, so that the region is neither expanding nor shrinking considerably (the moderate global expansion observed in some cases is analyzed in the paragraph at the end of the section). The turbulent pressure scales with the square of the turbulent speed, and so does the pressure exerted by the shell on the ISM (e.g., Chandrasekhar 1951; Bonazzola et al. 1987). The measured turbulent velocities are of the order of 25 $\mathrm{km\,s^{-1}}$ (see Table 2.2, and keep in mind that the quoted values are FWHM velocities rather than velocity dispersions), hence, provided that the HII region and the shell have similar densities, the ISM will not be able to confine an expanding shell with a speed of a few hundred $\mathrm{km\,s^{-1}}$. A significant part of the matter in the shell may eventually escape from the galaxy. Martin (1999) made a qualitative estimate of the conditions for starburst-driven outflows to escape, finding that the gas flows out from galaxies with rotation smaller than 130 $\mathrm{km\,s^{-1}}$, i.e., from our XMPs.

Under the hypothesis of expanding shell, it is possible to compute the column density to be expected if the shell material reaches the CGM. Assuming mass conservation, and if the shell geometry is maintained, the typical column density when the shell expands to a radius R' is,

$$N_H \simeq 7.9 \times 10^{14}\,\mathrm{cm^{-2}}\,\frac{R}{10\,\mathrm{pc}}\,\frac{n_e}{10^2\,\mathrm{cm^{-3}}}\left[\frac{R/R'}{10^{-3}}\right]^2, \tag{2.27}$$

where the electron density, n_e, and the radius, R, are those measured in the star-forming regions. Note that for the typical sizes and densities of our shells, and with expansion factors of the order of 10^3 that transform pc-size shells into intergalactic size structures (from $R \simeq 10\,\mathrm{pc}$ to $R' \simeq 10\,\mathrm{kpc}$), the column densities predicted by Eq. (2.27) are of the order of $10^{15}\,\mathrm{cm^{-2}}$. This gas would be undetectable with current instrumentation, even if it were fully neutral. For example, a high-sensitivity survey such as HIPASS sets the limit at $4 \times 10^{17}\,\mathrm{cm^{-2}}$ (Meyer et al. 2004), and values of $10^{17}\,\mathrm{cm^{-2}}$ will be achieved by SKA after a 1000 hour integration (de Blok et al. 2015). Moreover, at these low column densities the intergalactic ultraviolet (UV) background will keep the gas fully ionized, which makes it even more elusive. How long would it take for the gas to reach the CGM? Assuming that the original velocities are maintained, the time to reach the CGM is the expansion factor, R'/R, times the *Age* in Eq. (2.19). Given the *Age* in Table 2.4 and $R'/R \simeq 10^3$, the time-scale is of the order of 10 Myr, which is short compared to the time-scale for

galaxy evolution. In summary, the shells that we observe in the star-forming regions are expected to reach the CGM, and may do so in a reasonable timescale. Unfortunately, they would be undetectable with current instrumentation unless the expansion is more moderate than expected according to Eq. (2.27).

We show in Sect. 2.4 that some of the star-forming regions may be undergoing a global expansion, with a moderate velocity of around 15 $\mathrm{km\,s^{-1}}$. The mass loss rate associated with this global expansion, $\dot{M}_G$, can also be estimated using Eq. (2.15), except that this time the global mass of the starburst, M_G, and the radius of the starburst, R_e, have to be considered. A simple substitution renders $\dot{M}_G$ in terms of the mass loss rate inferred for one of the weak components in the wings of Hα, i.e.,

$$\dot{M}_G/\dot{M}_g \simeq \varepsilon^{-1}\,(R/R_e)\,(15\ \mathrm{km\,s^{-1}}/v_{\mathrm{out}}), \tag{2.28}$$

where we have assumed $\Delta R/(R_e/3) \simeq R/R_e$, and $M_g/M_G \sim \varepsilon$. Using typical values for these parameters, $\varepsilon \simeq 5 \times 10^{-3}$ (Table 2.4), $v_{\mathrm{out}} \simeq 150\ \mathrm{km\,s^{-1}}$ (Table 2.4), and $R/R_e \sim 5 \times 10^{-2}$ (Figure 2.13), one finds that the two mass loss rates are similar, i.e.,

$$\dot{M}_G/\dot{M}_g \sim 1. \tag{2.29}$$

One can repeat the exercise for the kinetic energy involved in the global expansion (Eq. [2.23]), which scales with the mass ratio and the square of the expansion velocities. Using the typical values given above, the two kinetic energies turn out to be similar too. This rough estimate leads to the conclusion that the mass loss rate and the kinetic energy involved in the global expansion of the star-forming region are similar to the values inferred for the emission features observed in the wings of Hα. The question arises as to whether the global expansion unbounds the gas in the starburst, and so may contribute to the global mass loss of the XMPs. As was the case with the small expanding shells discussed above, the answer to the question is very uncertain, and cannot be addressed resorting to our observational data alone. The fate of the gas depends on the unknown value of the ISM pressure. In contrast with the small shells, the expansion velocities are significantly smaller than the expected escape velocity. Moreover, the turbulent velocity of the galaxies is typically 40–50 $\mathrm{km\,s^{-1}}$, and, hence, comparable, but larger, than the turbulent velocity in the star-forming region (see Fig. 2.6). Only if the density in the ISM of the XMPs is much lower than the density in the starburst, the starburst may be overpressureized and the mild observed expansion can drive gas through the ISM to large distances.

2.7 Conclusions

The XMP galaxies analyzed in SA+15 are characterized by having a large star-forming region with a metal content lower than the rest of the galaxy. The presence of such chemical inhomogeneities suggests cosmological gas accretion as predicted in numerical simulations of galaxy formation. Cosmological gas accretion induces off-center giant star-forming clumps that gradually migrate toward the center of the galaxy disks (Ceverino et al. 2010; Mandelker et al. 2014). The star-forming clumps may be born in-situ or ex-situ. In the first case, the accreted gas builds up the gas reservoir in the disk to a point where disk instabilities set in and trigger star formation. In the second case, already formed clumps are incorporated into the disk. They may come with stars and dark matter, and thus, they are often indistinguishable from gas-rich minor mergers (Mandelker et al. 2014). Since they feed from metal-poor gas, the star-forming clumps are more metal-poor than their immediate surroundings (Ceverino et al. 2016). In order to complement the chemical analysis carried out by SA+15, I study the kinematic properties of the ionized gas forming stars in the XMP galaxies. Nine objects were studied (Table 2.1) with a spectral resolution of the order of 7500, equivalent to 40 $\mathrm{km\,s^{-1}}$ in Hα.

Most XMPs have a measurable rotation velocity, with a rotation amplitude which is only a few tens of $\mathrm{km\,s^{-1}}$ (Fig. 2.5). All rotation curves present small-scale velocity irregularities, often with an amplitude comparable to the velocity gradient across the whole galaxy. On top of the large-scale motion, the galaxies also present turbulent motions of typically 50 $\mathrm{km\,s^{-1}}$ FWHM (see Fig. 2.6 and Table 2.2), and, therefore, larger than the rotational velocities.

Observations suggest that the main star-forming region of the galaxy moves coherently within the host galaxy (Fig. 2.1). The velocity is constant (Fig. 2.7), so that the region moves as a single unit within the global rotation pattern of the galaxy. In addition, the velocity dispersion in some of these large star-forming clumps increases toward the center-side of the galaxy. The excess velocity dispersion on the center-side may indicate an intensification of the turbulence of the gas that collides with the ISM of the host galaxy, as if the clumps were inspiraling toward the galaxy center. This migration to the galaxy center is expected from tidal forces acting upon massive gas clumps (see, e.g., Elmegreen et al. 2008, 2012a; Bournaud et al. 2008; Ceverino et al. 2016), and the large starbursts in our XMPs may be going through the process at this moment. In some other cases, the velocity dispersion has a local maximum at the core of the star-forming region, which suggests a global expansion of the whole region, with a moderate speed of around 15 $\mathrm{km\,s^{-1}}$. Sometimes the velocity dispersion presents a minimum at the core, which may reflect a past

global expansion that washed out part of the turbulent motions.

We find no obvious relationship between the kinematic properties and the metallicity drops, except for the already known correlation between the presence of a starburst and the decrease in metallicity. We do find, however, a significant lack of correlation between the metallicity and the ratio N/O (Fig. 2.8), which is consistent with the gas accretion scenario. If the accretion of metal-poor gas is fueling the observed starbursts, then the fresh gas reduces the metallicity (i.e., O/H), but it cannot modify the pre-existing ratio between metals (e.g., Amorín et al. 2010, 2012), forcing the ratio N/O to be similar inside and outside the starburst.

The Hα line profile often shows a number of faint emission features, Doppler-shifted with respect to the central component. Their amplitudes are typically a few percent of the main component (Fig. 2.3), with the velocity shifts being between 100 and 400 km s^{-1} (Table 2.4). The components are often paired, so that red and blue peaks, with similar amplitudes and shifts, appear simultaneously. The red components tend to be slightly fainter, however. Assuming that the emission is produced by recombination of H, we have estimated the gas mass in motion, which turns out to be in the range between 10 and 10^5 M$_\odot$ (Table 2.4 and Fig. 2.10). Assuming that the Doppler shifts are produced by an expanding shell-like structure, we infer a mass loss rate between 10^{-2} and a few M$_\odot$ yr^{-1}. Given the observed SFR, the mass loss rate yields a mass loading factor (defined as the mass loss rate divided by the SFR) typically in excess of 10. Large mass loading factors are indeed expected from numerical simulations (e.g., Peeples & Shankar 2011; Davé et al. 2012; Oppenheimer et al. 2012), and they reflect the large feedback of the star formation process on the surrounding medium. Numerical simulations predict that low mass galaxies are extremely inefficient in using their gas, most of which returns to the IGM without being processed through the stellar mechanism. Since the measured expansion velocities exceed by far the rotational and turbulent velocities, we argue in Sect. 2.5.2 that the gas involved in the expansion is bound to escape from the galaxy disk, reaching the CGM and possibly the IGM. Therefore, the large mass loading factors that we measure support and constrain the predictions from numerical simulations. We have estimated the H column density to be expected when the shell material reaches the CGM, and it turns out to be around 10^{15} cm^{-2}. Even if all the H were neutral, this is undetectably small with present technology. Moreover, at these low column densities, all H is expected to be ionized by the cosmic UV background. Even if the IGM of the XMPs were filled by expanding shells from previous starbursts, they would be extremely elusive observationally.

From an energetic point of view, the observed motions involve energies

between 10^{49} and 10^{52} erg, which are in the range of the kinetic energy released by a core-collapse SN ($\sim 10^{51}$ erg). The low-end energy requires that only part of the SN kinetic energy drives the observed expansion, whereas the high-end energy requires several SNe going off quasi-simultaneously. The observed SFRs allow for the required number of SNe, and the estimated age of the shells (10^4–10^6 yr; Table 2.4) is also consistent with the expected SN rate. Other alternatives to explain the weak emission peaks in the wings of Hα, like BH driving the motions or the expansion, can be discarded using physical arguments (Sect. 2.5.2).

Some of the data suggest a moderate global expansion of the star-forming regions (Sect. 2.6). Even if the expansion velocity is small (around 15 $\mathrm{km\,s^{-1}}$), the motion involves the mass of the whole region, and, hence, the associated mass loss rate and kinetic energy turn out to be similar to those carried away by the fast-moving secondary components. Thus, global expansion may also be important in setting up the mass and energy budgets associated with star formation feedback.

High redshift clumpy galaxies are probably growing through cosmological gas accretion processes similar to those experienced by XMPs. However, the physical conditions at high and low redshifts differ (e.g., the gas accretion rates are larger at high redshifts), so do the observational biases affecting XMPs and high-redshift clumpies (e.g., low-mass galaxies are undetectable at high redshift). Therefore, addressing the issue of whether XMPs are low-mass analogues of high-redshift clumpies is complicated, and is beyond the scope of our work. However, because of their probable common physics, it is interesting to point out some of the similarities and differences of the two samples. As in the case of XMPs, some clumpy galaxies show metallicity drops associated with enhanced star-formation activity (Cresci et al. 2010; Troncoso et al. 2014). High redshift galaxies are significantly more massive than XMPs. Using as reference for high redshift galaxies (1.3–2.6) the SINS[8] sample (Förster Schreiber et al. 2009), the stellar mass of the high-redshift objects ($10^{9.5}$–$10^{11}\,M_\odot$) is three orders of magnitude larger than the mass of XMPs (10^6–$10^{8.5}\,M_\odot$; Table 2.1). This difference in stellar mass shows in dynamical mass too, with rotational velocities between 100 and 260 $\mathrm{km\,s^{-1}}$ at high redshift. We cannot directly compare the rotational velocities of XMPs with these values since we cannot correct for inclination, however, the uncorrected values go from zero to 30 $\mathrm{km\,s^{-1}}$ (see Fig. 2.5). The velocity dispersion in XMPs ranges from 10 and 20 $\mathrm{km\,s^{-1}}$ (corresponding to FWHM between 25 and 50 $\mathrm{km\,s^{-1}}$; see Fig. 2.6), whereas it is between 50 and 200 $\mathrm{km\,s^{-1}}$ at high-redshift (Förster Schreiber

[8]SINFONI Integral Field Spectroscopy of redshift two Star-forming Galaxies.

et al. 2009). The high redshift objects have a ratio between rotational velocity and velocity dispersion between 0.5 and one (Förster Schreiber et al. 2009). XMPs seem to have similar ratios, even though we cannot be more precise since the measured rotation in XMPs is affected by inclination. The total SFRs are very different (10 – $500\,M_\odot\,\mathrm{yr}^{-1}$ at high redshift and 0.001 – $0.1\,M_\odot\,\mathrm{yr}^{-1}$ in XMPs), but the surface star-formation rates are not; they go from 0.01 to $10\,M_\odot\,\mathrm{yr}^{-1}\,\mathrm{kpc}^{-2}$ at high redshift (e.g., Fisher et al. 2016) and from 0.005 to $0.8\,M_\odot\,\mathrm{yr}^{-1}\,\mathrm{kpc}^{-2}$ in XMPs (SA+15). Mass loading factors are one order of magnitude larger in XMPs than those inferred for high-redshift clumpy galaxies (Sect. 2.5; see also Newman et al. 2012), a difference that we attribute to their very different masses. However, the differences of size between the expanding regions of clumpies and XMPs may also play a role (see Eq. [2.15]). Local UV bright clumply galaxies (Elmegreen et al. 2012b) are often XMPs with metallicity drops (Sánchez Almeida et al. 2013), and we know that their star-forming clumps resemble those in high-redshift cumplies in terms of total SFR, clump mass, and stellar mass surface density (Elmegreen et al. 2013).

2.8 Appendix: Emission of an expanding dusty shell of gas

The emission of a uniform shell produces a top-hat line profile that is not consistent with the two-horned profiles observed in the wings of Hα (Fig. 2.3). However, if the shell has some internal extinction, then it preferentially absorbs photons emerging from the regions where the line-of-sight (LOS) tends to be parallel to the surface of the shell. Those are the regions of small Doppler shifts that contribute to the line center, thus creating a two-horned profile.

The effect can be readily shown assuming an expanding shell of radius R and width ΔR, as shown in Fig. 2.16a. The velocity along the LOS, v_z, only depends on the inclination angle, θ,

$$v_z = v\,\cos\theta. \tag{2.30}$$

Therefore, the line profile, $I(v_z)$, is just the total energy emitted with velocity between v_z and $v_z + \Delta v_z$, divided by Δv_z. Because of Eq. (2.30), it is proportional to the energy emitted by the ring of the shell with inclination angles between θ and $\theta + \Delta\theta$, i.e.,

$$\Delta s = \int_0^{2\pi} \int_{R-\Delta R/2}^{R+\Delta R/2} \int_{\theta}^{\theta+\Delta\theta} \epsilon\,\sin\theta'\,R'^2\,d\phi\,dR'\,d\theta', \tag{2.31}$$

where R is the radius of the shell of width ΔR, ϕ is the azimuth in spherical coordinates, and ϵ stands for the emission per unit volume. Assuming the shell to be small enough ($\Delta R \ll R$), then

$$\Delta s \simeq 2\pi\,R^2\,\sin\theta\,\Delta\theta \int_{R-\Delta R/2}^{R+\Delta R/2} \epsilon\,dR'. \tag{2.32}$$

According to the definition of $I(v_z)$,

$$I(v_z) = \Big|\frac{\Delta s}{\Delta v_z}\Big| = \Big|\frac{\Delta s}{\Delta\theta}\,\frac{\Delta\theta}{\Delta v_z}\Big| \simeq \Big|\frac{\Delta s}{\Delta\theta}\left(\frac{dv_z}{d\theta}\right)^{-1}\Big|, \tag{2.33}$$

so Eqs. (2.30), (2.32) and (2.33) yield,

$$I(v_z) \simeq 2\pi\,R^2\,v^{-1} \int_{R-\Delta R/2}^{R+\Delta R/2} \epsilon\,dR', \tag{2.34}$$

which holds only for $|v_z| \leq v$. Outside this range of velocities, Δs is equal to zero, and so is $I(v_z)$.

In the case that ϵ is constant, then $I(v_z)$ is also constant (Eq. [2.34]), leading to the top-hat line profiles expected from an optically thin expanding shell. We

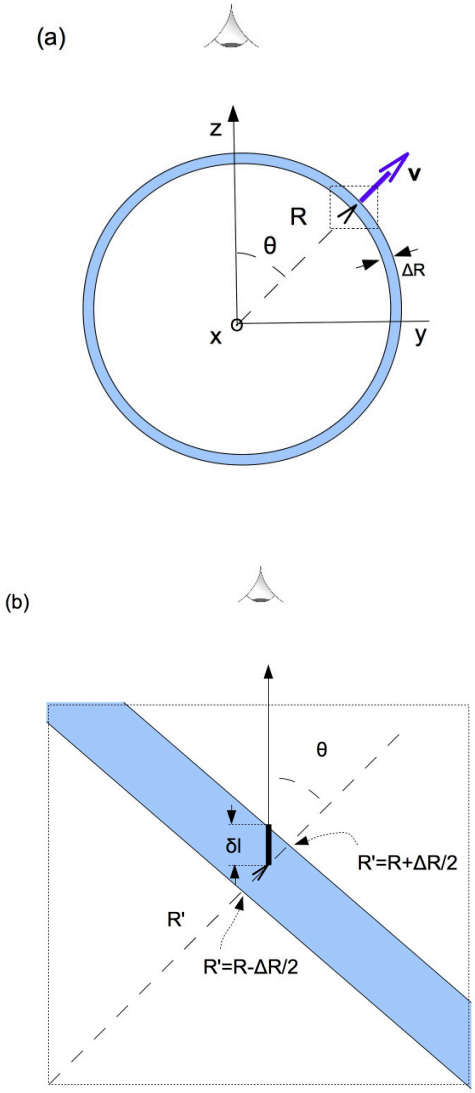

Figure 2.16: Schematic used to compute the emission-line profile of an expanding dusty shell of radius R and width ΔR. (a) Projection of the shell in the Y-Z plane, with Z in the direction along the LOS. The velocity vector, $\mathbf{v}$, in the direction set by θ is shown as a blue solid-line arrow. (b) Zoom-in of the region enclosed by the dotted-line rectangle in (a). The length along the LOS traversed by the photons emitted at coordinates (θ, R') is denoted as δl, with $\delta l = (R + \Delta R/2 - R')/\cos\theta$.

will consider the case where the emission is constant, ϵ_0, but the shell absorbs part of the emitted photons due to internal extinction, β, i.e.,

$$\epsilon = \epsilon_0 \, \exp(-\beta \delta l), \tag{2.35}$$

with

$$\delta l(R') \simeq \frac{R + \Delta R/2 - R'}{\cos\theta}, \tag{2.36}$$

as shown in Fig. 2.16b. For the moment, we have assumed that the emission occurs in the upper cap only. Using Eqs. (2.34), (2.35), and (2.36),

$$I(v_z) \simeq I_0 \, \frac{\cos\theta}{\beta \Delta R} \Big[1 - \exp(-\beta \Delta R / \cos\theta) \Big], \tag{2.37}$$

$$\cos\theta \geq 0, \qquad \text{or} \qquad v_z \geq 0,$$

with I_0 the emitted intensity if there were no extintion ($\beta \longrightarrow 0$),

$$I_0 = 2\pi \, R^2 \, \Delta R \, v^{-1} \, \epsilon_0. \tag{2.38}$$

The case of the lower cap is similar, except that one has to consider the additional absorption produced by the upper cap. In this other case,

$$I(v_z) \simeq I_0 \, \frac{|\cos\theta|}{\beta \Delta R} \Big[1 - \exp(-\beta \Delta R / |\cos\theta|) \Big] \, \exp(-\beta \Delta R / |\cos\theta|), \tag{2.39}$$

with

$$\cos\theta < 0 \qquad \text{or} \qquad v_z < 0.$$

The typical values of the extinction coefficient at Hβ in XMPs are between 0.1 and 0.9 (Sánchez Almeida et al. 2016). These values were inferred from the Balmer decrement in Sloan Digital Sky Survey (SDSS) spectra of XMPs. If we use them to represent the total extintion in the shell, then $0.15 < \beta \, \Delta R < 1.5$, where we have considered the differential extintion between Hα and Hβ using the extinction law in the Milky Way by Cardelli et al. (1989). The dashed lines in Fig. 2.17 show examples of the line profiles resulting from Eqs. (2.37) and (2.39). They represent extinctions that cover the range of values mentioned above. We show the original profiles (dashed lines) plus their convolution with a Gaussian that represents the finite resolution of the observation (solid lines). The width of the Gaussian has been chosen so that, if it represents our WHT observations (FWHM $\sim$ 40 km s^{-1}), then the expansion velocities of the shells are similar to the speeds of the multiple components analyzed in Sect. 2.5. One can see the two-horned shape, with a redshifted lobe that is smaller than the

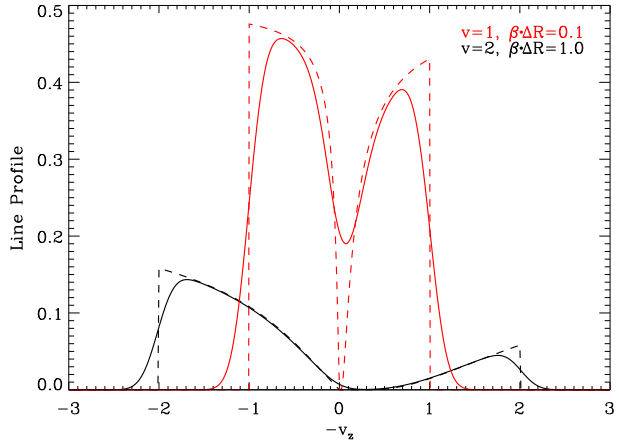

Figure 2.17: Line profiles expected from an expanding dusty shell. They portray both weak internal extinction ($\beta\Delta R = 0.1$; profiles in red), and significant internal extinction ($\beta\Delta R = 1.0$, profiles in black). Red and black lines also differ in the expansion speed v, as shown in the inset. We include the profiles predicted by Eqs. (2.37) and (2.39) (dashed lines), together with these profiles convolved with a Gaussian to represent the finite spectral resolution of the spectrograph (solid lines). We assume the FWHM of the Gaussian to be 0.35 in the dimensionless velocity scale. If this value is ascribed to the resolution of our observation (~ 40 km s^{-1}), then the expansion speeds for the shells giving rise to the red and black profiles are 110 km s^{-1} and 220 km s^{-1}, respectively. Abscissae show $-v_z$ rather than v_z so that the positive values correspond to redshifts.

blushifted lobe; the redshifted photons come from the lower cap of the shell, so that they are also extincted by the upper cap (we have flipped the sign of the abscissa axis in Fig. 2.17, so that positive corresponds to redshift, as usual).

The model in Eqs. (2.37) and (2.39) also predicts the fraction of emitted light lost by internal absorption. For the two profiles shown in Fig. 2.17, the fraction of light that emerges is 74 % and 24 % of the emitted light for the red and black profiles, respectively.

3

Gas in the circumgalactic medium of gas-accreting galaxies

3.1 Introduction

Given the importance of the cosmic web gas and the difficulties to constrain it observationally, we have tried a complementary approach to its detection and characterization. The properties of XMP galaxies (in particular the chemical inhomogeneities; see Sect. 1.1.2) suggest that they are going through one of the gas accretion episodes expected from numerical simulations. Therefore, they are ideal candidates to observe the gas involved in the process, inflows and outflows included. This is particularly relevant considering that XMPs are local galaxies which, in principle, could be studied in a detail unattainable at high redshift.

As we pointed out in section 1.1.1, there is evidence for Lyα emission around high-redshift galaxies tracing gas in the IGM and CGM (e.g., Cantalupo et al. 2014; Wisotzki et al. 2016; Arrigoni Battaia et al. 2019). The Lyα emission around XMPs is not accessible from ground observations but, fortunately, many physical processes able to generate Lyα photons produce Hα as well (to be discussed in Sect. 3.2). Thus, our strategy to detect this gas around XMPs includes deep imaging in Hα. Encouragingly, extended Hα emission around local star-forming galaxies has been recently detected (e.g., Herenz et al. 2017; Lin et al. 2017; and references in Sect. 3.2).

I carried out a systematic search for galaxies in the deep images of the IAC Stripe 82 Legacy Project that may be going through a gas accretion event at

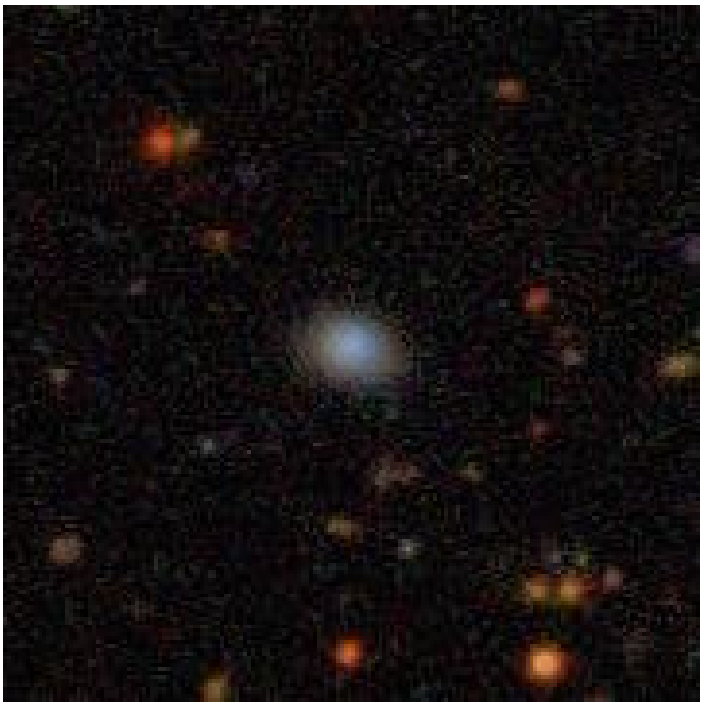

Figure 3.1: Color composition of the target galaxy UM260. It is based on the images of IAC Stripe 82 Legacy Project, using filter g as blue, filter r as green and filter i as red. The FOV is aproximately 71 × 71 arcsec^2. UM260 is at the center of the image. Note the whitish halo around the blue starbust, and the little cloud-like objects surrounding the galaxy.

present. The procedure and the list of targets is described in Appendix A. One of them was selected for a proof-of-concept observation (details to be given in Sect. 3.3.2).

This Chapter reports on the proof-of-concept observation to detect faint Hα emission around one such XMP using deep images taken with the 10-m GTC telescope (Gran Telescopio Canarias[1]). We targeted a field-of-view (FOV) around J0037+0033 (or UM 260, see Fig. 3.1). The observation turned out to be successful, detecting a low surface brightness emission halo at the level of 28 mag arcsec^{-2} (or 3×10^{-18} erg s^{-1} cm^{-2} arcsec^{-2} in terms of line emission). The purpose of the chapter is to describe the observation and the reduction procedure which allowed us to get a photon-noise limited image in Hα in a large FOV (8′diameter) around the galaxy. The resulting signals are interpreted in

[1] `http://www.gtc.iac.es/`

terms of the gas in the CGM and IGM around the galaxy, as well as high redshift contaminants.

The chapter is organized as follows: Sect. 3.2 is devoted to estimate the level of the weak Hα signal to be expected. Sect. 3.3.1 shows how those signals are within reach of the current telescopes within reasonable observing time. The actual GTC observations are described in Sect. 3.3.2 and the data reduction in Sect. 3.3.3. The methods used for the detection and characterization of the emission line-dominated blobs are explained in Sect. 3.4. The measured properties are described in Sect. 3.5. Finally, the main results are summarized and discussed in Sects. 3.6, 3.7.

3.2 Expected Hα signal

The section is devoted to work out the Hα emission to be expected in the CGM and IGM around local galaxies. The estimates are very uncertain, but they all converge to provide a level of emission detectable in a reasonable integration time with 10-m class telescopes.

Table 3.1 summarizes the expected signal under various circumstances and approximations as explained in the next paragraphs.

3.2.1 Re-scaling of the Lyα signals observed at high redshift.

As we explain in Sect. 3.1, diffuse Lyα emission around galaxies is often detected at high redshift. Going to the local Universe and using Hα rather than Lyα have pros and cons. Among the cons, the wide ratio between Lyα and Hα (ϵ). It is expected to be 8.7 if the lines are produced by recombination of electrons and protons (e.g., Miller 1974), and it is observed to be between 0.5 and 8.7 in high redshift star-forming galaxies (Hayes et al. 2010), between 1.5 and 10 in galaxy cluster diffuse emission (Hu 1992), around 5 in high redshift Lyα blobs (Leibler et al. 2018), between 0.2 and 20 in local star-forming galaxies (Atek et al. 2009), and around one in quasars (Baldwin 1977). The emissivity is expected to increase with density (e.g., Osterbrock 1974), therefore, another con has to do with the evolution of the cosmic web gas that decreases in density (ρ_g) with decreasing redshift (z) following the global expansion of the universe (e.g., van de Voort & Schaye 2012), i.e,

$$\rho_g \propto (1+z)^3. \tag{3.1}$$

Among the pros, local galaxies are closer and the cosmological dimming helps us increasing the surface brightness by $(1+z)^4$ (e.g., Goerdt et al. 2010; Hogg 1999). In addition, Lyα photons are more easy to destroy than Hα

Table 3.1: Summary of the Hα signal to be expected in the local Universe.

Comment	Surface Brightness (10^{-18} erg s^{-1} cm^{-2} arcsec^{-2})	$m_{\rm AB}$[a] (mag arcsec^{-2})	Region[b]	Section[c]	Reference
Scaled Lyα observations	1 – 30	29.3 – 25.6	IGM	3.2.2	Cantalupo et al. (2014)
Scaled Hα observations	10	26.8	IGM	3.2.2	Leibler et al. (2018)
Fluorescence	0.01 – 10	34.2 – 26.8	IGM	3.2.3	Kollmeier et al. (2010)
CIB[d] Fluorescence	0.1 – 0.001	31.8 – 36.8	CGM	3.2.3	Bland-Hawthorn et al. (2017)
Gravity driven	5 – 0.09	27.5 – 31.9	CGM	3.2.5	Goerdt et al. (2010)
Gravity driven	2 – 0.001	28.5 – 36.8	CGM	3.2.5	Faucher-Giguère et al. (2010)
Gravity driven, $z = 0$	20 – 0.002	26.0 – 36.0	IGM	3.2.5	Furlanetto et al. (2003)
Mechanical Feedback	~ 1	~ 29.3	CGM	3.2.4	Mori et al. (2004)
Observed $z = 0$	≥ 0.5	...	CGM	3.2.6	Herenz et al. (2017)

[a] AB magnitudes when the Hα emission is observed through a color filter with 50 % peak transmission and 100 Å FWHM.
[b] Whether the signals correspond to the cirumgalactic medium (CGM) or the intergalactic medium (IGM).
[c] Section in the text where this estimate is discussed.
[d] Cosmic Ionizing Background.

photons (e.g., by dust absorption or collisional de-excitation). For the sake of having an order of magnitude estimate of the expected signal, lets assume that the emission roughly drops with the mean gas density of the Universe. Then the ratio between the Lyα surface brightness at z ($F_{Ly\alpha}[z]$) and the Hα surface brightness if the same structure evolves and is observed in the local universe ($F_{H\alpha}[0]$) would be,

$$F_{H\alpha}(0) = \frac{(1+z)^4}{\epsilon(1+z)^3} F_{Ly\alpha}(z) = \frac{1+z}{\epsilon} F_{Ly\alpha}(z). \tag{3.2}$$

Note that

$$F_{H\alpha}(0) \simeq F_{Ly\alpha}(z), \tag{3.3}$$

provided that z is on the range between 2 and 3, and ϵ (the ratio between Lyα and Hα) remains between 3 and 4, which is reasonable considering the range of redshifts where extended Lyα emission has been detected (see Sect. 3.2.2), and the observed ϵ referenced above.

There are two key assumptions determining Eq. (3.3), namely (1) the factor ϵ is not far from the value provided by recombination, and (2) the drop of emission following the mean density of the universe. The two of them are revised in the following sections depending on the Lyα emission mechanism.

3.2.2 Emission expected scaling the signal found by Cantalupo et al. (2014).

We use Cantalupo et al. (2014) as a reference to quantify the Lyα signals observed at z between 2 and 3, but similar results are obtained using any of the recent works that have detected diffuse Lyα emission (e.g., Martin et al. 2014; Wisotzki et al. 2016, 2018). The peak surface brightness of the Lyα structure detected by Cantalupo et al. (2014) is

$$F_{Ly\alpha}(3) \simeq 3 \times 10^{-17}\,\mathrm{erg\,s^{-1}\,cm^{-2}\,arcsec^{-2}} \equiv F_0. \tag{3.4}$$

The Lyα signal presents a range of values of around 30 therefore, considering Eq. (3.3), $F_{H\alpha}(0)$ is expected to be in between $F_0/30$ and F_0.

We will observe the Hα emission through a filter much broader than the line itself, therefore, for the sake of intuition, it is convenient to write the flux of the line in terms of magnitude per arcsec^2. An emission line of flux F_{λ_0} observed through a filter broader than the line and transmission T_λ, with an effective bandpass $\Delta\lambda$,

$$\Delta\lambda = \int T_\lambda d\lambda, \tag{3.5}$$

turns out to have an AB magnitude of

$$m_{\rm AB} = 25.6 - 2.5 \log \Big[\Big(\frac{\lambda_0}{6563\,\mathring{\rm A}} \Big)^2 \frac{F_{\lambda_0}}{F_0} \frac{T_{\lambda_0}}{0.5} \frac{100\,\mathring{\rm A}}{\Delta\lambda} \Big], \tag{3.6}$$

where λ_0 is the observed central wavelength of the spectral line, T_{λ_0} is the transmission of the filter at λ_0, and F_0 and $\Delta\lambda$ are defined in Eqs. (3.4) and (3.5), respectively. In a case of a Gaussian-shape filter of peak transmission 1, $\Delta\lambda$ is very close to the FWHM of the filter. The expression (3.6) has been deduced from the definition of AB magnitudes. Note that the SDSS magnitudes are close to AB magnitudes (e.g., Fukugita et al. 1996) therefore, $m_{\rm AB}$ can be ascribed to SDSS-r when observing Hα. Equations (3.4) and (3.6) with $\Delta\lambda = 100\,\mathring{\rm A}$, $T_{\lambda_0} = 0.5$, and λ_0 the Hα wavelength, give the range of magnitudes to be expected from scaling the Lyα signals found by Cantalupo et al. (2014), i.e.,

$$25.6 \leq m_{\rm AB} \leq 29.3. \tag{3.7}$$

These are the figures appearing in Table 3.1 for the signal detected by Cantalupo et al. (2014), scaled down to the local universe and Hα using Eq. (3.3).

Leibler et al. (2018) have recently measured the Hα emission corresponding to the Lyα nebula detected by Cantalupo et al. (2014). Hα is in the near infrared at the redshift of the source, so, they use the spectrograph MOSFIRE[2]. The Hα surface brightness is around $3 \times 10^{-18}\,{\rm erg\,s^{-1}\,cm^{-2}\,arcsec^{-2}}$, with an Ly$\alpha$ to Hα flux ratio of 5.5. This observational result is consistent with the above estimates. If we correct for the variation with redshift, the Hα signal would be around $10^{-17}\,{\rm erg\,s^{-1}\,cm^{-2}\,arcsec^{-2}}$, as we include in Table 3.1.

3.2.3 Fluorescence of UV photons

UV photons from the cosmological background or from nearby sources are expected to photoionize the gas clouds existing in the CGM and IGM. The recombination of the photoionized H atoms produces Lyα photons that, after internal scattering, can scape the cloud producing a diffuse Lyα signal that traces the cloud. In optically thick clouds, the mechanism very effectively transforms the UV photons into Lyα photons, with an efficiency approaching one (e.g., Gould & Weinberg 1996). This whole process is often refereed to as *fluorescence* (e.g., Cantalupo et al. 2005; Gould & Weinberg 1996). Since photons are finally created through recombination, fluorescence produces all the other H recombination lines, including Hα.

[2] `https://irlab.astro.ucla.edu/mosfire/`

There are works estimating the Lyα signals expected due to illumination by the cosmic UV background or nearby quasars. Using cosmological simulations of gas clouds at $z \simeq 3$, Cantalupo et al. (2005) work out the Lyα signals, that turn out to be in the range between $3 \times 10^{-20}\,\mathrm{erg\,s^{-1}\,cm^{-2}\,arcsec^{-2}}$ and a few times $10^{-19}\,\mathrm{erg\,s^{-1}\,cm^{-2}\,arcsec^{-2}}$, the latter corresponding to the presence of a nearby quasar. Kollmeier et al. (2010) carry out a similar exercise rendering larger signals that can reach a value of $10^{-17}\,\mathrm{erg\,s^{-1}\,cm^{-2}\,arcsec^{-2}}$ if the quasar illumination is strong enough. The signal excited by the UV background is in the range of $10^{-20}\,\mathrm{erg\,s^{-1}\,cm^{-2}\,arcsec^{-2}}$. For more references on the estimates see, e.g., Cantalupo et al. (2012).

The scaling between the fluxes in Hα and Lyα worked out in Sect. 3.2.1 can also be used in this case to render the range of expected Hα fluxes (and magnitudes) included in Table 3.1.

Bland-Hawthorn et al. (2017) model the Hα emission in the outer gas disk of milky-way like galaxies produced by fluorescence of photons of the cosmic ionizing background. The estimated signals are in the range between 10^{-19}–$10^{-21}\,\mathrm{erg\,s^{-1}\,cm^{-2}\,arcsec^{-2}}$.

3.2.4 Emission driven by mechanical feedback from galaxies.

The mechanical energy injected by galaxy winds may also lead to shocks that are a powerful source of ionizing photons produced in the hot post shock plasma as it cools down (e.g., Dopita & Sutherland 1995). They may be responsible for some of the extended Lyα emission found at z in the range $2-3$ (e.g., Taniguchi & Shioya 2000; Ohyama et al. 2003). Mori et al. (e.g., 2004) model the winds produced by SN explosions in primitive galaxies at $z = 3$, and work out the emission properties assuming an optically thin gas in collisional-ionization equilibrium. The total flux in Lyα is around $10^{-16}\,\mathrm{erg\,sec^{-1}\,cm^{-2}}$, and it is emitted in region of around 10 arcsec, which renders a surface flux density of some $10^{-18}\,\mathrm{erg\,sec^{-1}\,cm^{-2}\,arcsec^{-2}}$. This is also the level of signals expected in the local universe when observed in Hα – Eq. (3.3). The actual values are included in Table 3.1.

3.2.5 Gravity driven emission

The potential energy of the gas falling into a gravitational well is transformed into kinetic and thermal energy, and has to be released for the gas to become gravitationally bound. This energy is partly radiated away in the form of H recombination lines (Dijkstra & Loeb 2009).

There are several studies in the literature that model this process and the

resulting line emission. We take the work by Goerdt et al. (2010) as reference. They use cosmological numerical simulations of galaxy formation to work out the Lyα flux to be expected from the gas streams that fed galaxies at high z. UV background excitation, collisions with free electrons, and dust attenuation are all included when computing the Lyα emission. The emission is mainly driven by the excitation produced by collisions with electrons since the filaments are thick enough to be shielded from the UV background. Most of the Lyα emission comes from narrow extended (50-100 kpc), partly clumpy, inflowing, cold streams of $\sim 10^4$ K that feed the growing galaxies. The predicted morphology is irregular, with dense clumps and elongated extensions. The typical surface brightness increases with decreasing distance from the halo centre. The peak surface brightness is 2×10^{-17} erg s^{-1} cm^{-2} arcsec^{-2} for MW-like haloes at $z = 2.5$, with typical signals in the range from 3×10^{-17} to 5×10^{-19} erg s^{-1} cm^{-2} arcsec^{-2}. No estimate for the Hα flux is given, however, they mention *other H emission lines are expected to be two orders of magnitude less luminous in our model.* Hα is expected to be the strongest one so we assume ϵ (i.e. the ratio between the emissivities in Lyα and Hα) to be 20. Using this value for ϵ in Eq. (3.2),

$$5 \times 10^{-18} \leq F_{\mathrm{H}\alpha}(0) \leq 9 \times 10^{-20}, \tag{3.8}$$

in units of erg s^{-1} cm^{-2} arcsec^{-2}. These values, together with the corresponding magnitudes, are included in Table 3.1.

Faucher-Giguère et al. (2010) carry out a similar simulation but with more sophisticated radiative transfer. As in the work by Goerdt et al. (2010), the signals are concentrated toward the centers of the dark matter haloes hosting galaxies, but some also emerge from the IGM. Depending on the treatment of the radiative transfer, the predicted Lyα signals can vary from 10^{-17} to 5×10^{-21} erg s^{-1} cm^{-2} arcsec^{-2}. Rescaling to Hα and to the local Universe, as we did for Goerdt et al., the expected Hα flux is in the range 2×10^{-18} to 10^{-21} erg s^{-1} cm^{-2} arcsec^{-2}. These values and the corresponding AB magnitudes are included in Table 3.1.

Furlanetto et al. (2003) pioneered the field. They presented predictions corresponding to the local Universe ($z \simeq 0.15$), so no need to apply high-z corrections. In their Fig. 2 they show structures producing between 10^2 to 10^6 photons cm^{-2} s^{-1} sr^{-1}, which properly transformed into the usual units render $F_{\mathrm{Ly}\alpha}(0)$ in the range between 4×10^{-20} and 4×10^{-16} erg s^{-1} cm^{-2} arcsec^{-2}. Correcting only for the ratio of emissivities between Hα and Lyα, $F_{\mathrm{H}\alpha}(0)$ turns out to be between 2×10^{-21} and 2×10^{-17} erg s^{-1} cm^{-2} arcsec^{-2}. These fluxes and the corresponding AB magnitudes are included in Table 3.1.

Likewise, Rosdahl & Blaizot (2012) model the Lyα emission in numerical simulations. The emitting gas is at the center of the dark matter haloes radiating away the excess of gravitational energy explicitly modeled in the previous works. The expected signals are similar to the ones resulting from the previous simulations.

3.2.6 Observed diffuse Hα emission in the local Universe

The existing Hα surveys in the local Universe have a surface brightness limit insufficient to detect the faint signals to be expected: equal or fainter than $10^{-17}\,\mathrm{erg\,s^{-1}\,cm^{-2}\,arcsec^{-2}}$, equivalent to a surface brightness of around 26.5 (Table 3.1). This level is not within reach of the existing surveys (e.g., Moss et al. 1988; James et al. 2004; Epinat et al. 2008; Dale et al. 2008; Jaiswal & Omar 2016). Moreover, some of them are focused on the emission of the Milky Way, either diffuse (e.g., Gaustad et al. 2001) or its point-like sources (e.g. Barentsen et al. 2014).

Despite the fact that general purpouse surveys do not suffice to detect the expected Hα signals, diffuse emission have been detected around individual galaxies when the observation is deep enough. As part of the LARS[3] project to study the visibility, strength, and scape fraction of the Lyα photons in 14 galaxies the local universe, Östlin et al. (2014) and Hayes et al. (2014) obtained deep Hα maps hinting at extended emission. Although the sensitivity is good (around $10^{-18}\,\mathrm{erg\,s^{-1}\,cm^{-2}\,arcsec^{-2}}$, Hayes et al. 2013), the field-of-view includes only a few effective radii around the galaxies, therefore, missing most of the CGM and the full IGM. Flux-wise, the integrated emission observed in Hα and Lyα are comparable.

Herenz et al. (2017) detect filaments of ionised gas in the CGM of the extremely metal-poor galaxy SBS 0335-052E. The features are detected in Hα and [O III]λ5007 down to a limiting surface-brightness of 5×10^{-19} erg s^{-1} cm^{-2} arcsec^{-2}. The galaxy diameter is around 3 kpc, with the filaments extending more than 9 kpc and connecting seamlessly in velocity space to the galaxy. Extended Hα emission at a level of $5\times10^{-18}\,\mathrm{erg\,s^{-1}\,cm^{-2}\,arcsec^{-2}}$ has been found around 3 dwarf galaxies by Lee et al. (2016). Cheung et al. (2016) find a lone Hα emitting blob next to an evolved galaxy with a signal around $3\times10^{-18}\,\mathrm{erg\,s^{-1}\,cm^{-2}\,arcsec^{-2}}$. A value of flux and magnitude representative of these observations is included in Table 3.1.

[3]Lyα Reference Sample (Östlin et al. 2014).

3.3 Observations and Data reduction

3.3.1 Global Strategy

Our goal is to detect the Hα emission of the CGM around an XMP galaxy using OSIRIS@GTC[4]. In order to isolate the line emission from the continuum emission, we subtract a broad-band (BB) image from a medium-band (MB) image.

The medium-band is chosen to select the line emission of Hα at the redshift of the galaxy. The broad-band contains the continuum and a very diluted Hα line. The images will be taken consecutively, alternating between MB and BB to ensure that they have the same sky conditions, so that the subtraction would leave residuals as small as possible.

The difference between MB and BB leaves the Hα emission plus the noise of the sky signal. If we assume that the sky emission varies by 0.01 mag in between MB and BB images (typical value of sky brightness variations on a ten minute timescale on a photometric night at the ORM[5]), then the residual sky would have a magnitude of around 27. We also use the technique of dithering and rotation of the FOV, which allows a better modelling of the sky emission. This technique has been proven to allow GTC to reach 31.5 mag arcsec^{-2} with a total of $\sim$8h exposure time in BB filters (Trujillo & Fliri 2016).

3.3.2 Observations

For this study I pre-selected XMP galaxies based mostly on morphological criteria (detailed information about this selection is given in Appendix A). Then, after a first morphological screening that pinpoints clumpy galaxies or galaxies with distorted shape, I chose those satisfying the following conditions: detected HI emission around them (e.g., Filho et al. 2013), adequate redshift for the available SHARDS filters (Pérez-González et al. 2013), observable during the granted observing time, and no companions. I also looked into dust maps[6] and infrared maps, in order to avoid galactic cirrus and to have the minimal extinction in the field around the target. Another constrain is avoiding saturation of bright stars in the field of OSIRIS (7.8 $\times$ 7.8 arcmin^2), which is quite difficult as a star of $m_r = 19$ mag saturates in 110 s, when observed with a seeing of 1.2 arcsec. Another factor to take into account is that the nominal wavelength of the narrow filters changes along the FOV, so the range of redshifts available for

[4]http://www.gtc.iac.es/instruments/osiris/
[5]http://vivaldi.ll.iac.es/OOCC/orm-sky-brightness/
[6]http://irsa.ipac.caltech.edu/applications/DUST/

observations is reduced, in order to ensure that the Hα line does not get out of filter at the border of the FOV (see Pérez-González et al. 2013 for details).

I downloaded the deep images of IAC Stripe 82 Legacy Project (Fliri & Trujillo 2016) of the pre-selected XMP galaxies fulfilling the above criteria. In these images we searched for peculiar morphologies and hints of diffuse signal around the XMP galaxy. We rejected galaxies in which one could see galactic cirrus, as their presence complicates the detection of the diffuse emission since the sky should be as smooth as possible. The one galaxy that satisfies all the above conditions is the target of our observation: SDSS J003741.11+003320.2, which we refer to as UM 260. The galaxy is shown in Fig. 3.1. Table 3.2 contains its main physical properties.

Table 3.2: Properties of UM 260.

Major axis[a] [arcsec]	4.75
Minor axis[a] [arcsec]	3.66
r (SDSS Model) AB[b] [mag]	18.389 ± 0.013
Redshift[a]	0.01447
Scale[c] [kpc arcsec^{-1}]	0.301
Effective radius[d] [arcsec]	1.70 ± 0.03
A[e] [arcsec]	1.90
B[e] [arcsec]	1.55
θ_0^e [degrees]	−13.32
log(SFR[M$_\odot$ yr^{-1}])[f]	$-1.583^{+0.125}_{-0.055}$

[a,b] From the NASA/IPAC Extragalactic Database (NED).
[b] At isophotal 25.0 mag arcsec^{-2}.
[c] Scale obtained from distance as given in Table A.1.
[d] Parameter petroR50 measured in r filter, gathered from SDSS DR12. We also measured the effective radius in the BB image and the result is 1.8 arcsec.
[e] Parameters obtained with SExtractor using the MB image. A is the semi-major axis, B the semi-minor axis and θ_0 the angle of the ellipse fitted to the isophots.
[f] From Chang et al. (2015).

The observations were taken with the instrument OSIRIS (Optical System for Imaging and low-Intermediate-Resolution Integrated Spectroscopy; Cepa et al. 2000, 2003) at GTC (Gran Telescopio de Canarias). The FOV of the instrument is $7.8' \times 7.8'$ (unvignetted) splitted in two CCDs. The average seeing during the observations was 1 arcsec. The images were obtained with two filters: SDSS r for the continuum and the medium-band SHARDS U670/17 (Pérez-González et al. 2013) for the line emission. The total exposure time (6.85 hours) is divided between the two filters in a ratio BB to MB 1/3, in order to

maximize the signal to noise ratio in the image difference between the two filters (see Appendix 3.8.1).

The observational strategy is similar to that followed by Trujillo & Fliri (2016). We performed a dithering pattern of five points: 4 points in the corners of a 90 arcsec side square and one in the center. In each dithering step, images of both filters were taken: 125 seconds of exposure time for SDSS r and 423 seconds for SHARDS U670/17. At the end of the dithering pattern, short exposures of 3 and 9 seconds were taken in the two bands, to avoid saturation of the bright objects in the FOV. We repeated the dithering pattern 9 times, rotating the FOV by 30 degrees each time. The combination of dithering and rotation allows for a better estimation of the sky background. Completing the observation required three different nights explicitly, $08-09$, $09-10$, $11-12$ of September 2015.

3.3.3 Data reduction

I explain the data reduction in detail since it is one of the critical points of the work, and the technique to push the depth of astronomical images to the limit is of general interest. Most of it has been adapted from Trujillo & Fliri (2016) with some changes for treating our MB images.

Bias subtraction and flat-field correction

These steps of the data reduction were done with the package PyRAF [7]. We carried out a standard bias subtraction: first combining the bias images of every night and CCD, and then subtracting the masterbias from the science images of the corresponding night and CCD.

Masterflats were computed from the sky in the science images. First, we need to mask the objects in the images. For that we use the program SExtractor (Bertin & Arnouts 1996), which makes a catalogue of all the sources in the images. One of the outputs of the program is an image with the sources, in which the background is set to zero. We invert this image to produce an object mask and expand it with a gaussian filter. Then we apply the object mask to the science images and normalize them to the mean value around the center of the FOV of the instrument. Then we combine the background-only normalized science images of the same filter, CCD and observing night to make the flat.

The above procedure works well for the flats of the BB images. However, the MB filter suffers from variation of the CWL (central wavelength) across the

[7] PyRAF is a product of the Space Telescope Science Institute, which is operated by AURA for NASA http://www.stsci.edu/institute/software_hardware/pyraf/

FOV (see Pérez-González et al. 2013) and due to this effect there is a variable contamination from sky emission lines on the CCD. Structures associated with sky emission appear in all the science images in the same physical position regardless of the sky coordinates (although the flux may vary in time), and they complicate the construction of the flat images. The purpose of flatfielding is to correct the different sensibility of the pixels in the CCD, so we have to remove this contamination from the flats because it does not represent an increase in sensibility, but an increase in sky emission. In order to remove this effect I perform an illumination correction on the MB flat-fielded images. First, the MB flat was spatially smoothed. Then, the MB flat was divided by the smoothed flat. Thus, I remove the large scale patterns of the flat that belong to sky emission and leave the pixel-to-pixel variations that reflect the differences in sensibility of the CCD and the SHARDS filter. Then, the ratio is multiplied by the large scale patterns of the broad-band filter, which represent variations in efficiency of the whole CCD plus telescope (e.g., vignetting).

The vignetting pattern changes slightly every time we rotate the FOV. Therefore, I made a flat for each observing block. Which, consecuently, has lower signal-to-noise ratio than the flats-per-night. So an additional small correction was introduced in the same way as the illumination correction, leaving the pixel-to pixel transmission variation from the flat-per-night and, on top of it, adding the large-scale vignetting pattern of a flat per observing block. I also removed pixels in the flats with a transmission below 90 % and all the satellite tracks that crossed the images. Finally, I applied the corresponding flats to all the science images.

Astrometric calibration

As we want to combine all the images together, the astrometry of the images needs to be calibrated. In order to do it, I use the program SCAMP (Bertin 2006). This program needs a catalogue of the positions of the objects in each image. This catalogue was obtained using SExtractor. It also needs a reference catalogue of all the stars in the full FOV. The catalogue used for reference was the stellar catalogue in SDSS-DR9. After gathering all the catalogues, we run SCAMP on all the science images. SCAMP provides a new header for each image with the new astrometric solution. The accuracy of the astrometric calibration is good up to 0.17 arcsec, as given by the output of SCAMP. This is negligible small compared with our spatial resolution ($\simeq$ 1 arcsec).

Photometric calibration

The photometric calibration of the images was carried out in the way that a hypothetical star with a flat spectra in the wavelength range of the SDSS r filter would have the same magnitudes in the medium-band (MB) and the broad-band (BB) images. The catalogue of sources in each science image was obtained with SExtractor and then purged out of objects without good photometry. Then the catalogue of sources in each science image was cross-matched with the SDSS star catalogue employed in the astrometric calibration, which has the magnitudes of the stars in the SDSS r filter. The cross-match employed the program stilts (Taylor 2006) using the coordinates of the objects. The photometry constrains employed in the cross-matching were the following:

- no SExtractor photometry flags,
- SExtractor measured FWHM less than 7 pixels (1.75 arcsec),
- score distance of the cross-matching less than 0.2 arcsec (accuracy of the astrometry),
- SExtractor measured instrumental magnitude greater than -16 (to avoid non-lineal effects of too bright saturated stars),
- photometry errors in SExtractor measured magnitudes less than 0.05 mag.

The magnitude zeropoint of each image was calculated as the median of the difference between the magnitude of the stars in the source and the reference catalogues. This is an iterative process in which I remove the points above 3 times the median absolute deviation (MAD), and calculating the median and MAD again until the MAD converges. The value of the median after MAD converges is the magnitude zeropoint of the image and we correct each image for its corresponding zeropoint. After this correction the zeropoint of the images is zero. In order to avoid working with very small numbers that could affect the rest of the data reduction, I subtracted 32 magnitudes from each image, leaving the images with a common zeropoint of 32 magnitudes.

On average, we used 31 stars on each image, and the resulting photometric calibration is good within 0.15 mag. This value is calculated as the median of the MAD of each zeropoint estimation.

Background subtraction

I estimated the background level by taking random samples from the science images, in which I previously masked the objects using SExtractor. The samples are the mean of the signal inside boxes of size 10 arcsec (BB) or 1 arcsec (MB). The boxes are smaller in MB science images because it resulted in a better fit of the sky background. The total number of samples is around 10^4 in each MB and BB image. For the BB images, I used a constant sky model, so I took the median of the samples. For the MB images, I fitted a 4 degree polynomial surface to the samples, which I found to fit best the sky contamination. Then, I subtracted the sky model from the science images.

Combination of images

The combination of images into a mosaic was done using the program Swarp (Bertin et al. 2002). This program resamples and co-adds the background subtracted images, with the new astrometry header produced by SCAMP. The used sampling algorithm is LANCZOS3 and the combination was done with the median. I also used the bad pixel and satellite masks, to remove them from the final combined mosaic. Figure 3.2 shows the resulting MB mosaic.

The median FWHM of the stars in the combined image is 1.3 arcsec for BB and 1.4 arcsec for MB. These numbers were calculated using the star catalogue of the photometric calibration. This catalogue contains the FWHM of the objects measured by SExtractor. Then the median FWHM of the stars in the MB and BB mosaic was calculated.

Estimation of magnitude limits

Following Trujillo & Fliri (2016), we estimated the magnitude limit randomly placing 10^5 10 arcsec square apertures on the sky, and then calculating the standard deviation of the total flux within the apertures divided by the total surface of the aperture in arcsec^2. This quantity corresponds to $\overline{S_A}$ in Eq. (3.38) (see Appendix 3.8.2) when the aperture A is 10 arcsec. The magnitude corresponding to 3 times this standard deviation is the magnitude limit. The magnitude limits thus computed are 28.8 mag arcsec^{-2} in the BB filter and 28.2 mag arcsec^{-2} in the MB filter. The same procedure applied to the image resulting from subtracting the BB image from the MB image (filter difference image) renders a magnitude limit of 28.6 mag arcsec^{-2}.

We also calculated the 1σ magnitude limit with apertures of 1 arcsec to compare with the OSIRIS@GTC exposure time calculator. The values are, 29.0 mag arcsec^{-2} in the BB filter, 28.8 mag arcsec^{-2} in the MB filter and

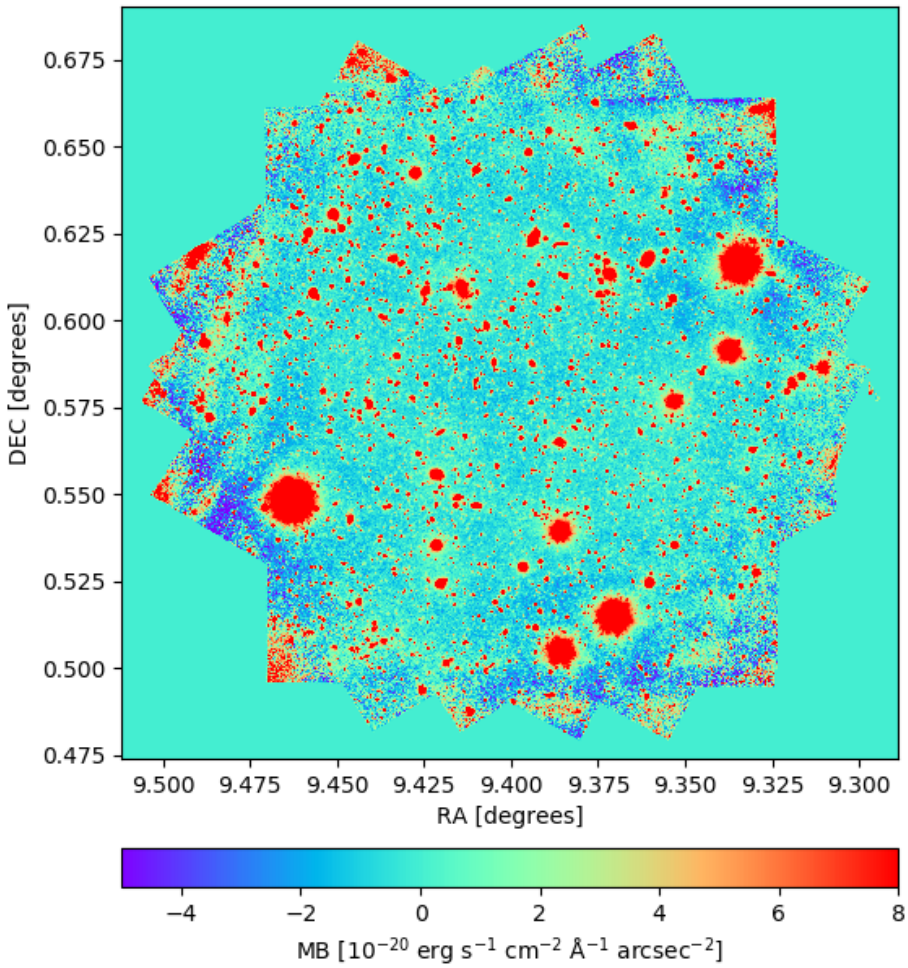

Figure 3.2: Full FOV of the combined mosaic. The color code shows the MB flux. The mosaic is noisier at the edges because fewer images contribute.

28.7 mag arcsec^{-2} in the filter difference image. These magnitude limits are fainter than the previous ones because they are calculated with 1σ instead of 3σ, even though the area of the aperture decreases. Considering that in the filter difference image much of the systematics error are removed, this is the closest value to the value given by the exposure time calculator.

For the exposure time calculator we use the following parameters[8]: broad-

[8]Other parameters used in the exposure time calculator (common for both filters) are the following: extended source, seeing 1 arcsec, airmass 1.3, dark moon, binning 2x2.

band filter r' and 45 exposures of 125 s for the BB image. For the MB image: a narrow filter with central wavelength 6700, filter width 160, filter transmission 1.0 and 45 exposures of 423 s. The exposure time calculator returns a signal to noise of 1 per arcsec^2 for a source of magnitude 29.6 in BB settings, and of magnitude 29 in MB settings. The magnitude limit equivalent to the difference MB − BB is 28.84 mag.

Absolute flux units and construction of the Hα image

Using the definition of AB magnitudes, and the fact that we added to the MB and BB images a zeropoint of 32 magnitudes, we can convert the units of the images from counts to erg s^{-1} cm^{-2} Å^{-1}. The procedure works as follows.

The units of the BB and MB images after the photometric calibration are still in counts f_c. First, the artificial zeropoint of 32 magnitudes that we introduced in the photometric calibration needs to be removed. The following equation gives us the present relation between the counts f_c and the magnitudes in the images,

$$m_{\rm AB} = -2.5\log(f_c) + 32. \tag{3.9}$$

The images are calibrated in terms of AB magnitudes ($\rm m_{AB}$), which are approximately the units of the SDSS star catalogue used in the photometric calibration (Fukugita et al. 1996). Using the definition of AB magnitudes (Oke 1974) and the conversion from the the flux per unit of frequency to the flux per unit of wavelength, we obtain the flux in units of erg s^{-1} cm^{-2} Å^{-1} (f_λ),

$$\begin{aligned} m_{\rm AB} &= -2.5\log(f_\nu/3631[\rm Jy]) = \\ &= -2.5\log\left[(\lambda_o^2/c)(f_\lambda/3631\times10^{-23})\right], \end{aligned} \tag{3.10}$$

where f_ν is the flux per unit of frequency in Jy, λ_o is the central wavelength of each filter in Å, c is the velocity of light in cm s^{-1}, and f_λ is the flux per unit of wavelength in cgs units. Combining Eqs. (3.9) and (3.10) we get,

$$I_i \equiv f_\lambda = f_c \times 10^{-0.4\times32}\ (c/\lambda_o^2)\ 3631\times10^{-23} \tag{3.11}$$

which is the conversion factor from counts f_c of the photometric calibration to flux units in erg s^{-1} cm^{-2} Å^{-1} f_λ. From this point on, I_i is used to represent the flux in cgs units per pixel. Eq. (3.11) is applied to the MB and BB images.

To have an image of the line emission at the redshift of the galaxy, we subtracted MB − BB. Equation (3.11) provides the corresponding f_λ, which represents the total flux per unit wavelength integrated over the filter. To

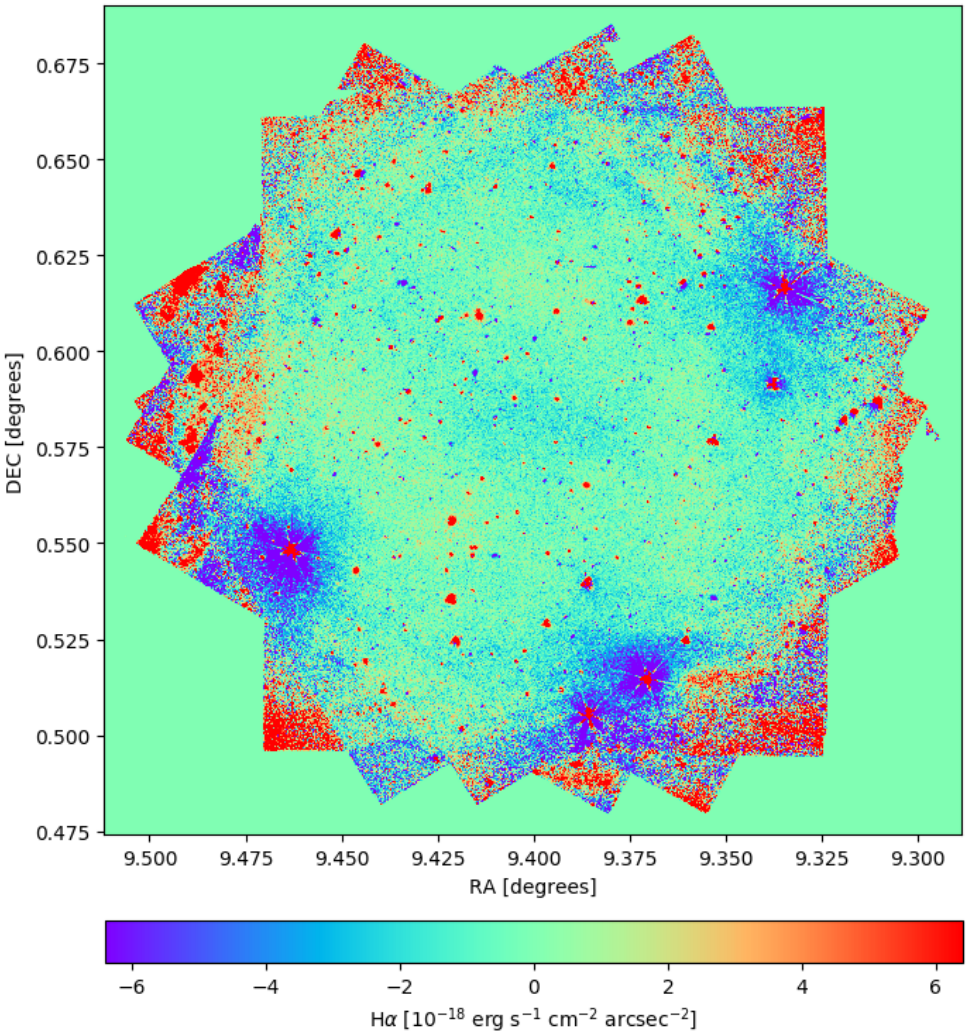

Figure 3.3: Full FOV of the combined mosaic. The color code shows the Hα flux. The mosaic is noisier at the edge because fewer images contribute. The center of the brightest stars appears in red due to saturation effects. The blue haze could be due to slightly broader PSF in the BB filter.

obtain the total flux in the emission line, it has to be multiplied by the bandpass of the MB filter. Thus, the resulting image has units of erg s^{-1} cm^{-2} pix^{-1}, and will be referred as HA image. The HA image is shown in Fig. 3.3.

In order to check the accuracy of our calibrations, I use the spectrum avail-

able for this galaxy on SDSS. I compared the integrated flux of Hα on the SDSS spectrum with the HA image using the same aperture as SDSS, i.e., a circle of 3 arcsec diameter. The fluxes are 10.4×10^{-15} erg s^{-1} cm^{-2} in SDSS and 7.3×10^{-15} erg s^{-1} cm^{-2} in the HA image. This $\sim$30% difference in the absolute photometry of the HA image is within the acceptable range, since the comparison has a number of uncertainties which have not been taken into account, like the true position and shape of the SDSS aperture. I also tried to repeat the same sanity check with other objects in the FOV of our images with spectra on SDSS. Unfortunately, none of the existing spectra had an emission line in the wavelength range of the MB filter, which is a requisite to show on the HA image.

3.4 Detection and characterization of emission line-dominated blobs

3.4.1 Detection: color cut argument

To identify the presence of emission line objects in the FOV, I use the ratio between the fluxes in the medium-band (MB) and the broad-band (BB) images. Artifacts have to be discarded, though. From now on the magnitudes in the MB and BB filters will be denoted as $m_{\rm MB}$ and $m_{\rm BB}$, respectively. A consequence of our photometric calibration is that stars without a flat spectrum in the range of the SDSS r filter will show residuals in $m_{\rm MB} - m_{\rm BB}$ correlated with their intrinsic color and, consequently, could be miss-identified as emission line objects. The standard stars used in the photometric calibration can be used to set a threshold on the measured $m_{\rm MB} - m_{\rm BB}$ color that guarantees the correct identification of objects with spectra dominated by emission lines.

I proceeded as follows. Figure 3.4 shows the existence of a correlation between the $m_{\rm MB} - m_{\rm BB}$ of stars in the field and their $g - r$ color ($r - i$ gives a similar relation). The residual $m_{\rm MB}$ and $m_{\rm BB}$ from stars are very different from the value $m_{\rm MB} - m_{\rm BB}$ of a well defined emission line blob which I use as the threshold to identify emission line objects in the field. Note that Figure 3.4 uses integrated aperture magnitudes, but the detection of the line emission will be based on the $m_{\rm MB} - m_{\rm BB}$ image. They are very similar because the size of the used apertures are comparable to the seeing, and the information of different pixels is correlated at the seeing scale.

The color image $m_{\rm MB} - m_{\rm BB}$ is shown in Fig. 3.5. The color image was smoothed with a gaussian filter of FWHM $\simeq$ 3.5 pix. This image was used in the procedure to identify emission line clump candidates. As a first step, I did

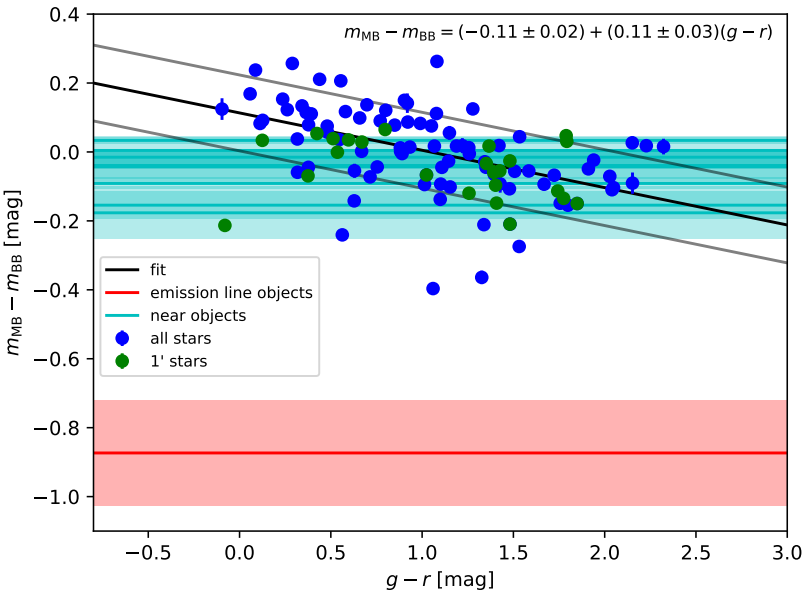

Figure 3.4: Residual color of stars in the field. It shows the relation between the measured color in our observations $m_{\rm MB} - m_{\rm BB}$ and the color $g - r$ obtained from SDSS. The correlation between these variables is due to the photometric calibration, which assumes the stars to have a wavelength independent continuum spectrum in the range of the SDSS r filter. The blue points are the standard stars used in the photometric calibration, whose magnitudes are extracted from the SDSS catalogue. The green points are a subset of the blue points, corresponding to the stars closer (distance < 1 arcmin) to the target galaxy. The solid black line and the gray lines show a linear fit to the blue points and its standard deviation, respectively. The equation of the fit is given on the top of the plot. The horizontal cyan lines and errorbars show the colors of other faint objects near the target galaxy not detected in SDSS. The red line and the errorbar (red band) show the color of a clear emission line blob near the target galaxy used for reference. The color of the blob differs significantly from the fake colors traced by the stars.

a visual inspection of the images using the *blink* option in the program DS9[9], alternating between BB and MB to identify emission features in the MB image which in $m_{\rm MB} - m_{\rm BB}$ satisfy the color cut mentioned above. As some objects may escape the visual inspection, I did a thorough search with SExtractor to obtain a list of line emitters. I run SExtractor on the $m_{\rm MB} - m_{\rm BB}$ image to get

[9]http://ds9.si.edu/site/Home.html

the center and the size of the most negative color objects. I selected the objects with a color $m_{\rm MB} - m_{\rm BB}$ smaller than -0.9, a criterion that discards stars (Fig. 3.4). I ordered them by size (big objects first) and did a visual inspection of the first 200. I compared the image of each object in our observations with their image in the IAC Stripe 82 Legacy Project (Fliri & Trujillo 2016). Although the images of IAC Stripe 82 are shallower than our observations, they provide additional information as they have more filters (u,g,r,i,z). If the identified object is bright enough to be seen in the IAC Stripe 82 survey, we can get a hint of the photometric redshift. Otherwise we can compare it with the objects around it. In the visual inspection, I noted that some objects were actually saturated stars, so I removed them from the list of 200 blobs. I also discarded blobs that were at the level of the noise or at the edge of the mosaic, where astrometric distortion could mislead the detection. I also added to the list one blob that was identified during the visual inspection and some blobs that were very near to the selected blobs. These blobs were not previously in the list because they were not big enough (they were smaller than the 200 objects in the initial list), but they pass the color cut. The final list of selected blobs contains 96 objects, which I will use for the rest of the chapter.

Figures (3.6), (3.7), (3.8), and (3.9) show examples of some of the identified blobs. For each emission line blob, eight snapshots are presented: (a) Hα flux (same color scale as Fig. 3.3), (b) $m_{\rm MB} - m_{\rm BB}$ color (same color scale as Fig. 3.5), (c) BB, the broad-band image, (d) MB, the medium-band image (the color scale is the same in these two images, to make it easier showing that the blobs have more emission in MB than in BB), (e) rdeep82, the combination of filters g, r, i from the IAC Stripe 82 Legacy Project given in arbitrary flux units, (f) the magnitude in the g filter from the IAC Stripe 82 Legacy Project, (g) the magnitude in the r filter from the IAC Stripe 82 Legacy Project, and (h) the magnitude in i filter from the IAC Stripe 82 Legacy Project (the color scale is the same in the last three images). All these snapshots have been spatially smoothed with a gaussian filter of FWHM $\simeq$ 3.5 pix. The FOV of these snapshots is 20×20 arcscec^2. I now discuss the examples shown in Figures (3.6) – (3.9):

- Object #7 (Fig. 3.6) has clear emission in the MB and BB images and it is the brightest blob in Hα of our sample. There are some hints of emission in the g, r and rdeep images of the IAC Stripe 82 Legacy Project.

- Object #9 (Fig. 3.7) has a barely detectable signal in the BB image which is off-center from the emission in the MB image. In the position of the BB continuum, there is a faint signal on the rdeep and i images of the IAC Stripe 82 Legacy Project.

- Object #16 (Fig. 3.8) has no detected emission in the BB image, but the signal in the MB image is clear. It is a candidate to be a pure emission line object. It is not detected on the images of the IAC Stripe 82 Legacy Project.
- Object #683 (Fig. 3.9) is the first emission blob we detected as it is very close to the target galaxy. In the Hα image it appears to be a filament connecting the blob and the target galaxy. It is not detected on the BB image neither on the images from the IAC Stripe 82 Legacy Project.

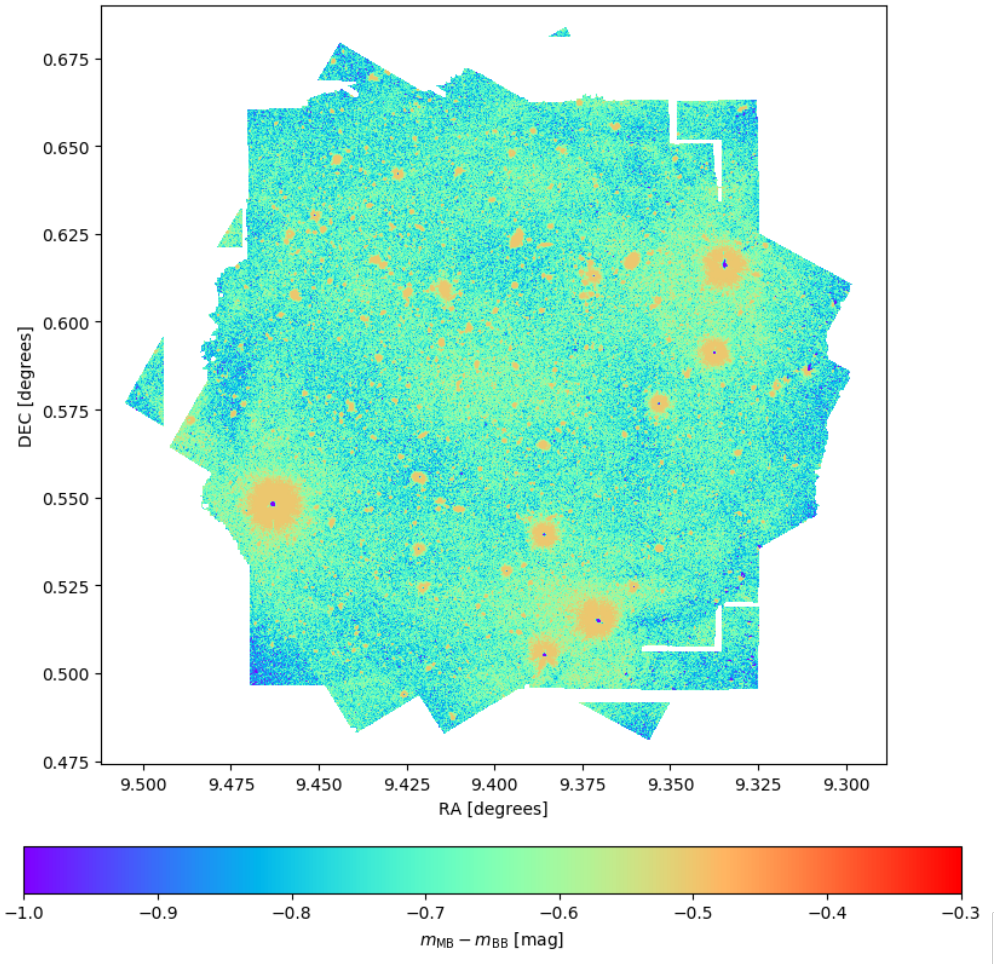

Figure 3.5: Full FOV of the combined mosaic. The color code shows $m_{\mathrm{MB}} - m_{\mathrm{BB}}$. The center of the brightest stars appears in blue due to saturation effects.

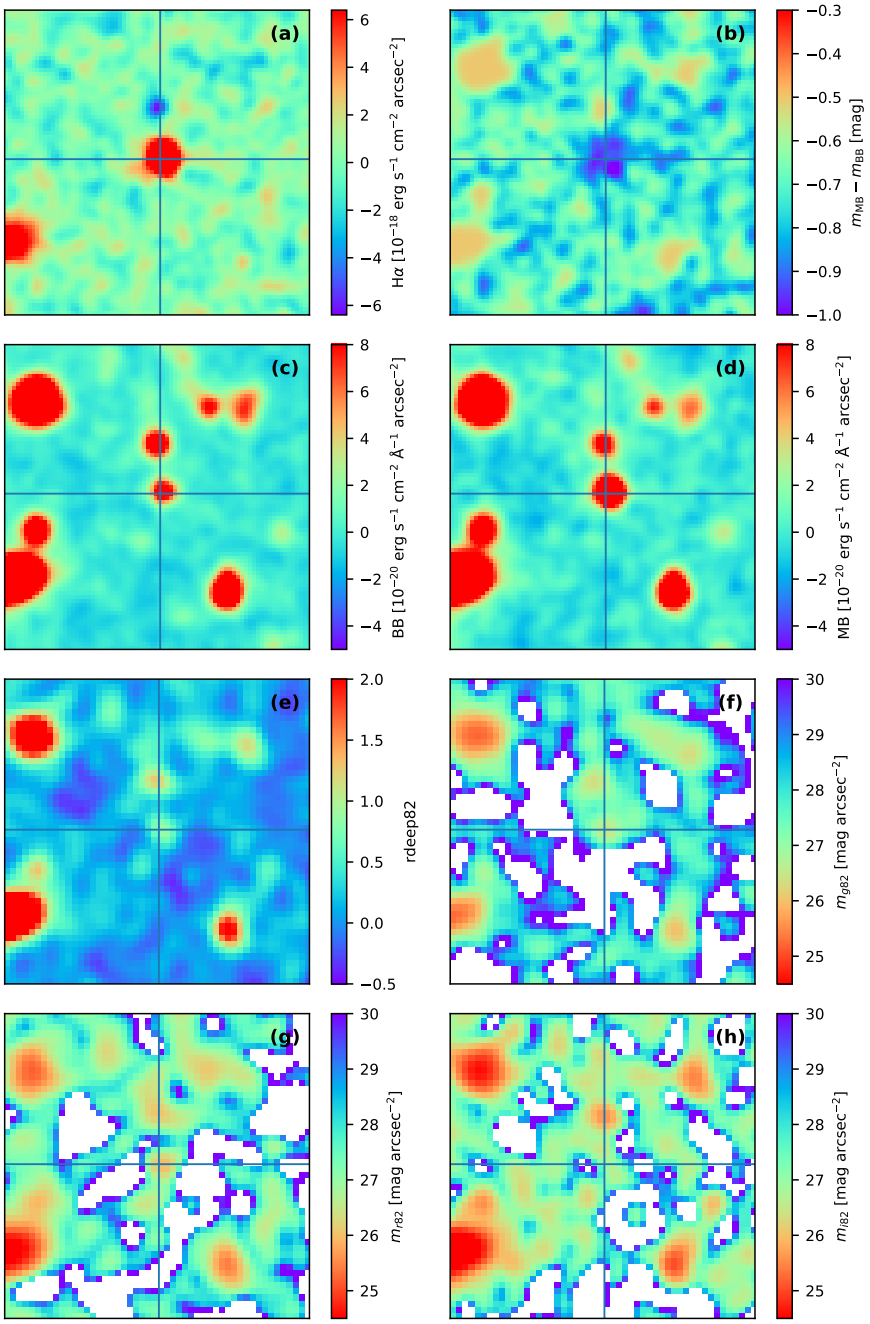

Figure 3.6: Object #7, RA: 0:37:38, DEC: +0:33:24. Caption continues in page 81.

Figure 3.6: This caption continues from the previous page. Each snapshot has been spatially smoothed with a gaussian filter of FWHM $\simeq$ 3.5 pix. The FOV of these snapshots is 20×20 arcscec^2. The FOV and the blue cross are centered on the coordinates of the identified blob, which were obtained from the $m_{\rm MB} - m_{\rm BB}$ color image. Eight snapshots are presented, in order: (a) Hα flux (same color scale as Fig. 3.3), (b) $m_{\rm MB} - m_{\rm BB}$ color (same color scale as Fig. 3.5), (c) BB, the broad-band image, (d) MB, the medium-band image (the color scale is the same in these two images, to make it easier showing that the blobs have more emission in MB than in BB), (e) rdeep82, the combination of filters g, r, i from the IAC Stripe 82 Legacy Project (the rdeep image is the average of the g, r, i images in arbitrary flux units), (f) the magnitude in the g filter from the IAC Stripe 82 Legacy Project, (g) the magnitude in the r filter from the IAC Stripe 82 Legacy Project, and (h) the magnitude in i filter from the IAC Stripe 82 Legacy Project (the color scale is the same in the three last images).

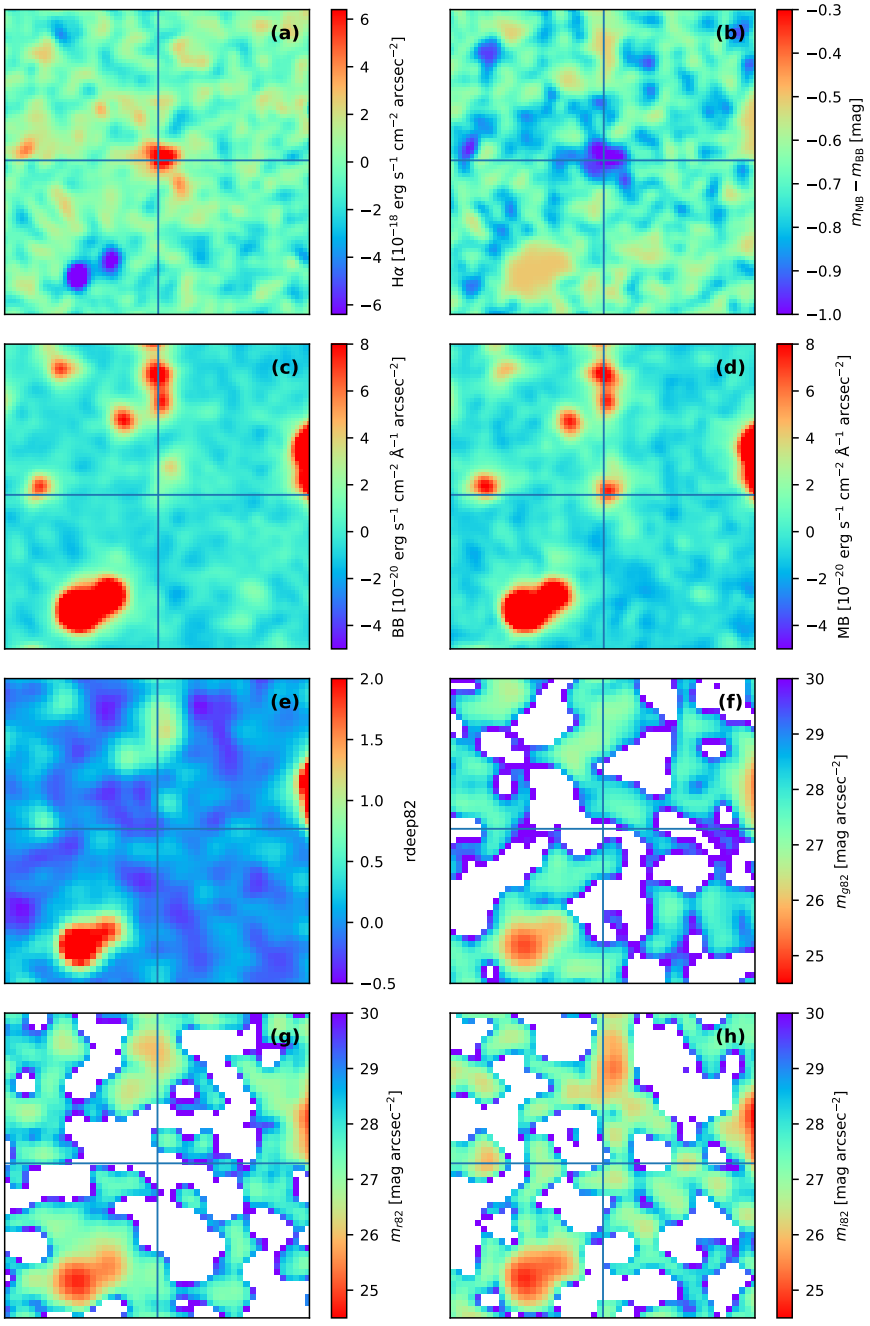

Figure 3.7: Object #9, RA: 0:37:30., DEC: +0:35:31. For the meaning of each panel, see caption of Fig. 3.6 in page 81.

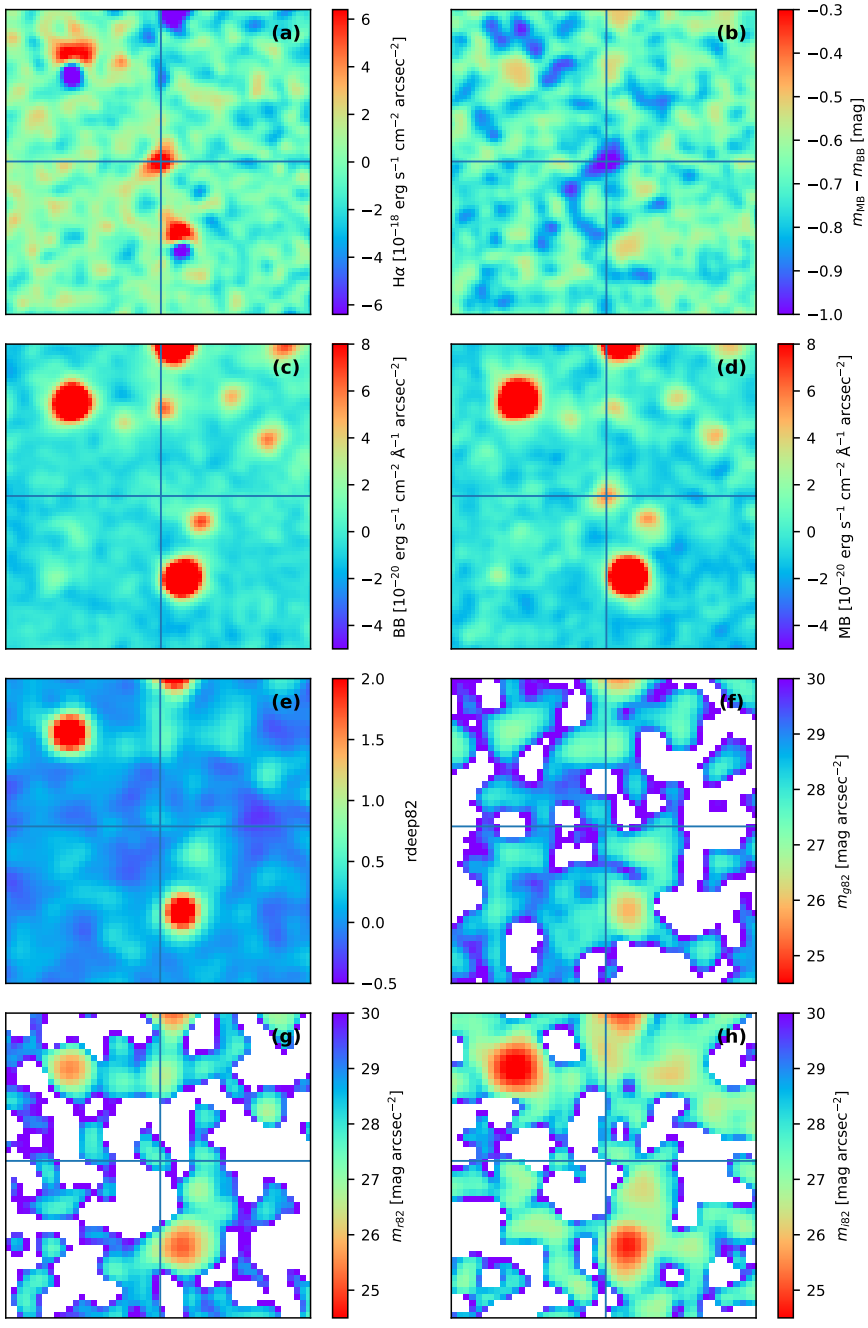

Figure 3.8: Object #16, RA: 0:37:29, DEC: +0:37:52. For the meaning of each panel, see caption of Fig. 3.6 in page 81.

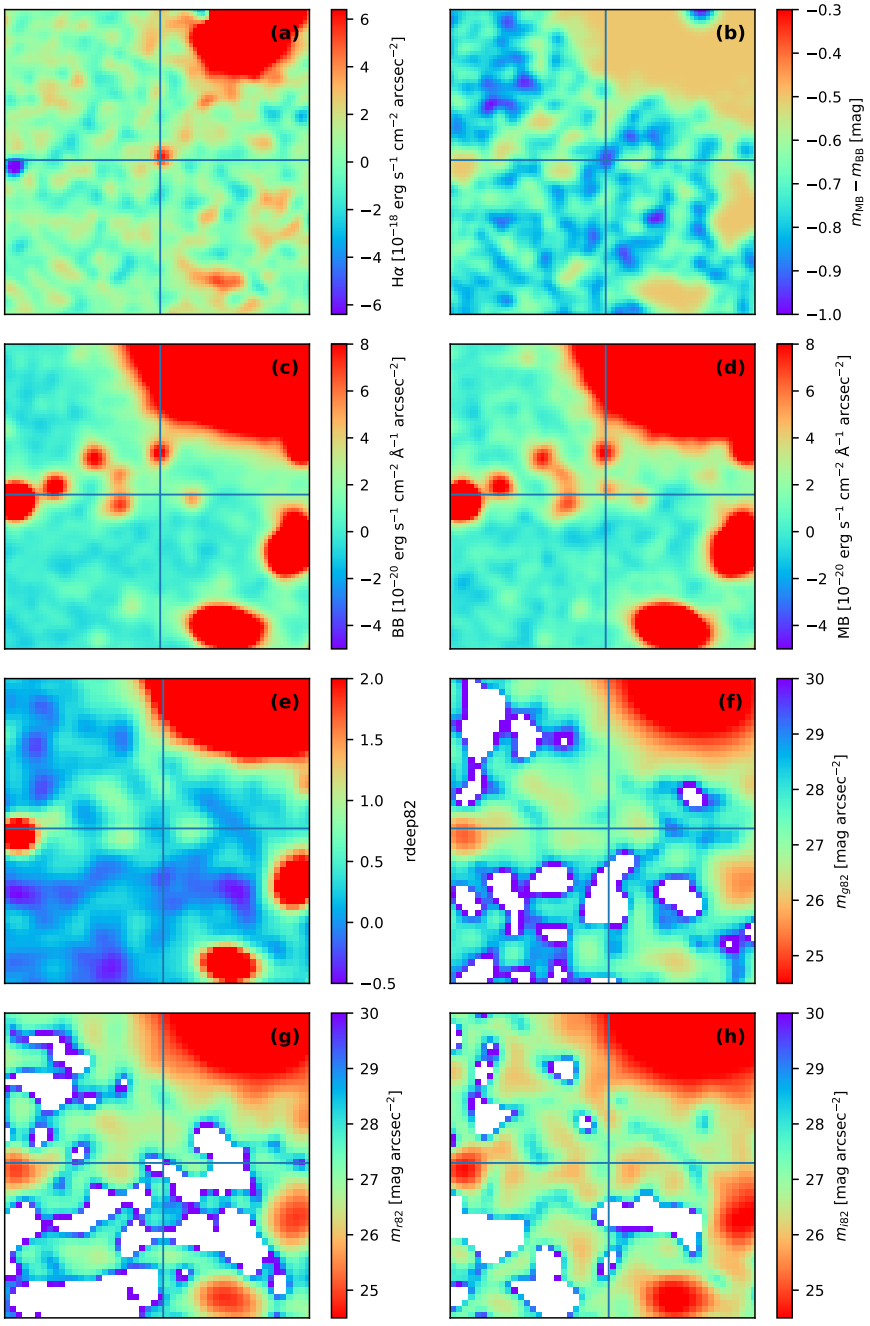

Figure 3.9: Object #683, RA: 0:37:41, DEC: +0:33:10. For the meaning of each panel, see caption of Fig. 3.6 in page 81.

3.4.2 Independent confirmation of blobs

In addition to the procedure described in Sect. 3.4.1, we use an alternative method to confirm the presence of emission line blobs in the Hα image. In the method explained in Sect. 3.4.1, $m_{\rm MB} - m_{\rm BB}$ has to be above a certain value, i.e., the ratio of fluxes has to be above a threshold. In this section, we explore the difference of the fluxes rather than the ratio. I use the Hα image to directly detect the emission line blobs. I use NoiseChisel (Akhlaghi & Ichikawa 2015), which is a program designed to detect low surface brightness objects. Is it similar in intention to SExtractor, but with a different approach. Instead of detecting signal above a noise threshold, NoiseChisel carves the signal out of the noise, using a combination of convolution, thresholding and erosion, based on the fact that the signal is spatially connected, while the noise is not. And it does not assume any particular shape for the detected object. In Appendix 3.8.3, I calculate the detection limit of NoiseChisel and find that it detects objects with a signal to noise ratio below 1, which is significantly smaller than the recommended parameter of SExtractor (Holwerda 2005).

I matched the list of blobs from the method described in Sect. 3.4.1 with the objects detected by NoiseChisel, and found a 63% agreement (61 blobs). 47 out of the 61 (77%) have enough S/N to be above our flux threshold in Hα (see Sect. 3.4.3). To compare with, SExtractor with the Hα image detects 25 blobs (26 %). 24 out of the 25 (96%) have enough S/N to be above our flux threshold in Hα. All these 24 blobs are also detected by NoiseChisel. So, NoiseChisel detects all the blobs (except one) detected by Sextractor, and more.

We conclude that a significant fraction of the blobs in Table 3.4 were also detected by the automatic algorithm NoiseChisel. This fact reinforces our confidence on the reduction and analysis carried out with the MB and BB GTC images.

3.4.3 Determination of photometric properties of the blobs

Table 3.4 lists the photometric properties of the detected blobs. This section explains how they were computed. The table will be described in detail at the end of this Section.

To calculate the flux of each individual emission line object (which I am calling a blob), I used several methods. First I used the dual mode of SExtractor. This mode allows to use different images for the detection and for the photometry. The detection image is the sum of the MB mosaic and the BB mosaic, and for the photometry, I used individually the Hα, MB and BB mosaic, to be sure that the same objects are detected on both images. I also used the

ASSOC parameters to provide SExtractor with a list of targets. This list, which has 96 objects, is derived in Sect. 3.4.1. SExtractor makes a cross-correlation with this list and outputs the catalogue of the requested targets. With this method SExtractor detects 37 blobs ($\sim$ 39% agreement), which implies more blobs than running SExtractor on each image independently. A circular aperture (best for faint objects) of radius 7 pixels was used for the photometry. It is equivalent to 1.75 arcsec. We decided not to include in Table 3.4 these results from SExtractor because the estimated uncertainty of the photometry is too large, due to the fact that SExtractor expects the input image to be in counts. It was not possible to give the images in counts to SExtractor because the images were flux calibrated before combining them into the MB and BB mosaics.

Another method was using a custom-made Python routine for aperture photometry. For every object identified in Sect. 3.4.1, I integrate the flux of all pixels inside a circle of radius 7 pixels (1.75 arcsec). We also used the package Photutils (Bradley et al. 2017) of Astropy, designed for aperture photometry. The Photutils package includes the fraction of the pixel that is within the circular aperture, so it gathers more surface and samples the circular aperture better than my custom-made Python routine. The difference in magnitude between the two procedures is very small (below 0.05 mag) as the main difference between them is the treatment of the pixels in the border of the aperture, which are mainly sky signals and do not contribute significantly to the total flux. The main source of noise in our images is the photon noise of the sky. In previous sections we explained how we measure the magnitude limit of the images, set by the noise of the sky. Now I consider this as the main source of error in our photometry.

We derive the errorbar of the integrated flux of the objects (σ_S) from the standard deviation of the sky measured in boxes of side of 3.5 arcsec (equal to the diameter of the photometry aperture). It is calculated from the noise of the mean flux in the aperture (σ_A) as

$$\sigma_S = \sigma_A \times \Delta x^2 \times N_A, \tag{3.12}$$

where Δx is the scale plate of the instrument, 0.25 arcsec pixel^{-1} and N_A the number of pixels in the aperture. The units of (σ_S) are erg s^{-1} cm^{-2} Å^{-1}. Equation (3.12) is derived in Appendix 3.8.2 (Eq. [3.41]).

In order to be sure that there is indeed line emission in the visually selected blobs (Sect. 3.4.1), I have compared the integrated flux in the aperture of each object with the corresponding expected noise. I decided to set a detection threshold at $1.5\,\sigma_S$ based on a visual inspection of the blobs. Those blobs

detected in Sect. 3.4.1 with signal below this noise threshold were flagged in Table 3.4 as not having enough signal for its noise.

I am also interested in the size of the blobs. For that I used the second moment of the image around the blob, which gives us the size without assuming any particular shape for the blob. The equations used here are taken from the SExtractor manual (Bertin & Arnouts 1996). The equations for the barycenter are the following:

$$\overline{x} = \frac{\sum_i I_i x_i}{\sum_i I_i}, \qquad \overline{y} = \frac{\sum_i I_i y_i}{\sum_i I_i}, \tag{3.13}$$

where $\overline{x}$ and $\overline{y}$ are the barycenter along the x axis and y axis respectively. The sum extends to every pixel inside the aperture (3.5×3.5 arcsec^2), I_i is the flux in the pixel of spatial coordinates x_i, y_i. In our case, they are the offset in arcsec from the aperture center. The equations for the second moments of the image ($\overline{x^2}$, $\overline{y^2}$ and $\overline{xy}$) are the following:

$$\overline{x^2} = \frac{\sum_i I_i x_i^2}{\sum_i I_i} - \overline{x}^2, \quad \overline{y^2} = \frac{\sum_i I_i y_i^2}{\sum_i I_i} - \overline{y}^2, \quad \overline{xy} = \frac{\sum_i I_i x_i y_i}{\sum_i I_i} - \overline{x}\,\overline{y}. \tag{3.14}$$

As a first order approximation one can associate an elliptical shape to these moments. The three second order moments can be re-written in terms of the parameters of an ellipse that has them, namely, the semi-major (A) and semi-minor (B) axes,

$$A^2 = \frac{\overline{x^2} + \overline{y^2}}{2} + \sqrt{\left(\frac{\overline{x^2} - \overline{y^2}}{2}\right)^2 + \overline{xy}^2}, \tag{3.15}$$

$$B^2 = \frac{\overline{x^2} + \overline{y^2}}{2} - \sqrt{\left(\frac{\overline{x^2} - \overline{y^2}}{2}\right)^2 + \overline{xy}^2}, \tag{3.16}$$

and the orientation,

$$\tan 2\theta_0 = 2\,\frac{\overline{xy}}{\overline{x^2} - \overline{y^2}}, \tag{3.17}$$

where θ_0 is the angle of the ellipse in the x-y reference system. Fig. 3.10 shows examples of some identified blobs, each one has an ellipse drawn with the parameters A, B and θ_0 described in Eqs. (3.15), (3.16) and (3.17).

Table 3.4 contains the sizes of all the blobs, where we use as size the FWHM (full width at half maximum) associated to the semi-major axis A if the emission blob had a gaussian shape, i.e., FWHM$= 2\sqrt{2\ln 2}\,A$. In order to understand the

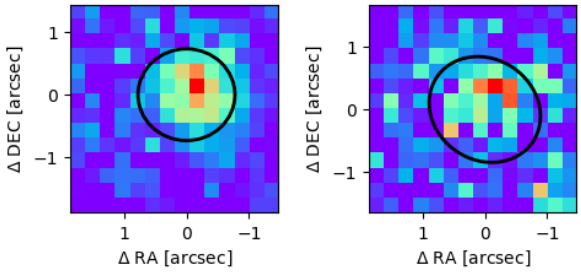

(a) blob #7

(b) blob #9

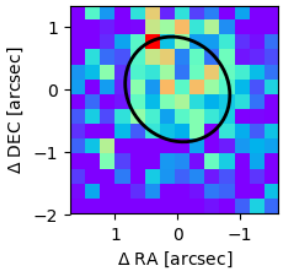

(c) blob #12

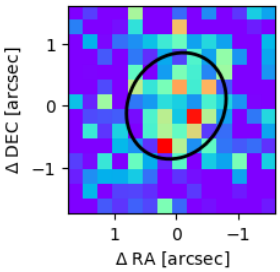

(d) blob #14

Figure 3.10: Images in Hα of the first four blobs of the list (#7, #9, #12, #14). The units of the horizontal and vertical axes are arcsec from the measured barycenter. The black ellipse is drawn with the parameters A, B and θ_0 described in Eqs. (3.15), (3.16) and (3.17). The FOV of these images is 3.5×3.5 arcsec^2. This is the FOV used to calculate the size of the blobs, and it matches the diameter of the photometry apertures.

uncertainty in the size due to the use of a finite aperture, I made the simulation described in Appendix 3.8.4. The conclusion is that sizes are overestimated by a factor around 1.6, so I use that as the uncertainty of the parameter given in Table 3.4.

As it can be seen in Table 3.4, most of the blobs have a FWHM around 0.7 kpc (2.33 arcsec), and the first ones in the table are smaller than the rest. This can be attributed to the effect modelled in Appendix 3.8.4, that the size of the blob is overestimated at low S/N. Due to the selection process, most of the objects with good S/N have a higher position in the table (a low identification number), so they tend to have smaller size due to their good signal to noise. But it could also happen that they are intrinsically smaller. The majority of the blobs in the list has roughly the same size which is due to the same effect;

the size in all of them is probably overestimated.

This paragraph describes Table 3.4 in detail. Table 3.4 lists the photometric properties of the detected blobs. It contains 96 blobs, identified with the procedure described in Sect. 3.4.1. The ID listed in the table corresponds to the position in the list of the first 200 objects, ordered by size, that were drawn from the catalogue made by SExtractor based on the $m_{\mathrm{MB}} - m_{\mathrm{BB}}$ image. The second column gives the Hα flux in units of erg s^{-1} cm^{-2}. The flux was calculated placing circular apertures of radius 7 pixels on the Hα image, as explained in the beginning of this section. The third column is the MB flux and the fourth the BB flux, both in units of erg s^{-1} cm^{-2} Å^{-1}. The flux was calculated placing circular apertures of radius 7 pixels on the MB and BB image. The uncertainty in the Hα, MB and BB flux is derived using Eq. (3.12). It is derived from the standard deviation of the sky measured in boxes of side 3.5 arcsec. It is a constant for every image (Hα, MB and BB). The fifth column gives the size of the blob in kpc, assumed to correspond to Hα and measured on the Hα image. The size is given in terms of the FWHM associated to the semi-major axis A (Eq. 3.15). The sixth column gives True or False whether Hα flux fulfils the detection threshold of being larger than 1.5 times the noise. The seventh column gives the logarithm of the gas mass of the blob. The calculation of the gas mass will be explained in Sect. 3.5.2. It assumes that the emission we detect is Hα at the redshift of the target galaxy, at a temperature of 10^4 K and an electron density 0.01 cm^{-3}. The uncertainty in the gas mass comes from the propagation of the uncertainty of the Hα flux. The last column gives the distance in kpc between the blob and the target galaxy UM260. It assumes the blobs to be at the redshift of the target galaxy in order to convert from arcsec to kpc.

3.5 Properties of UM260 and the emission around it

3.5.1 Observations on this galaxy existing in the literature

Sánchez Almeida et al. (2016) search for XMP galaxies in SDSS using the ratio of the lines [OIII]λ4363 to [OIII]λ5007, which is a proxy for the electron temperature. As the gas in XMP galaxies has very little metals, it can not cool efficiently, so it has relatively high electron temperature. UM260 is one of the objects that they select. They report an oxygen abundance $(12 + \log[\mathrm{O/H}])$ of 7.68 ± 0.12, a ratio of abundances of nitrogen over oxygen $(\log[\mathrm{N/O}])$ of -1.52 ± 0.13, an ionization parameter $(\log U)$ of -1.89 ± 0.27, and a extinction coefficient in Hβ ($C_{\mathrm{H}\beta}$) of 0.00 ± 0.03.

Chang et al. (2015) use SDSS and WISE (bands at 3.4, 4.6, 12 and 22 μm)

data to reconstruct spectral energy distributions (SED) of galaxies. The addition of WISE photometry together with the optical data means that not only the stellar emission is modelled in the SED, but also dust extinction and emission. They obtain for UM260 a star formation rate ($\log \mathrm{SFR}$) of $-1.583^{+0.125}_{-0.055}$, an stellar mass ($\log \mathrm{M_*}$) of $7.40^{+0.09}_{-0.06}$ and a specific star formation rate ($\log \mathrm{sSFR} = \log [\mathrm{SFR/M_*}]$) of $-8.98^{+0.16}_{-0.14}$. SFR, $\mathrm{M_*}$ and sSFR are expressed in units of $\mathrm{M_\odot\ yr^{-1}}$, $\mathrm{M_\odot}$, $\mathrm{yr^{-1}}$, respectively. According to Chang et al. (2015), these results have to be taken with care because this galaxy does not have reliable aperture corrections, although they state that the uncertainty in the aperture corrections is smaller than the uncertainties derived in the stellar mass and SFR. The magnitudes used by Chang et al. (2015) are given in Table 3.3.

Table 3.3: Magnitudes of UM260.

SDSS u [Jy][a]	$7.9 \pm 0.5 \times 10^{-5}$
SDSS g [Jy][a]	$1.41 \pm 0.07 \times 10^{-4}$
SDSS r [Jy][a]	$1.63 \pm 0.08 \times 10^{-4}$
SDSS i [Jy][a]	$1.73 \pm 0.09 \times 10^{-4}$
SDSS z [Jy][a]	$1.85 \pm 0.09 \times 10^{-4}$
W1 [Jy][a]	$6.8 \pm 1.1 \times 10^{-5}$
W2 [Jy][a]	$4.7 \pm 1.4 \times 10^{-5}$
W3 [Jy][a]	$0.004 \pm 2.0 \times 10^{-4}$ upperlimit
W4 [Jy][a]	$0.004 \pm 1.8 \times 10^{-3}$ upperlimit

[a] From Chang et al. (2015) in the VizieR catalog

Eckert et al. (2015) also obtain the stellar mass of the galaxy from SED modelling, but they also include UV and the HI 21 cm. A stellar mass ($\log \mathrm{M_*/M_\odot}$) of 7.57 was obtained, consistent with the estimate by Chang et al. (2015).

From the survey ALFALFA (Giovanelli et al. 2005), Stark et al. (2016) give a total flux in 21 cm line of 0.53 ± 0.16 Jy km $\mathrm{s^{-1}}$. Eq. (2) in Stark et al. (2016) gives us a hydrogen atomic mass ($\mathrm{M_{HI}}$) of $(4.8 \pm 1.5) \times 10^8\ \mathrm{M_\odot}$, or $\log (\mathrm{M_{HI}/M_\odot}) = 8.68 \pm 0.13$. Thus, combining the stellar mass from Chang et al. (2015) with this estimate, one gets a gas to stars mass ratio $\mathrm{M_{HI}/M_*} \simeq 20$. Thus, UM260 is an extremely gas rich object, in line with the rest of the XMPs (Filho et al. 2013).

Sánchez Almeida et al. (2010) classified the spectra of the galaxies available in SDSS DR7 using the machine learning algorithm *k-means* (ASK classification). This unsupervised algorithm classifies the spectra according to their shape in the visible wavelength range. The target galaxy UM260 belongs to

class 25 with a quality of 0.344, and to class 26 with a quality of 0.04895[10]. The quality is a merit function that evaluates the distance to the class center, where the largest quality corresponds to the minimum distance.

According to Table 1 of Sánchez Almeida et al. (2012), class 25 contains star-forming galaxies with a metal-poor starburst and a young stellar population. The spectrum is dominated by strong emission lines, with a blue continuum and weak absorption lines in the Balmer series. It also has the Balmer continuum in emission. Comparing to other classes in the ASK classification, it is among those with the youngest stellar population and the lowest gas-phase metallicity. The properties of class 25 are: the oxygen abundance of the gas, $12+\log(\mathrm{O/H})$, is 8.29 ± 0.01, the age of the stellar population is 0.0083 ± 0.0018 Gyr, and the metallicity of the stars, $\mathrm{Z/Z_\odot}$, is 0.72 ± 0.36. These results were obtained from the average spectra of the class. The galaxies of class 26 are similar to those of class 25, but with slightly older stellar populations and slightly higher gas-phase metallicity.

It stands out that the metallicity of class 25 ($12 + \log[\mathrm{O/H}] = 8.29 \pm 0.01$) does not match the metallicity of the galaxy ($12 + \log[\mathrm{O/H}] = 7.68 \pm 0.12$) measured by Sánchez Almeida et al. (2016). Both calculations are based on SDSS spectra, but one is the average of all spectra in class 25 and the other is the spectrum of UM260. The SDSS spectrum of UM260 is shown in Fig. 3.11. The methods used to calculate the metallicity are also different; whereas Sánchez Almeida et al. (2012) use the direct method, Sánchez Almeida et al. (2016) use the code HII-CHI-mistry (Pérez-Montero 2014), which is consistent with the direct method but it is not the direct method. Alternatively, there is a large spread in metallicity within the class that is not reflected in the uncertainty of the metallicity given by Sánchez Almeida et al. (2012). Actually, the algorithm classifies the spectra according to the shape of the spectrum, so the continuum has more weight than the emission lines. This can be explained if the target galaxy UM260 has a continuum representative of class 25 and the emission lines come from an HII region which is more metal poor than the rest of the galaxy. This behaviour is typical of the XMP galaxies as described by Sánchez Almeida et al. (2013, 2015). So, the metallicity of UM260 is low compared with the average spectrum of class 25. In other words, UM260 is an outlier in the gas metallicity of class 25, but is not in the age of the stellar population and the metallicity of the stars (this behavior is discussed in detail in Chapter 4).

As part of the GALEX Medium-depth Imaging Survey, Bianchi et al. (2011) give the following magnitudes: $\mathrm{FUV} = 20.27 \pm 0.06$ and $\mathrm{NUV} = 20.15 \pm 0.04$. The size (FWHM) of the source in the FUV and NUV is 5.37 arcsec, therefore,

[10] http://sdc.cab.inta-csic.es/ask/jsp/searchform.jsp

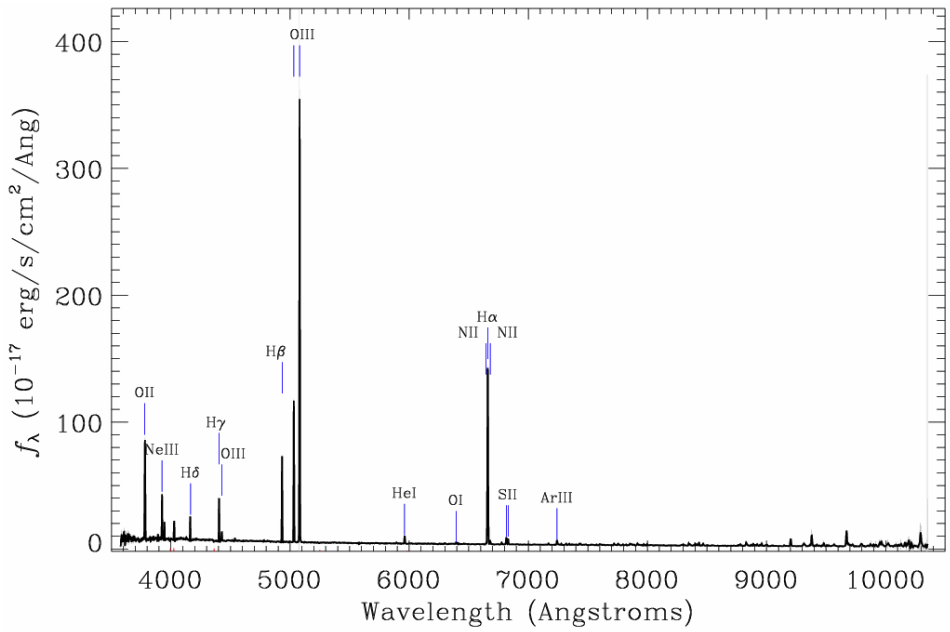

Figure 3.11: SDSS spectra of the galaxy UM260, showing the main emission lines.

significantly larger than the optical size (Table 3.2).

Fliri & Trujillo (2016) present a catalog of the properties measured in the images of the IAC Stripe 82 Legacy Project. They give the following Petrosian magnitudes for the target galaxy UM260: $u = 19.48 \pm 0.03$, $g = 18.491 \pm 0.006$, $r = 18.277 \pm 0.007$, $i = 18.201 \pm 0.008$, $z = 18.12 \pm 0.02$. The Petrosian radius is 4.6 arcsec. They provide a position angle of -16.87 degrees and an elongation (axial ratio) of 1.310, measured in their r-deep image (g+r+i). In comparison, we obtain a position angle -16.99 and an elongation of 1.27, measured in the BB image (SDSS r) with SExtractor, which agrees with Fliri & Trujillo (2016).

With the images of the IAC Stripe 82 Legacy Project, we made a color composition of UM260. It is shown in Fig. 3.1, with the galaxy at the center of the image. UM260 has two components; one blue star forming region slightly off-centered, and a diffuse white component corresponding to the rest of the galaxy. Surrounding the galaxy, there are little cloud-like objects. Those are the ones that originally captured our interest and in the end were responsible for choosing UM260 in our proof-of-concept observation.

3.5.2 Properties of the emission line blobs

As described in Section 3.4.1, I have detected a total of 96 emission line blobs around UM260. Table 3.4 summarizes their main properties. These properties are discussed in detail in this subsection.

BB, MB, Hα measured flux. The flux in the three images, BB, MB and Hα, appear in Table 3.4. The uncertainty in the measured flux is a constant for each one of these three images. It depends only of the standard deviation of the sky of the image and the number of pixels in the photometry aperture. Most of the 96 blobs (88%) are below the flux threshold in BB (see also Fig. 3.12), so we can not claim the detection of the continuum. In the case of the MB image, as you can see in Fig. 3.13, more blobs are detected above the flux threshold in MB (49%), but still the mode of the distribution is below the threshold. The best case is for the Hα image (Fig. 3.14), where the mode of the histogram is at the flux threshold, and 66% (63) of the blobs are above it.

There are some blobs with near zero flux or negative flux in the MB or Hα images. These blobs have a clear detection on the $m_{\rm MB} - m_{\rm BB}$ color image, however, their signal is usually at the level of the noise, so the integrated flux turns out very small. Sometimes it is because the blob is very faint and others because the region around them is particularly noisy.

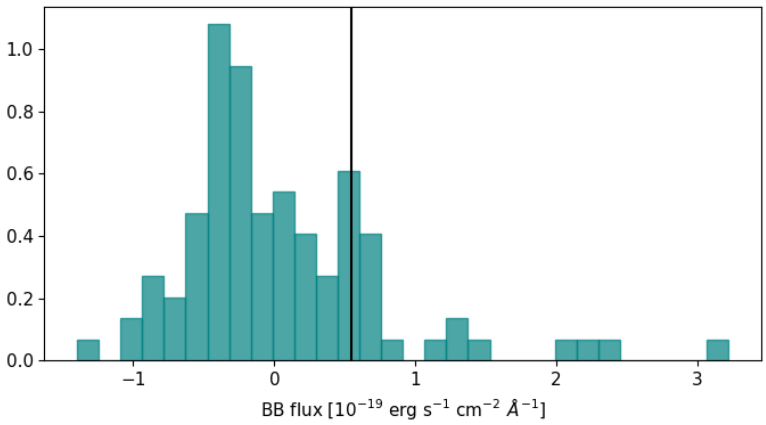

Figure 3.12: Histogram of the flux of the emission line blobs measured in the BB image. The vertical black line is the BB flux threshold, defined as 1.5 times the uncertainty of the measured flux. 88% of the blobs do not have BB signal above the noise level.

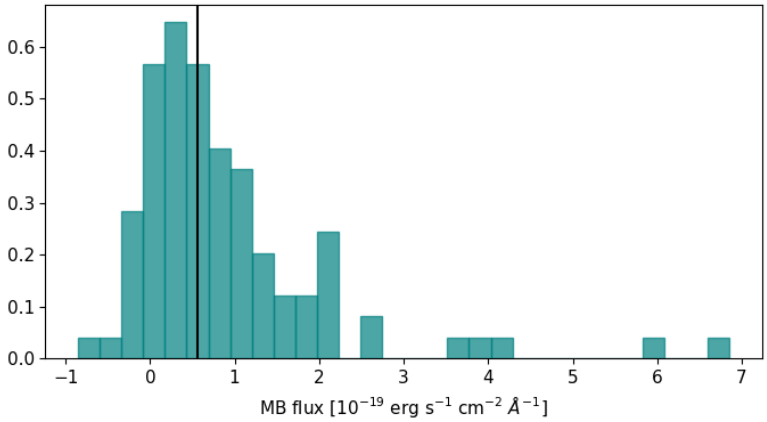

Figure 3.13: Histogram of the flux measured in the MB image. The vertical black line is the MB flux threshold, defined as 1.5 times the uncertainty of the measured flux.

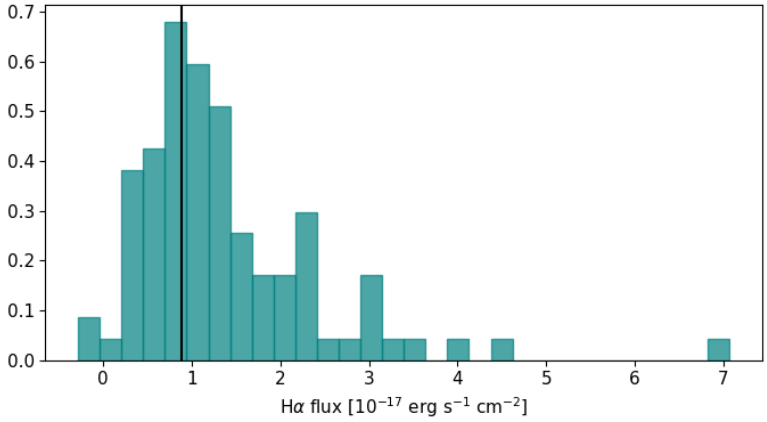

Figure 3.14: Histogram of the flux measured in the Hα image. The vertical black line is the Hα flux threshold, defined as 1.5 times the uncertainty of the measured flux.

Size. The size of the blobs is given in Table 3.4 in kpc, thus assuming that the emission occurs at the distance of UM260. As we explained in Sect. 3.4.3 and Appendix 3.8.4, the values in the table represent upperlimits because, due to the low S/N, the size is overestimated by a factor around 1.6. For the same reason, we trust the size of the smallest and brightest blobs, since they also have the highest S/N. The histogram of the sizes is shown in Fig. 3.15.

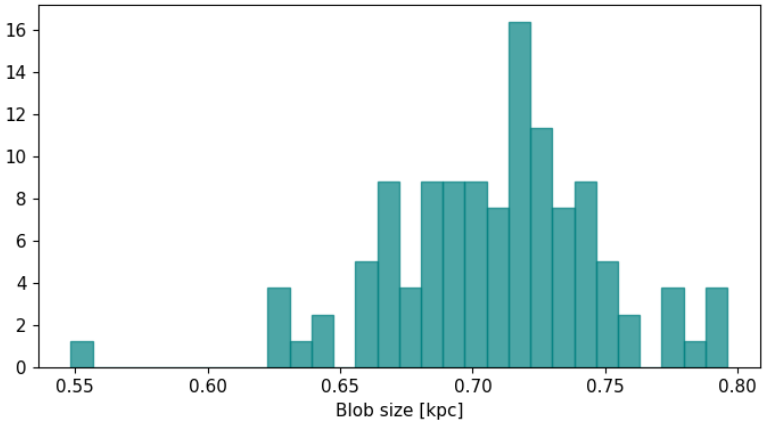

Figure 3.15: Histogram of the size of the blobs in the Hα image, assuming they are at the distance of UM260.

Gas mass. In order to estimate the gas mass of these blobs, we also assume that they are at the redshift of the target galaxy UM 260, so the emission that we detect in the MB filter is Hα and is produced by the recombination of H. We follow the procedure in Sect. 2.3.3 and use Eq. (2.12). If we assume typical values of HII regions for the temperature (T= 10^4 K) and electron density (n_e = 10 cm^{-3}), we get masses within the range M$_g$ $\sim$ $10^3 - 10^4$ M$_\odot$. If we consider that they have the typical density of the circumgalactic medium (CGM: $n_e \sim 0.01$ cm^{-3}), we get masses within the range M$_g$ $\sim$ $10^6 - 10^7$ M$_\odot$. The gas mass of the individual Hα blobs for n_e = 0.01 cm^{-3} is included in Table 3.4.

The value I use for n_e is obtained from both observations and simulations. From the simulations presented in van de Voort & Schaye (2012, Fig. 9), we got a value for the gas density which is of the order of 10^5 the mean baryon density of the universe. (I cite the density of the cold gas at 0.1 virial radii of galaxies with halo masses between $10^{11.5}$ and $10^{12.5}$ M$_\odot$.) Using the mean density of the universe at redshift zero, and assuming the gas to be made of H and He, then the mean density of H in the local Universe is 2.5×10^{-7}cm^{-3}. Assuming an HII region with $n_{\rm H} \simeq n_e$, then one gets $n_e \simeq 0.025$ cm^{-3}. As far as the observations are concerned, Stern et al. (2016) find a CGM gas density in the range between 50 and 5×10^5 times the mean density. This large range in gas density comes from the assumption that the cool CGM has a structure in which small high-density clouds are embedded in large low-density clouds. The observations presented in the paper corresponds to redshift 0.2, but they will

not be very different from the conditions in the local universe since densities scales as $(1+z)^3$ which corresponds to 1.7 at z = 0.2 (see Eq. [3.1]). They give a mean $n_{\rm H}$ of 3.2×10^{-7} cm^{-3} which, at the high end of the density distribution gives $n_e \sim 0.16$ cm^{-3}. With this value and the one from van de Voort & Schaye (2012), we can set a lower limit on the electron density $n_e < 0.1$ cm^{-3}. This justifies the value used to calculate the mass in Table 3.4, i.e., $n_e = 0.01$ cm^{-3}.

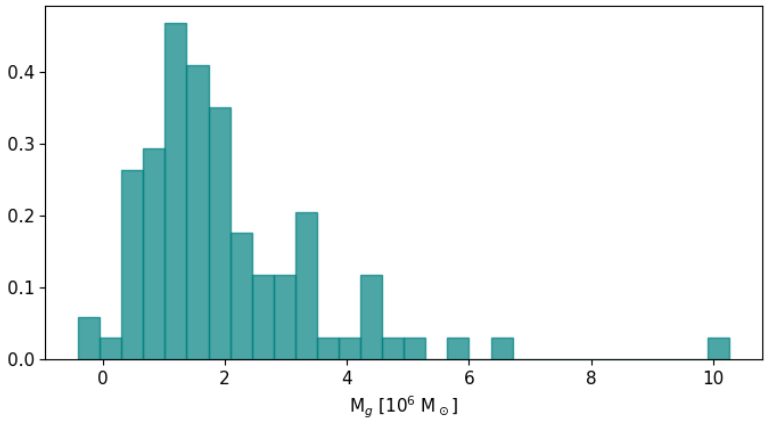

Figure 3.16: Histogram of gas mass emitting in Hα for $n_e = 0.01$ cm^{-3}.

A histogram of the gas mass of the Hα blobs is represented in Fig. 3.16. There are some quite massive blobs, but most of them are around 10^6 $M_\odot$. This is one order of magnitude less than the stellar mass of the galaxy and two orders of magnitude less than the gas mass of the galaxy as inferred from HI (see Sect. 3.5.1). Fig. 3.17 shows the gas mass against the distance in kpc to the target galaxy UM260, assuming the Hα blobs to be at the distance of the galaxy. Although there is a large spread in mass due to the poor S/N of most of the objects, there is no evident correlation between the gas mass and the distance to the target galaxy.

Distance of the Hα blobs to UM260. We calculated the projected distance of each blob to the central galaxy. The histogram of distances is shown in Fig. 3.18. There is a large spread in the distance of the blobs to the target galaxy. There seems to be a concentration around ~ 50 and ~ 70 kpc. There is no evident pattern in the distribution. The virial radius divides the CGM from the IGM (intergalactic medium). According to Kravtsov (2013), the virial radius of a galaxy is related to the effective radius with the following relation: $R_{\rm vir} \simeq 70\ R_e$. For galaxy UM260, $R_e \sim 2''$, so $R_{\rm vir} \sim 140''$ or 42

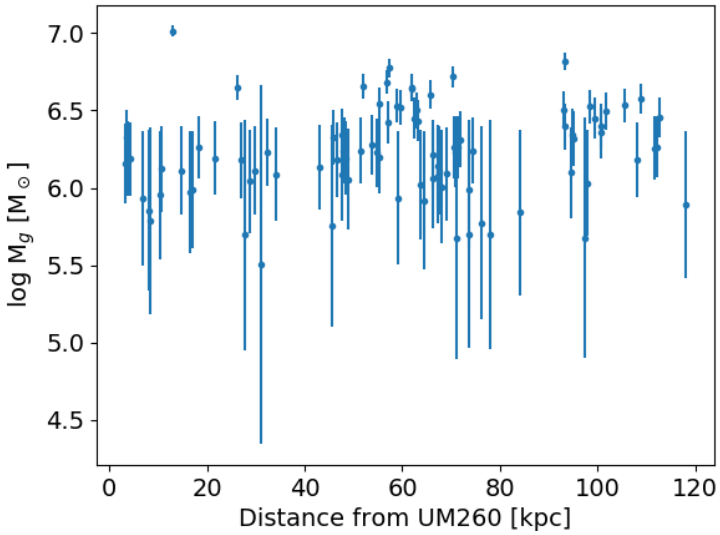

Figure 3.17: Measured gas mass of the Hα blobs versus the distance in kpc to the target galaxy UM260. There is no evident correlation between M_g and the distance to the target galaxy.

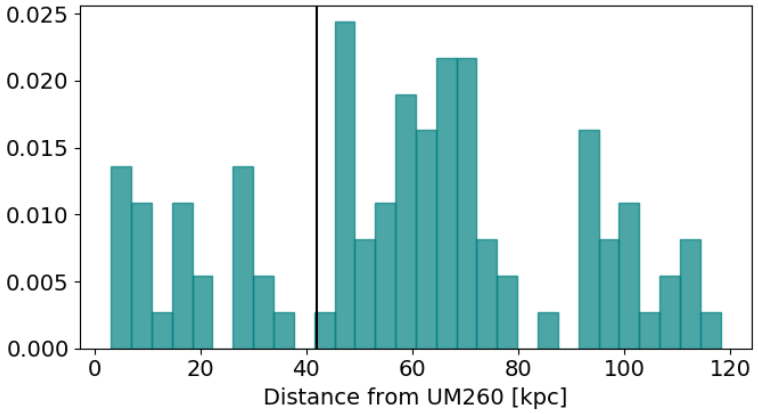

Figure 3.18: Histogram of the distance between the Hα blobs and UM260. The vertical line is the estimated virial radius of UM260.

kpc. Therefore some of the Hα blobs seem to be within the virial radius, but most of them are not. Keep in mind, however, that the R_e in XMPs is often

underestimated. A bright star forming region dominates the light of the galaxy and thus the inferred R_e is not representing the whole galaxy but the knot (see, e.g., Sánchez Almeida et al. 2017). Should this be the case, most blobs would be within the virial radius of UM260.

The question arises as to whether we are detecting all the blobs or due to proper motions, some are shifted in wavelength so much as to exceed the band-pass of the MB filter. This does not seem to be an issue since the band-pass of the MB filter is equivalent to ∼7000 km s^{-1}. This is more than enough since the expected proper motions are just tens of km s^{-1}.

Preferred azimuth of the Hα blobs. We calculated the azimuth of the blobs in a reference system centered in UM260. As the target galaxy is not in the center of the image, some directions have more pixels than others. In order to compare the number of blobs existing in each direction, I normalise the histogram of the azimuth of the blobs dividing by the histogram of the azimuth of all the pixels in the image. Fig. 3.19a shows the histogram of the azimuth of the blobs prior to this normalisation, and 3.19b the histogram of the azimuth of all pixels in the image. It is a polar diagram where the length

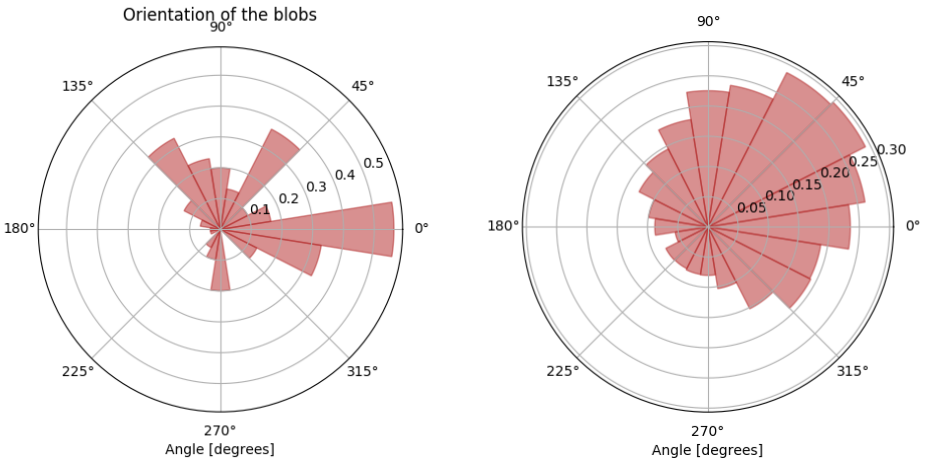

(a) blobs (b) all pixels

Figure 3.19: (a) Polar histogram of the azimuth of the blobs. Angles are measured in a reference system centered in UM260, where RA corresponds to abscissae and azimuth zero points to the East. (b) Polar histogram of the azimuth of all the pixels in the image. It clearly differs from (a).

in each azimuth is proportional to the number of pixels with this azimuth. Azimuths are computed in a reference system centered in the galaxy with the azimuth equals zero along the celestial East. The histograms in Fig. 3.19a and 3.19b are very different so the existence of preferred directions in the Hα blobs (Fig. 3.19a) is not due to uneven sampling of the different azimuths. Instead, the existence of the peaks indicates that there is a preference for the blobs to be along certain directions.

Figure 3.20 contains the histograms normalized to histogram in Fig. 3.19b. Figure 3.20a contains the 96 blobs described in Sect. 3.4.1 whereas Fig. 3.20b shows only those above the flux threshold in Hα. The relative importance of the peaks of the histogram changes with respect to those in Fig. 3.19a, but the existence of 3 preferred directions remains. There are three major peaks, although the one pointing to the south (270°) is not reliable, because some of the blobs in this peak are in a very noisy region near the border of the image. The two other filaments seem to be roughly aligned with the mayor axis of the galaxy. This is to be expected if the gas in the blobs were co-planar with the disk of the galaxy.

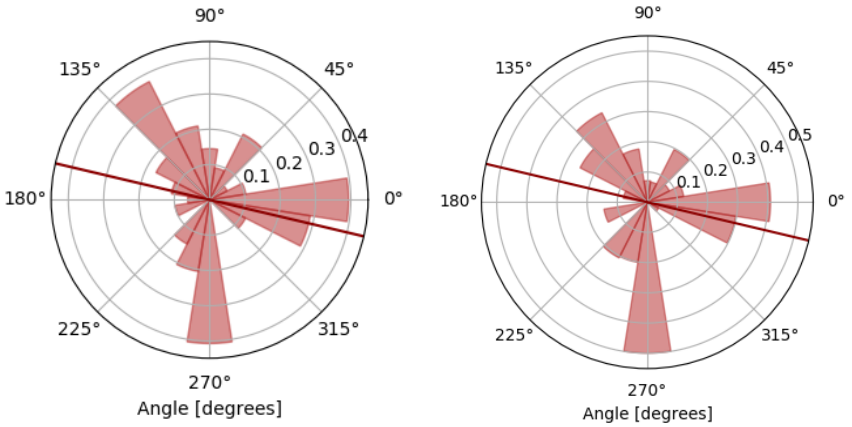

(a) all blobs (b) Hα detected blobs

Figure 3.20: (a) Polar histogram of the orientation of the blobs, normalised to the of the sky area sampled in each direction (i.e., histogram in Fig. 3.19a divided by the histogram in Fig. 3.19b). (b) The same as in (a) but only for the blobs detected in Hα above the flux threshold. It can be seen that the distribution of azimuth has 3 prominent preferred directions. The red solid line represents the angle of the major axis of UM260 in this reference system.

Table 3.4: Physical parameters of the observed Hα blobs.

ID	Hα flux $\times 10^{17}$ [erg s^{-1}cm^{-2}]	MB flux $\times 10^{20}$ [erg s^{-1}cm^{-2}Å^{-1}]	BB flux $\times 10^{20}$ [erg s^{-1}cm^{-2}Å^{-1}]	Hα size[a] [kpc]	Enough S/N in Hα?[b]	log M_g^c [$M_\odot$]	Separation[d] [kpc]
7	7.1 ± 0.59	69 ± 3.8	24 ± 3.7	0.55	True	7.01 ± 0.04	12.9
9	3.1 ± 0.59	25 ± 3.8	5.8 ± 3.7	0.66	True	6.65 ± 0.08	62.0
12	4.1 ± 0.59	39 ± 3.8	13 ± 3.7	0.63	True	6.77 ± 0.06	57.3
14	2.8 ± 0.59	22 ± 3.8	4.7 ± 3.7	0.63	True	6.60 ± 0.09	65.7
15	0.93 ± 0.59	5.3 ± 3.8	−0.47 ± 3.7	0.67	True	6.13 ± 0.27	42.9
16	2.3 ± 0.59	15 ± 3.8	0.6 ± 3.7	0.64	True	6.53 ± 0.11	98.3
19	3.1 ± 0.59	26 ± 3.8	6.8 ± 3.7	0.63	True	6.65 ± 0.08	26.1
20	3.3 ± 0.59	16 ± 3.8	−4.8 ± 3.7	0.71	True	6.68 ± 0.08	56.9
28	1.2 ± 0.59	3.3 ± 3.8	−4.4 ± 3.7	0.67	True	6.25 ± 0.21	71.1
33	1.9 ± 0.59	18 ± 3.8	6.1 ± 3.7	0.67	True	6.43 ± 0.14	63.2
35	1.1 ± 0.59	3.7 ± 3.8	−3 ± 3.7	0.72	True	6.19 ± 0.24	21.5
37	1.3 ± 0.59	4.1 ± 3.8	−3.7 ± 3.7	0.68	True	6.26 ± 0.20	71.4
38	1.2 ± 0.59	6.8 ± 3.8	−0.69 ± 3.7	0.69	True	6.24 ± 0.21	47.8
40	2.4 ± 0.59	12 ± 3.8	−2.4 ± 3.7	0.75	True	6.54 ± 0.11	105.4
41	2.6 ± 0.59	20 ± 3.8	4.1 ± 3.7	0.72	True	6.58 ± 0.10	108.8
42	2.3 ± 0.59	12 ± 3.8	−2.4 ± 3.7	0.72	True	6.53 ± 0.11	58.7
44	1.1 ± 0.59	1.7 ± 3.8	−5.1 ± 3.7	0.74	True	6.20 ± 0.23	55.4
45	2.4 ± 0.59	5 ± 3.8	−10 ± 3.7	0.72	True	6.54 ± 0.11	55.3
49	0.89 ± 0.59	1.5 ± 3.8	−4.1 ± 3.7	0.67	True	6.11 ± 0.29	67.4
50	0.99 ± 0.59	6.2 ± 3.8	−0.056 ± 3.7	0.69	True	6.16 ± 0.26	3.1
52	1 ± 0.59	9.1 ± 3.8	2.6 ± 3.7	0.69	True	6.18 ± 0.24	26.8
53	2.2 ± 0.59	35 ± 3.8	22 ± 3.7	0.72	True	6.51 ± 0.12	93.1
56	0.62 ± 0.59	5 ± 3.8	1.2 ± 3.7	0.64	False	5.95 ± 0.41	10.3
60	1.7 ± 0.59	2.9 ± 3.8	−7.8 ± 3.7	0.71	True	6.40 ± 0.15	93.3
62	2 ± 0.59	12 ± 3.8	−0.41 ± 3.7	0.68	True	6.46 ± 0.13	112.8
63	0.86 ± 0.59	0.87 ± 3.8	−4.5 ± 3.7	0.69	False	6.10 ± 0.30	94.6
65	1.6 ± 0.59	5.4 ± 3.8	−4.3 ± 3.7	0.72	True	6.36 ± 0.16	100.6
66	0.35 ± 0.59	0.034 ± 3.8	−2.1 ± 3.7	0.67	False	5.70 ± 0.73	73.7

Continued on next page

Table 3.4 – *Continued from previous page*

ID	Hα flux $\times 10^{17}$ [erg s^{-1}cm^{-2}]	MB flux $\times 10^{20}$ [erg s^{-1}cm^{-2}Å^{-1}]	BB flux $\times 10^{20}$ [erg s^{-1}cm^{-2}Å^{-1}]	Hα size[a] [kpc]	Enough S/N in Hα?[b]	log M_g^c [$M_\odot$]	Separation[d] [kpc]
68	4.6 ± 0.59	61 ± 3.8	32 ± 3.7	0.75	True	6.82 ± 0.06	93.3
71	3 ± 0.59	22 ± 3.8	2.8 ± 3.7	0.71	True	6.64 ± 0.08	61.8
72	3.1 ± 0.59	41 ± 3.8	21 ± 3.7	0.79	True	6.66 ± 0.08	52.0
76	1.5 ± 0.59	12 ± 3.8	3 ± 3.7	0.74	True	6.34 ± 0.17	94.9
77	1.1 ± 0.59	4.5 ± 3.8	−2.1 ± 3.7	0.73	True	6.19 ± 0.24	4.3
80	1.8 ± 0.59	7.6 ± 3.8	−3.8 ± 3.7	0.69	True	6.42 ± 0.14	57.1
83	0.59 ± 0.59	9.2 ± 3.8	5.5 ± 3.7	0.69	False	5.93 ± 0.43	6.9
84	2.3 ± 0.59	16 ± 3.8	1.9 ± 3.7	0.71	True	6.52 ± 0.11	59.7
88	3.6 ± 0.59	8.5 ± 3.8	−14 ± 3.7	0.72	True	6.72 ± 0.07	70.2
89	1.1 ± 0.59	3.6 ± 3.8	−3 ± 3.7	0.71	True	6.19 ± 0.24	3.7
91	1.2 ± 0.59	4 ± 3.8	−3.5 ± 3.7	0.73	True	6.24 ± 0.21	74.4
92	1.1 ± 0.59	−2.2 ± 3.8	−8.9 ± 3.7	0.7	True	6.19 ± 0.24	48.3
93	2.2 ± 0.59	10 ± 3.8	−3.6 ± 3.7	0.72	True	6.50 ± 0.12	63.1
94	1.9 ± 0.59	9.8 ± 3.8	−2.3 ± 3.7	0.73	True	6.45 ± 0.13	62.5
95	0.84 ± 0.59	8.3 ± 3.8	3 ± 3.7	0.7	False	6.09 ± 0.30	34.2
96	1.3 ± 0.59	8.5 ± 3.8	0.53 ± 3.7	0.7	True	6.27 ± 0.20	112.2
97	1.2 ± 0.59	0.43 ± 3.8	−7.3 ± 3.7	0.79	True	6.26 ± 0.21	111.6
98	1.1 ± 0.59	2.7 ± 3.8	−3.9 ± 3.7	0.74	True	6.18 ± 0.24	46.6
99	0.42 ± 0.59	−0.62 ± 3.8	−3.3 ± 3.7	0.72	False	5.79 ± 0.60	8.2
100	1.3 ± 0.59	5.4 ± 3.8	−2.5 ± 3.7	0.66	True	6.26 ± 0.20	18.3
104	0.67 ± 0.59	0.04 ± 3.8	−4.2 ± 3.7	0.74	False	5.99 ± 0.38	73.6
105	1.5 ± 0.59	14 ± 3.8	4.5 ± 3.7	0.78	True	6.32 ± 0.18	45.9
106	0.32 ± 0.59	3.3 ± 3.8	1.3 ± 3.7	0.67	False	5.67 ± 0.78	71.2
108	−0.065 ± 0.59	−8.5 ± 3.8	−8.1 ± 3.7	0.73	False	nan ± −3.91	52.5
110	1.2 ± 0.59	0.99 ± 3.8	−6.3 ± 3.7	0.69	True	6.23 ± 0.22	32.4
116	0.85 ± 0.59	7.7 ± 3.8	2.4 ± 3.7	0.7	False	6.09 ± 0.30	69.1
119	1 ± 0.59	21 ± 3.8	14 ± 3.7	0.66	True	6.18 ± 0.24	108.1
120	0.89 ± 0.59	4.4 ± 3.8	−1.1 ± 3.7	0.69	True	6.11 ± 0.29	14.6
121	1.9 ± 0.59	18 ± 3.8	5.8 ± 3.7	0.74	True	6.45 ± 0.13	99.5
122	1.5 ± 0.59	1.4 ± 3.8	−8 ± 3.7	0.71	True	6.34 ± 0.17	47.6

Continued on next page

Table 3.4 – *Continued from previous page*

ID	Hα flux $\times 10^{17}$ [erg s^{-1}cm^{-2}]	MB flux $\times 10^{20}$ [erg s^{-1}cm^{-2}Å^{-1}]	BB flux $\times 10^{20}$ [erg s^{-1}cm^{-2}Å^{-1}]	Hα size[a] [kpc]	Enough S/N in Hα?[b]	log M_g^c [$M_\odot$]	Separation[d] [kpc]
124	0.76 ± 0.59	5 ± 3.8	0.28 ± 3.7	0.7	False	6.04 ± 0.34	28.8
126	0.39 ± 0.59	8.3 ± 3.8	5.8 ± 3.7	0.7	False	5.76 ± 0.65	45.5
128	1.2 ± 0.59	2 ± 3.8	−5.2 ± 3.7	0.75	True	6.23 ± 0.22	54.8
131	1.4 ± 0.59	6.2 ± 3.8	−2.8 ± 3.7	0.73	True	6.32 ± 0.18	95.1
132	0.95 ± 0.59	4.3 ± 3.8	−1.6 ± 3.7	0.66	True	6.14 ± 0.27	67.4
136	1.3 ± 0.59	−2 ± 3.8	−10 ± 3.7	0.67	True	6.28 ± 0.20	53.7
137	1.4 ± 0.59	2.6 ± 3.8	−6.2 ± 3.7	0.68	True	6.31 ± 0.18	71.8
138	−0.28 ± 0.59	−4.5 ± 3.8	−2.7 ± 3.7	0.73	False	nan ± −0.90	60.1
140	0.74 ± 0.59	14 ± 3.8	8.9 ± 3.7	0.73	False	6.03 ± 0.34	97.9
141	2.2 ± 0.59	20 ± 3.8	6.1 ± 3.7	0.69	True	6.49 ± 0.12	101.6
142	−0.012 ± 0.59	0.27 ± 3.8	0.34 ± 3.7	0.76	False	nan ± −21.20	19.0
145	1.2 ± 0.59	0.15 ± 3.8	−7.1 ± 3.7	0.74	True	6.23 ± 0.22	70.8
148	0.83 ± 0.59	3 ± 3.8	−2.1 ± 3.7	0.74	False	6.08 ± 0.31	67.2
151	0.79 ± 0.59	9.7 ± 3.8	4.8 ± 3.7	0.64	False	6.06 ± 0.32	66.2
154	0.65 ± 0.59	3.3 ± 3.8	−0.72 ± 3.7	0.69	False	5.97 ± 0.39	16.5
156	0.41 ± 0.59	2.6 ± 3.8	0.014 ± 3.7	0.7	False	5.77 ± 0.62	76.2
157	0.84 ± 0.59	12 ± 3.8	6.3 ± 3.7	0.73	False	6.09 ± 0.30	47.5
162	1.3 ± 0.59	6.2 ± 3.8	−1.7 ± 3.7	0.72	True	6.27 ± 0.20	70.5
163	0.89 ± 0.59	11 ± 3.8	5.6 ± 3.7	0.73	True	6.11 ± 0.29	29.7
164	0.7 ± 0.59	−2.2 ± 3.8	−6.6 ± 3.7	0.76	False	6.01 ± 0.36	68.0
166	1.2 ± 0.59	3.3 ± 3.8	−4.2 ± 3.7	0.8	True	6.24 ± 0.21	48.1
170	0.53 ± 0.59	8 ± 3.8	4.7 ± 3.7	0.78	False	5.89 ± 0.48	118.2
172	0.72 ± 0.59	0.88 ± 3.8	−3.6 ± 3.7	0.72	False	6.02 ± 0.35	63.6
173	0.67 ± 0.59	11 ± 3.8	6.4 ± 3.7	0.75	False	5.99 ± 0.38	17.1
174	0.78 ± 0.59	−0.94 ± 3.8	−5.8 ± 3.7	0.73	False	6.05 ± 0.33	48.9
175	0.49 ± 0.59	4.6 ± 3.8	1.5 ± 3.7	0.68	False	5.86 ± 0.52	8.2
177	0.48 ± 0.59	2.5 ± 3.8	−0.48 ± 3.7	0.72	False	5.84 ± 0.53	84.0
181	0.22 ± 0.59	7.2 ± 3.8	5.8 ± 3.7	0.68	False	5.50 ± 1.16	31.0
182	0.91 ± 0.59	1.2 ± 3.8	−4.5 ± 3.7	0.71	True	6.12 ± 0.28	10.5
183	0.34 ± 0.59	−0.056 ± 3.8	−2.2 ± 3.7	0.77	False	5.70 ± 0.74	77.9

Continued on next page

Table 3.4 – *Continued from previous page*

ID	Hα flux $\times 10^{17}$ [erg s^{-1}cm^{-2}]	MB flux $\times 10^{20}$ [erg s^{-1}cm^{-2}Å^{-1}]	BB flux $\times 10^{20}$ [erg s^{-1}cm^{-2}Å^{-1}]	Hα size[a] [kpc]	Enough S/N in Hα?[b]	log M_g^c [$M_\odot$]	Separation[d] [kpc]
189	0.59 ± 0.59	10 ± 3.8	6.5 ± 3.7	0.72	False	5.94 ± 0.43	59.1
191	1.2 ± 0.59	9.5 ± 3.8	2 ± 3.7	0.72	True	6.24 ± 0.21	51.4
386	0.34 ± 0.59	−1.1 ± 3.8	−3.3 ± 3.7	0.69	False	5.70 ± 0.75	27.7
530	0.33 ± 0.59	−2.4 ± 3.8	−4.4 ± 3.7	0.78	False	5.68 ± 0.78	97.4
596	1.1 ± 0.59	5.4 ± 3.8	−1.7 ± 3.7	0.75	True	6.22 ± 0.23	66.3
627	1.7 ± 0.59	22 ± 3.8	11 ± 3.7	0.74	True	6.40 ± 0.15	100.6
683	1.5 ± 0.59	22 ± 3.8	13 ± 3.7	0.67	True	6.33 ± 0.17	3.4
1077	0.57 ± 0.59	−1.6 ± 3.8	−5.1 ± 3.7	0.72	False	5.92 ± 0.45	64.5

Aperture radius 1.75 arcsec.

[a] Sizes can be overestimated by a factor of 1.6.

[b] Fulfils the detection threshold of being 1.5 times the noise.

[c] Gas mass assuming photoionization with electron temperature 10^4 K and electron density 0.01 cm^{-3}.

[d] Distance in kpc to the target galaxy UM260.

3.5.3 Properties of the Hα halo around UM260

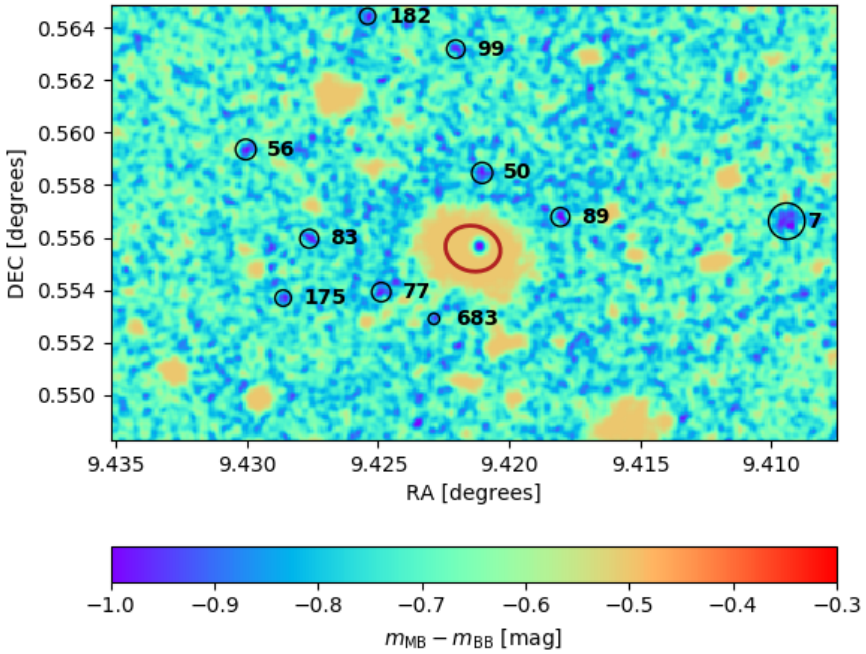

Figure 3.21: Section of $\sim 1.5 \times 1$ arcmin^2 of the color image in Fig. 3.5, smoothed with a gaussian filter of FWHM $\simeq$ 3.5 pix. Each pixel is color-coded according to $m_{\rm MB} - m_{\rm BB}$; see the bar for the color code. UM 260 is at the center. The line emission with MB$\gg$ BB shows up in deep purple. The main blobs with negative colors are encircled and numbered. Note the bluish-purplish region around the central galaxy, which we attribute to a faint Hα halo around the galaxy (e.g., sources # 50, 77, and 89 belong to this halo). Note also other conspicuous emission structures which may (or may not) be tracing high redshift emission nebulae (e.g., # 7, to the center right of the image). An ellipse with the parameters 2A, 2B and θ_0 (see Table 3.2) are drawn over UM260. The semi-major and semi-minor axis of the ellipse have been multiplicated by two so the ellipse can be seen clearly. The center of the ellipse does not match the line emission peak in UM260, and that means that the HII region of UM260 is off-center, typical of XMP galaxies (Papaderos et al. 2008; Morales-Luis et al. 2011).

A visual inspection of the color image (Fig. 3.5) reveals that UM260 has a faint emission line halo around it. Figure 3.21 is a zoom into the central region and shows that the target galaxy (in the center) is surrounded by a bluish halo, while in the rest of the background is mostly green. Even some of the identified emission line blobs are inside this halo. The blobs are encircled and labelled according to the numbers given in Table 3.4.

In order to caracterize this emission, I made surface brightness profiles around the target galaxy (Fig. 3.22). I used the program Matrioska (Borlaff et al. 2018)[11]. The inputs of the program are the image of the galaxy to which we want to obtain the surface brightness profiles and the morphological parameters needed to construct elliptical apertures centered around the galaxy. Then, for all the pixels in each elliptical aperture, it uses a bootstrapping technique to derive the median surface brightness and the confidence intervals, which are drawn from the probability distribution function of the median. The objects around the galaxy had been masked. The elliptical parameters of the galaxy had been calculated using Sextractor on the MB image. Although they are similar to those calculated on the BB image, the morphology of the galaxy in the Hα image is quite different, because it is dominated by the light of the main star forming region of UM260 (see Sect. 3.5.1 and Fig. 3.1). I think that the halo follows the general morphology of the galaxy rather than that of the star forming region.

Fig. 3.22 shows the surface brightness profiles of the target galaxy UM260 in the MB and BB images. At distance zero, the light is dominated by the central star forming region of the galaxy. At distances larger than 10 arcsec, in the outskirts of the galaxy, MB is larger than BB; this is a signature of the halo seen in the color image (Fig. 3.21). Fig. 3.23 shows a comparison between the surface brightness profile of the galaxy UM260 in the Hα image and the difference between the surface brightness profiles of MB and BB. Overall, they agree within the confidence interval of the Hα profile. However, I do not find an explanation for the disagreement between these profiles in some regions.

I calculated the total Hα flux of the halo, defined by the region in between distances 10 and 25 arcsec from the center of the galaxy. This range of distances was chosen based on the color image (Fig. 3.21). Integrating the flux between those distances, I obtain $4.0 \pm 0.7 \times 10^{-16}$ erg s^{-1} cm^{-2} over an area of 0.33 arcmin^2. One can use this flux to estimate the HII mass associated with the Hα halo using the same assumptions as with the blobs (See Sect. 3.5.2 and Eq. [2.12]), i.e., that the emission is produced by the recombination of H, the temperature is 10^4 K, and the density of the ionized gas is the typical of the CGM (~ 0.01 cm^{-3}; see Sect. 3.5.2). The total HII mass of the halo turns out to be $5.85 \pm 0.97 \times 10^7$ M$_\odot$ ($\log(M_{HII}/M_\odot) = 7.77 \pm 0.07$), which is similar to the total stellar mass of the galaxy ($\log(M_*/M_\odot) = 7.7$), and some ten times smaller than the gas mass inferred for this galaxy from HI (see Sect. 3.5.2). The HII mass of the halo is also similar to the mass in all the detected Hα blobs.

[11] https://github.com/Borlaff/Matrioska

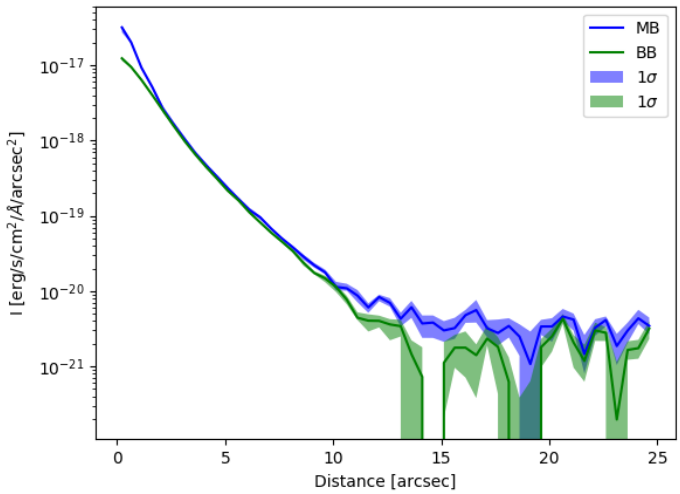

Figure 3.22: Surface brightness profiles of the galaxy UM260, calculated using the MB image (blue line) and the BB image (green line). The colored bands are the confidence intervals. See how MB > BB when distance > 10″, which is the signature of the Hα halo around the galaxy.

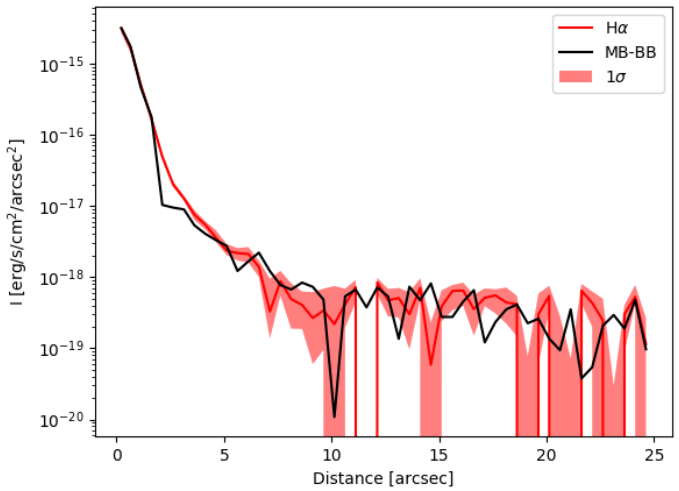

Figure 3.23: Surface brightness profiles of the galaxy UM260 calculated using the Hα image (red line with error band). It agrees with the difference of the MB and BB profiles (black line).

3.6 Discussion: Are the line emission blobs due to background sources?

The SHARDS filter was chosen to select Hα at the redshift of the target galaxy (z=0.014, see Sect. 3.3.1). However, other combinations of spectral lines and redshifts can leak into the filter producing the observed faint emission. Assuming that the rest-frame spectrum of the blobs is similar to that of an HII region, we could be observing the following lines: [OIII]λ5007 at z=0.34 $\pm$ 0.02, or [OIII]λ4959 at z=0.35 $\pm$ 0.02, or Hβ at z=0.38 $\pm$ 0.02, or [OII]λ3726 at z=0.80 $\pm$ 0.02, or CIII]λ1908 at z=2.51 $\pm$ 0.04, or Lyα at z=4.51 $\pm$ 0.07. It has been taken into account that the FWHM of the filter is 160 Å to give the range of possible redshifts.

From this point on, I analyse the pros and cons of this interpretation alternative to Hα.

If the line emission is due to background galaxies, we should be able to detect their stellar continuum. From the list of blobs, 21 (22%) are above the flux threshold for the BB image. Analysing the image around the individual blobs, we often find contamination from nearby objects, usually with more continuum emission than the blob itself. Only 4 blobs (#7, #12, #19, #83) show clear BB continuum signals. These 4 blobs have equivalent width of 290$\pm$ 50 Å, 310$\pm$90 Å, 400$\pm$300 Å, 110$\pm$130 Å, respectively. They are candidates to be extreme line emission galaxies in the background. The equivalent width is calculated at z=0.014, but the correction to rest-frame is very small. In order to analyse the general distribution of EW of the blobs, I replaced the BB flux of those blobs below the BB threshold with the value of the threshold (1.5 σ), so the EW of those blobs is a lower limit. Figure 3.24 shows the EW in the Hα image of all the blobs, disaggregating the blobs above or below the flux threshold in Hα. There are blobs with large EW that can be candidates of being pure emission line objects. As the EW is a lower limit, the blobs with low EW could also be candidates, but we can not be certain.

The typical size of the blobs is 2.33 arcsec which corresponds to 0.7 kpc at the redshift of the target galaxy. With the concordance cosmological parameters[12], the size of the background galaxy would be 11.3 kpc at z=0.34 ([OIII]λ5007), 11.5 kpc at z=0.35 ([OIII]λ4959), 12.2 kpc at z=0.38 (Hβ), 17.6 kpc at z=0.80 ([OII]λ3726), 19.0 kpc at z=2.51 (CIII]λ1908), 15.6 kpc at z=4.51 (Lyα). All the sizes correspond to very large galaxies, which are rarer as one goes to larger redshifts.

As we described in Sect. 3.5.2, the emission line blobs seem to have three

[12] $H_0 = 70$, $\Omega_M = 0.286$, $\Omega_{\rm vac} = 0.714$

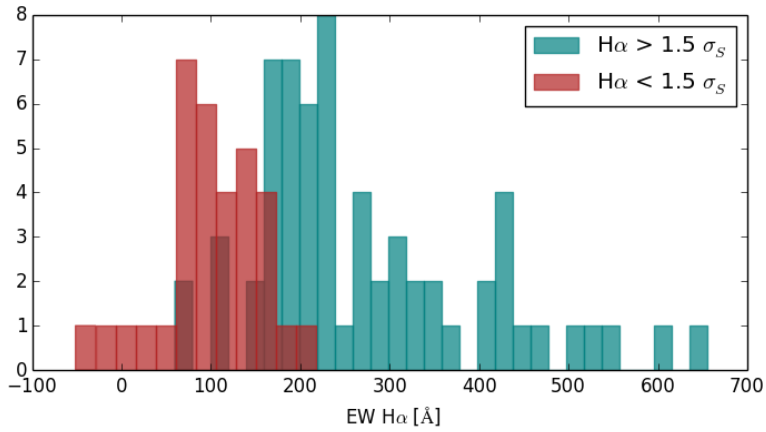

Figure 3.24: Histogram of the equivalent width of the emission assumed to be Hα at z=0.014. The EW for blobs with BB flux below the threshold is calculated using the BB threshold (1.5 times the noise) instead of the BB flux. The histogram is not normalizad, so the y-axis shows the number of blobs in each bin. The histogram in red shows the EW of the blobs with Hα flux below the threshold. The histogram in blue shows the EW of the blobs with Hα flux above the threshold.

preferred azimuths with respect to the central galaxy. If the blobs were background sources, we would expect them to be randomly distributed showing no preferred azimuth. If the blobs are at the redshift of the galaxy and they are the result of an accretion process, we could expect them to be aligned in filaments. This is indeed what it is observed. So one can discard that all blobs are background sources.

Are the blobs extended objects? Most of the blobs have a size around 2.3 arcsec, the smallest being 1.83 arcsec. But we know from Appendix 3.8.4 that the sizes are overestimated in a factor 1.6. The median FWHM of the stars in the image is around 1.4 arcsec, therefore, objects larger than 2.24 arcsec (0.67 kpc) are resolved and, so, extended. This overestimation factor is for blobs at S/N = 1.5, but 66% of blobs are above this threshold in Hα. The overestimation factor decreases with higher S/N, so the brightest blobs with sizes below 2.24 could be resolved.

The luminosity of the blobs can be used to discriminate whether they can be background sources. I will compare the luminosity of the blobs assuming that they are background sources at several redshifts with the luminosity function at those redshifts. I will assume the blobs to be CIII] emitters at redshift 2.51 or Lyα emitters at redshift 4.51. I will check whether the number of blobs

predicted by the luminosity function is smaller than the number of detected blobs, which means that the hypothesis of the blobs being emitters at those redshift is not correct.

In order to compare with the luminosity function, the completeness of the sample needs to be calculated. The standard procedure to estimate the completeness of the sample is to insert in the image a mock catalogue of objects at different luminosities and study the recovery fraction at each luminosity bin (Blanton et al. 2005; Sobral et al. 2013). We will do a simpler approach, which assumes that the blobs follow a Schechter function. We plot the logarithm of the cumulative number of blobs with luminosity higher than the luminosity bin. In the range of luminosity that we are considering, the cumulative distribution can be approximated by the exponential term of the Schechter function. When our data deviates from this behaviour is when we start to miss objects. The 90% completeness luminosity is the luminosity at which we detect the 90% of the objects predicted by the exponential term of the Schechter function. As we do not do the completeness correction, we separate the blobs above and below this threshold, and calculate a luminosity function for each set.

Then, the luminosity function is calculated by dividing the luminosity range in bins and counting the number of blobs in each bin, normalized by the width of the luminosity bin and the volume sampled by the MB filter. The volume is the FOV of the mosaic multiplied by the range in redshift covered by the filter at redshift 2.51 and 4.51. This method is similar to the V/V_{max} estimator (Avni & Bahcall 1980), without the completeness correction.

Figure 3.25 shows the luminosity function of the blobs assuming that all of them are background sources at redshift 2.51. The luminosity function of CIII] emitters at redshift ~ 1.05 is presented as comparison (Stroe et al. 2017). It is not expected much variation in the luminosity function between those redshifts. Although the red points should be corrected for the completeness of the sample, it is clear that it is very unlikely that the blobs are CIII] emiters, as the blue points are far above the luminosity function from Stroe et al. (2017).

Figure 3.26 shows the luminosity function of the blobs assuming that all of them are background sources at redshift 4.51. The luminosity function of Lyα emitters at several redshifts are presented as comparison: Herenz et al. (2019) at redshift $3 < z < 6$, Drake et al. (2017) at redshift $2.91 < z < 6.64$, Zheng et al. (2013) at redshift $z \sim 4.5$, and Dawson et al. (2007) at redshift $z \sim 4.5$.

The LF of Zheng et al. (2013) and Dawson et al. (2007) are clearly below the blue points. The points of Drake et al. (2017) and Herenz et al. (2019) are at the level of our data, considering the span of the errorbars. It is not clear whether some blobs could Lyα emitters; it depends of the LF I compare them with.

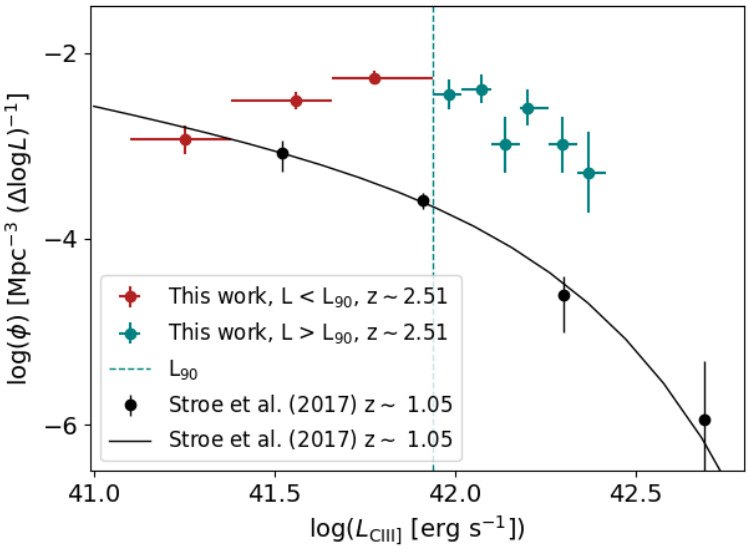

Figure 3.25: The CIII] luminosity function under the assumption that all the blobs are CIII] emitters at redshift 2.51. The blue points are the blobs with luminosity higher than the luminosity at 90% completeness. The red points correspond to the blobs with luminosity lower than the luminosity at 90% completeness. The errorbar along the x-axis gives the range of the luminosity bin and the errorbar along the y-axis is the Poissonian error from the number of blobs in each luminosity bin. The blue vertical line is the luminosity at 90% completeness. The black dots and the black line are the luminosity function of CIII] emitters at redshift ~ 1.05 from the work of Stroe et al. (2017). The black line is the Schechter fit to the black dots.

In short, I can not discard that some of the detected emission line blobs are background sources. However, there are good arguments to support that many of them belong to the CGM of UM260.

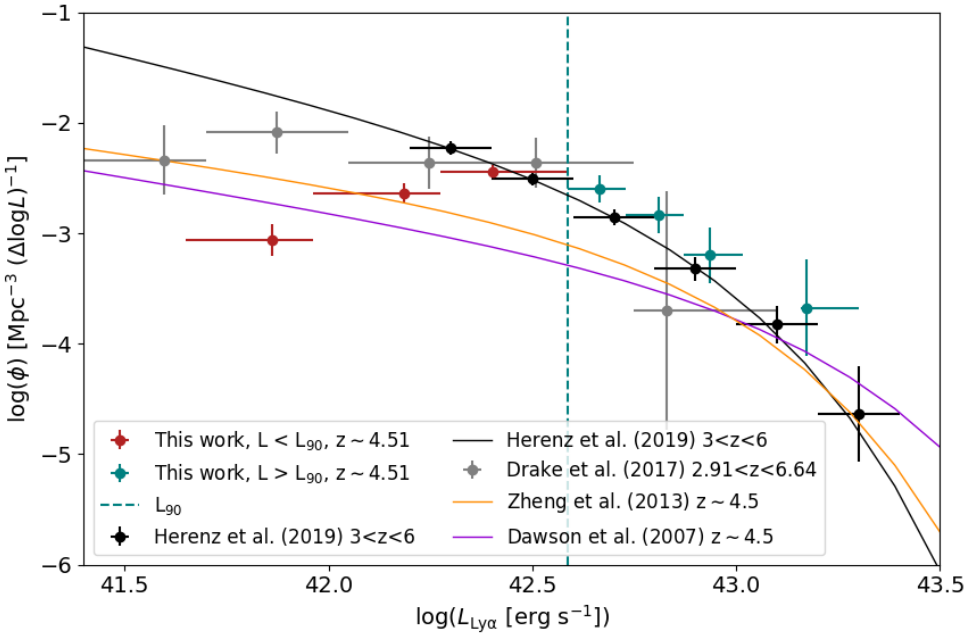

Figure 3.26: The Lyα luminosity function under the assumption that all the blobs are Lyα emitters at redshift 4.51. The blue points are the blobs with luminosity higher than the luminosity at 90% completeness. The red points correspond to the blobs with luminosity lower than the luminosity at 90% completeness. The errorbar along the x-axis gives the range of the luminosity bin and the errorbar along the y-axis is the Poissonian error from the number of blobs in each luminosity bin. The blue vertical line is the luminosity at 90% completeness. The other symbols and lines are taken from the literature and shown here for reference. Symbols are observed points whereas lines correspond to fits of observed points to a Schechter function. The black line and blacks dots are the luminosity function of Lyα at $3 < z < 6$ from Herenz et al. (2019). The grey dots are the luminosity function of Lyα at $2.91 < z < 6.64$ from Drake et al. (2017). The orange line corresponds to the luminosity function of Lyα at redshift $z \sim 4.5$ from Zheng et al. (2013). The purple line corresponds to the luminosity function of Lyα at redshift $z \sim 4.5$ from Dawson et al. (2007).

3.7 Conclusions

In this Chapter, I presented a proof-of-concept observation to detect faint Hα emission around an XMP galaxy (UM 260) using deep images taken with the 10-m GTC telescope. The images were obtained with two filters: one broad-band (BB) filter for the continuum and one medium-band (MB) filter for the Hα emission at the redshift of the target galaxy. The observing strategy and the reduction process were aimed at minimising the noise of the sky residual, which is the main limiting factor in the detection of faint sources. The key elements to achieve this goal are a combination of dithering and rotation of the FOV to map the sky around the target and avoid systematics in the camera and telescope; and the alternation of the filters in the acquisition of the images, to reduce the effect of the variation of the sky along the observing campaign. In the data reduction, systematics are reduced by the careful construction of the flat, the sky subtraction, and the combination of the images. The sky emission impacts in different ways to the two filters and has to be taken into account in the reduction process. The final image reach a magnitude limit of 28.8 mag arcsec^2 in the BB filter and 28.2 mag arcsec^2 in the MB filter (3σ, 10 arcsec box).

In order to detect emission line-dominated objects, I analyse the $m_{\rm MB} - m_{\rm BB}$ color image with a threshold to discard stars. With this procedure, I detect emission line-dominated objects all around the FOV, whose presence have been confirmed using independent detection methods. A total of 96 blobs were identified, of which 63 (66%) have a reliable detection in Hα. The measured line emission flux of the blobs is around 10^{-17} erg/s/cm^2. The size of the blobs range between $0.5 - 0.8$ kpc. Although the size of blobs with low signal to noise ratio are overestimated, it seems that most of the blobs are resolved. If we consider that the emission is not Hα at the redshift of UM260 but instead bluer emission lines at higher redshifts, the sizes increases up to 11 kpc at z=0.3 and 19 kpc at z=2.5, for example. These sizes correspond to large galaxies, which are rarer as one goes to larger redshifts. Assuming that the detected emission is Hα produced by recombination of H, and that the gas temperature and density are typical of the CGM ($T_e \simeq 10^4$ K, $n_e \sim 0.01$ cm^{-3}), I obtain gas masses for the emitting clumps around 10^6 M$_\odot$. No evident correlation was found between the mass of the object and the projected distance from the target galaxy. The distribution of the distance has two peaks at ~ 50 and ~ 70 kpc, with the farthest blob 120 kpc away. The comparison between the virial radius of UM260 (around 42 kpc) with the distance between the blobs and the target galaxy yields that some blobs may belong to the CGM of UM260, but most of them do not. On the other hand, the distribution of the azimuth of

the blobs is not uniform, indicating that there is a preference of the blobs to be along certain directions with respect to the target galaxy. If all the blobs were background sources, we would expect them to be randomly distributed showing no preferred azimuth. From the analysis of the luminosity function, we can discard that the blobs are CIII] emitters at redshift 2.51, however it is not as clear in the case of Lyα at redshift 4.51. These arguments tells us that the detected emission line blobs may belong to the CGM of UM260, and that the possibility that some of them may be background sources can not be fully discarded.

Apart from the emission line blobs, I also detect a low surface brightness emission halo surrounding the target galaxy. This halo was identified first in $m_{\rm MB} - m_{\rm BB}$ and then analysed using surface brightness profiles in the Hα, MB and BB images. The total flux of the halo, defined by the elliptical apertures enclosed within 10 and 25 arcsec from the center of the galaxy, is 4.0 $\pm$ 0.7 $\times 10^{-16}$ erg s^{-1} cm^{-2} over an area of 0.33 arcmin^2. With the same assumptions as with the blobs, the total mass of the halo is $6 \pm 1 \times 10^7$ M$_\odot$. The mass of the halo has the same order of magnitude as the total stellar mass of the galaxy and about ten times smaller than the gas mass inferred from HI.

As future work, we will make a spectroscopic follow up of the extended emission and the emission line blobs. These observations will allow us to confirm the existence of diffuse line emission around UM260, to infer the redshift of such emission, and to constraint the physical properties of emitting gas. We can infer the kinematics from the brightest emission line and the metallicity from line ratios. This is part of an ongoing project that will sample more XMP galaxies selected in Appendix A .

3.8 Appendixes

3.8.1 Integration times for an optimal photon-noise limited signal-to-noise ratio

The emission of the sky at a good astronomical site, including the Observatorio del Roque de los Muchachos (ORM), is of the order of 21 mag arcsec^{-2} at around 6000Å (e.g., Benn & Ellison 1998; Pedani 2004). Thus, removing sky emission is mandatory to go deep. However, the photon noise introduced by the sky emission cannot be removed, and this noise provides the ultimate limiting factor of any deep observation.

Typically, the sky emission is removed by subtracting two images (or spectra) taken quasi-simultaneously, one including the target[13] (T) and another reference image without it (R),

$$T = (W + A)\,\tau_T\,\Delta\lambda_T\beta_T, \tag{3.18}$$

$$R = (C + A)\,\tau_R\,\Delta\lambda_R\beta_R.$$

The contribution of the sky A goes away from the observed image, O, when it is defined as,

$$O = T - \alpha R = (W - C)\,\tau_T\,\Delta\lambda_T\beta_T, \tag{3.19}$$

provided the scaling factor is chosen as,

$$\alpha = \frac{\tau_T\,\Delta\lambda_T\beta_T}{\tau_R\Delta\lambda_R\beta_R}. \tag{3.20}$$

The symbols in Eq. (3.18) stand for the target emission per unit wavelength and time, W, the sky emission per unit wavelength and time, A, the emission in the reference field which is not associated with the sky, C, the integration time on target, τ_T, the integration times on the reference field, τ_R, the width of the color filter used for the target, $\Delta\lambda_T$, and the width of the color filter used for the reference field, $\Delta\lambda_R$. The filters used on target and on reference have peak transmissions of β_T and β_R, respectively.

Assuming the noise to be dominated by the sky emission photon noise, the signal to noise ratio of the observation is given by,

$$S/N = \frac{O}{\sigma_O} = S/N_\tau\Big[\frac{f}{(1+f)(1+gf)}\Big]^{1/2}, \tag{3.21}$$

with σ_O representing the noise in O,

$$\tau = \tau_T + \tau_R,$$

[13]Keep in mind that this appendix is self contained and so follows its own notation.

$$f = \tau_T/\tau_R,$$
$$g = \Delta\lambda_T\beta_T/(\Delta\lambda_R\beta_R).$$

and

$$S/N_\tau = \frac{(W-C)\Delta\lambda_T\beta_T\tau}{\sqrt{A\Delta\lambda_T\beta_T\tau}}. \tag{3.22}$$

The symbol S/N_τ stands for the S/N to be obtained if the sky emission just produces noise but does not contaminate the signals, and if all the observing time τ is employed on target. In other words, S/N_τ is the S/N provided by the exposure time calculator (ETC) of an instrument once the magnitude of the source and the integration time are set.

The question arises as how to maximize S/N given the constrains produced by the observational setup (i.e., $\Delta\lambda_T, \beta_T, \Delta\lambda_R, \beta_R$), and once the total integration time τ is fixed. The only degree of freedom left is f, i.e., the ratio between the integration times on target and at the reference. This is obtained finding the solution for $d(S/N)/df = 0$, which renders

$$f = 1/\sqrt{g} \quad \text{or equivalenty,} \qquad \frac{\tau_T}{\tau_R} = \Big(\frac{\Delta\lambda_R\beta_R}{\Delta\lambda_T\beta_T}\Big)^{1/2}, \tag{3.23}$$

with the maximum S/N, $S/N_{\rm max}$, given by

$$S/N_{\rm max} = \frac{S/N_\tau}{1+\tau_R/\tau_T}. \tag{3.24}$$

In short, once g is set, the largest S/N is produced for τ_T/τ_R given by Eq. (3.23).

In our particular case, T and R correspond to the images with a medium-band filter (MB) and a broad-band filter (BB) around the Hα line, respectively. We use the r SDSS filter for BB, and a SHARDS filter for MB (Pérez-González et al. 2013), which approximately have widths of $\Delta\lambda_R \sim 1500$ Å and $\Delta\lambda_T \sim 150$ Å, respectively. Assuming that the peak transmission in both filters is similar ($\beta_T \sim \beta_R$), then the optimum ratio of integration times given by Eq. (3.23) is,

$$\frac{\tau_T}{\tau_R} \simeq \sqrt{10} \simeq 3.3, \tag{3.25}$$

which yields a S/N not far from the ideal case of using all the time to integrate in the MB,

$$S/N_{\rm max} \simeq 0.77\, S/N_\tau. \tag{3.26}$$

Thus, in our observations, the total exposure time is split in a ratio 1/3 in order to maximize the signal to noise ratio in the image difference between the two filters.

3.8.2 Noise in an aperture

The purpose of this appendix is to describe the derivation of the noise in a given aperture of arbitrary size from the noise per pixel in the images. The units of the calibrated images are erg s^{-1} cm^{-2} $\mathring{A}^{-1}$ pix^{-1}, as set in the photometric calibration. The symbol I_i is used to denote the value of the image in these units in the i-th pixel. In the following equations, it is assumed to have a noise, with a standard deviation σ_i.

The noise measured in square boxes of side 1 arcsec is defined to be σ''_1. As explained in Section 3.3.3, to calculate the limiting magnitude of the image we place square boxes of area 1 $arcsec^2$ in sky only regions. Then, the total flux inside them is calculated and divided by the total surface of the box in $arcsec^2$, (i.e., 1 $arcsec^2$). The limiting magnitude is set by the standard deviation of the surface brightness considering all the boxes. This limiting value corresponding to a 1 arcsec aperture can be scaled to any other aperture size as explained below.

The mean flux in the 1 arcsec aperture is defined as,

$$\overline{I_i} = \frac{\sum_i^{1''} I_i}{\sum_i^{1''} 1}, \tag{3.27}$$

where I_i is the flux in every pixel, $\sum_i^{1''}$ the sum over all pixels in the aperture of size 1 $arcsec^2$, so equal to $N_{1''}$ the number of pixels in the aperture. Applying the equation of propagation of errors to Eq. (3.27), the standard deviation of the mean flux in an aperture of 1 $arcsec^2$ ($\sigma_{\overline{I_i}}$) is related to the standard deviation in every pixel (σ_i) as,

$$\sigma^2_{\overline{I_i}} = \sum_i^{1''} \left(\sigma_i^2/N_{1''}^2\right) = \left(\sigma_i^2/N_{1''}^2\right) \sum_i^{1''} 1 = \left(\sigma_i^2/N_{1''}^2\right) N_{1''} = \sigma_i^2/N_{1''}, \tag{3.28}$$

where we have assumed that the standard deviation of the noise of I_i (σ_i) is constant within the 1 arcsec aperture. Thus,

$$\sigma_{\overline{I_i}} = \sigma_i/\sqrt{N_{1''}}. \tag{3.29}$$

We want to express the signal in units of erg s^{-1} cm^{-2} $\mathring{A}^{-1}$ $arcsec^{-2}$, so we divide the flux in a pixel by its surface, i.e., $S_i = I_i/\Delta x^2$ where Δx^2 is the area of a pixel: 0.25^2 $arcsec^2$. With the previous equations, the average surface brightness in the aperture is,

$$\overline{S_i} = \frac{1}{N_{1''}} \sum_i^{1''} I_i/\Delta x^2 = \frac{1}{\Delta x^2 N_{1''}} \sum_i^{1''} I_i, \tag{3.30}$$

and its variance is given by:

$$\sigma^2_{\overline{S_i}} = \frac{1}{\Delta x^4 N^2_{1''}} \sum_i^{1''} \sigma_i^2 = \frac{\sigma_i^2}{\Delta x^4 N_{1''}} \tag{3.31}$$

The symbol $\sigma_{1''}$ was defined as the variance of the fluctuations of the sky in an aperture of 1 arcsec^2, and is given by the square root of the previous equation,

$$\sigma_{1''} \equiv \sigma_{\overline{S_i}} = \frac{\sigma_i}{\Delta x^2 \sqrt{N_{1''}}}, \tag{3.32}$$

and using Eq. (3.29), it is also,

$$\sigma_{1''} = \sigma_{\overline{I_i}} \frac{1}{\Delta x^2}. \tag{3.33}$$

We will use the previous equations to calculate the standard deviation of the surface brightness of the sky over apertures of different sizes. This is needed to quantify the uncertainties in the photometry. The signal integrated in an aperture of size A, which has units of erg s^{-1} cm^{-2} Å^{-1} pix^{-1}, is,

$$S = \sum_i^A I_i, \tag{3.34}$$

where the sum $\sum_i^A$ is extended to the full aperture, and so $\sum_i^A 1 = N_A$, the number of original pixels in the aperture. The propagation of error leads to,

$$\sigma_S^2 = N_A \sigma_i^2 \rightarrow \sigma_S = \sqrt{N_A}\, \sigma_i. \tag{3.35}$$

Inserting σ_i from Eq. (3.32),

$$\sigma_S = \sqrt{N_A}\, \sigma_{1''}\, \Delta x^2\, \sqrt{N_{1''}}, \tag{3.36}$$

and then using Eq. (3.33),

$$\sigma_S = \sqrt{N_A}\, \sigma_{\overline{I_i}}\, \sqrt{N_{1''}}. \tag{3.37}$$

This expression becomes more compact when expressed in terms of the fluctuations of the mean surface brightness averaged over the aperture,

$$\overline{S_A} = \frac{1}{\sum_i^A 1} \sum_i^A I_i / \Delta x^2, \tag{3.38}$$

and

$$\sigma_A^2 = \frac{1}{\Delta x^4 N_A^2} \sum_i^A \sigma_i^2 = \frac{1}{\Delta x^4 N_A^2} \sigma_i^2 \; N_A = \frac{\sigma_i^2}{\Delta x^4 N_A}, \tag{3.39}$$

$$\sigma_A = \frac{\sigma_i}{\Delta x^2 \sqrt{N_A}} \tag{3.40}$$

Combining Eq. (3.35) and (3.40) one finds,

$$\sigma_S = \sqrt{N_A} \; \sigma_A \; \sqrt{N_A} \; \Delta x^2 = \sigma_A \; \Delta x^2 \; N_A. \tag{3.41}$$

Equation (3.41) gives the standard deviation of the noise integrated in an aperture of area A (σ_S), from the standard deviation of the surface brightness fluctuations (σ_A) in apertures of the same size. It is the equation we use in Section 3.4.3 for the uncertainties in the photometry and the flux threshold.

3.8.3 Detection limit of NoiseChisel

NoiseChisel (Akhlaghi & Ichikawa 2015) is a program designed to detect low surface brightness objects, so I used it as a independent check to confirm the presence of the emission line blobs. To that end, we tested the detection limit and compare it with the standard limit in SExtractor (Bertin & Arnouts 1996). The test described in this Appendix is complementary to the published tests in (Akhlaghi & Ichikawa 2015) and was suggested by the author M. Akhlaghi (private communication).

The tests were carried out with mock images made out of a disk plus noise. The noise is gaussian distributed with mean 0 and standard deviation 1. The signal to noise ratio is varied changing the amplitude of the signal in the disk. The diameter of the disk is 40 pixels, which approximately corresponds to the size of the target galaxy UM260 (plate scale 0.25 arcsec/pix). We made different images decreasing the signal of the circle compared to the sky noise. We repeated the test with different image sizes, which only enlarges the size of the noise region, providing better statistics for the noise.

Figure 3.27 shows the fraction of the disk recovered by NoiseChisel as a function of the signal to noise ratio, given by the amplitude of the disk since the noise always has standard deviation of one. Figure 3.27 shows that part of the object starts to be missed when S/N < 0.4. Half of the true area is detected when S/N goes from 0.15 to 0.25 depending on the image sizes. What is important in this context is the fact that NoiseChisel performs well at a S/N below the lowest recommended detection threshold of SExtractor (Bertin & Arnouts 1996), which is S/N = 1 (Holwerda 2005).

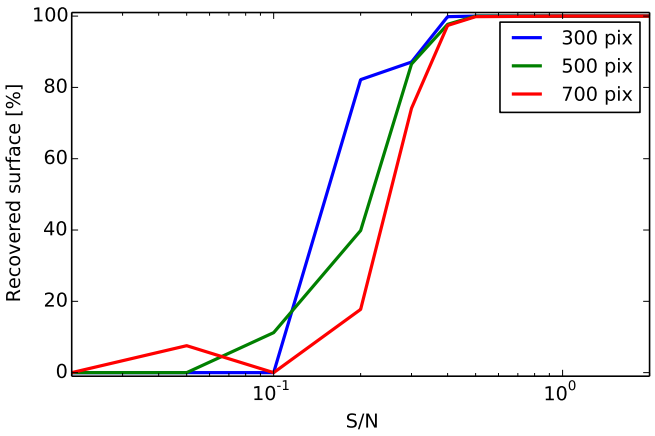

Figure 3.27: Detection limit of NoiseChisel. It shows the percentage of surface of the disk in the mock image recovered by the program at various S/N. Each line corresponds to different image sizes; the value given in the legend is the number of pixels along one side of the test image.

3.8.4 Overestimation of the blob sizes

Noise in the images artificially increases the estimated sizes. I made some tests to calculate the uncertainties produced by this effect. First, I added noise to a 2D gaussian profile that simulates the object. Then we employ the same equations used to estimate sizes in the main text with these fake noisy objects. The noise always has the same characteristics; it is drawn from a gaussian distribution of mean 0 and standard deviation 1. The object is symmetric and its amplitude increases in each iteration. Three different values are used for the width of the object; FWHM of 1.18, 2.35 and 3.53 arcsec. The original image size of 14×14 pixels (is equal to the diameter of the aperture for the photometry), but I also use 20×20 pixels and 28×28 pixels (side of 3.5, 5 and 7 arcsec respectively). Noise creates pixels with negative flux. They were set to zero to avoid problems in the computation of the barycenter, which assumes the signal to be positive. The image of a simulated object is given in Fig. 3.28.

I use the same equations described in Sect. 3.4.3 to calculate the size and the photometric noise of the fake object. Figure 3.29 shows the dependence for the inferred size and the signal to noise ratio of the fake object. The figure shows that the size of a blob is overestimated at low signal to noise ratio, meanwhile at high signal the true size is recovered. The smallest size that can be measured is limited by the size of the pixel. The largest size is set by size of the image.

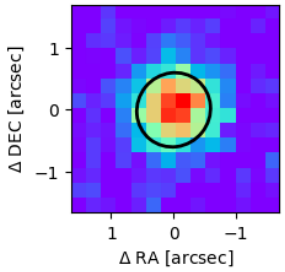

Figure 3.28: Image of the simulated object. The units of the horizontal and vertical axis are arcsec from the barycenter. The black ellipse is drawn with the parameters A and B described in Eqs. (3.15) and (3.16). The size of this image is 3.5×3.5 arcsec^2 with the FWHM of the simulated object set to 1.18 arcsec.

When the size of the simulated object gets closer to the size of the image, we do not recover the FWHM of the 2D gaussian in the model because the gaussian is severely truncated, but the measured size is actually correct.

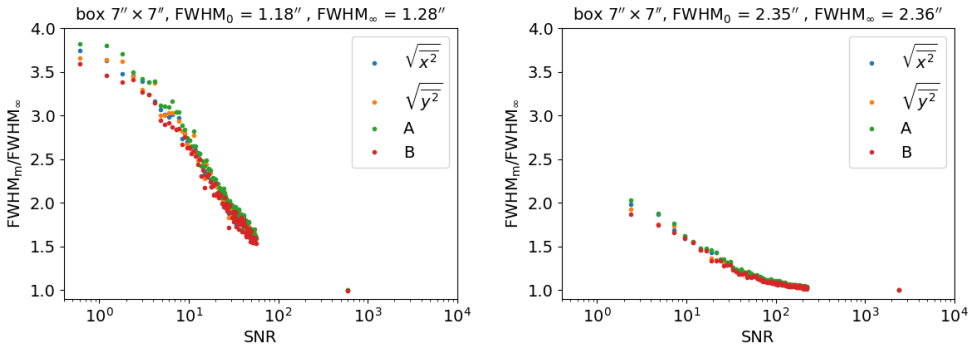

(a) (b)

Figure 3.29: Variation of the measured size with the signal to noise ratio (S/N) of the fake object. The measured size is normalized to the value in the limit of high signal to noise. The points represent the measured size calculated using different second order moments: along the x-axis (blue), the y-axis (yellow), the major axis (green), and the minor axis of the ellipse (red). As the simulated object is symmetric, these four values should be equal, as it can be seen in the figure at high S/N. At low S/N, the noise introduces some eccentricity, making these values different. This simulation was carried out on an image of 7×7 arcsec^2 with the FWHM of the simulated object set to (a) 1.18 arcsec and (b) 2.35 arcsec. It can be seen how the overestimation drops as the size of the simulated object increases.

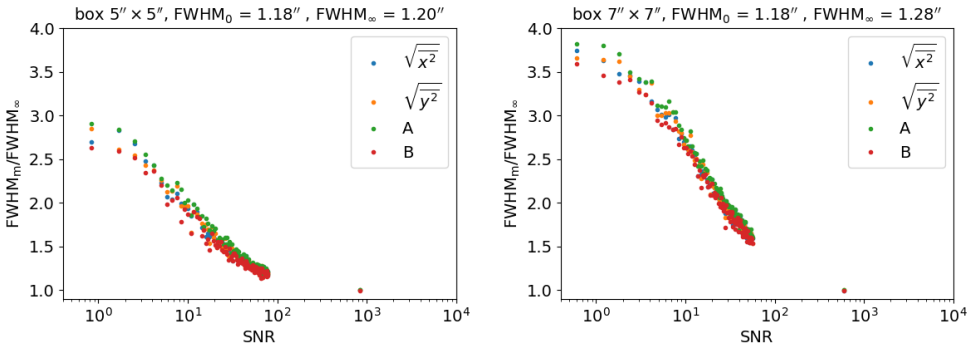

(a) (b)

Figure 3.30: Similar to Fig. 3.29. In this case the FWHM of the simulated object is 1.18 arcsec with the size of the image set to (a) 5×5 arcsec^2 and (b) 7×7 arcsec^2 . The overestimation increases with the size of the image.

When we enlarge the size of the simulated object, keeping the size of the image constant, the size converges faster to the high signal to noise limit, so the overestimation is reduced. This happens in all image sizes. This can be seen comparing Figures 3.29a and 3.29b. Enlarging the size of the image, keeping the size of the simulated object constant, the overestimation at low signal to noise ratio increases. At every signal to noise ratio, the larger the image size the larger the overestimation. This can be seen in Figures 3.30a and 3.30b.

All of these simulations tell us that the overestimation is reduced using smaller apertures, so, we use the 3.5×3.5 arcsec^2 box when measuring blob sizes in real images. For this aperture, the overestimation factor is around 1.6, considering the signal to noise ratio of 1.5 that we use in the observed Hα images (see Fig. 3.31).

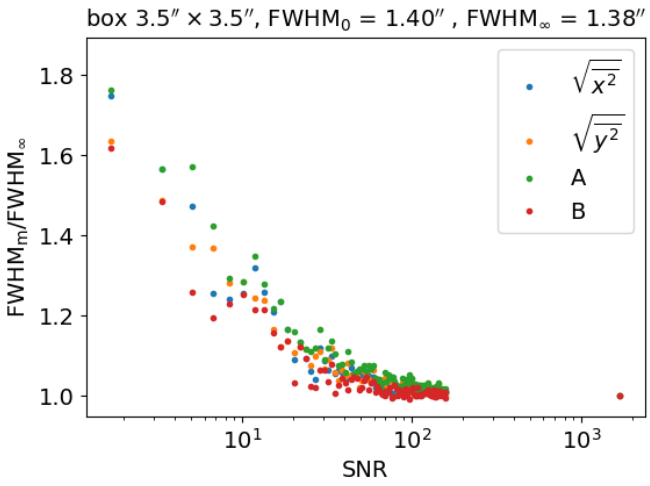

Figure 3.31: Similar to Fig. 3.29. In this case the FWHM of the simulated object is 1.4 arcsec (FWHM of stars in MB image) with the size of the image set to 3.5×3.5 arcsec^2. At super-low signal to noise ratio, the overestimation of the measured sizes is around 2. At S/N=1.5, it is about 1.6, which is the bias to be expected in the real Hα observation.

4

An XMP host galaxy: the high gas-phase metallicity of the ultra-diffuse galaxy UGC 2162[1]

4.1 Scientific rationale

In previous chapters we have discussed the properties of XMP galaxies, mainly focusing on the star forming region of the galaxy, but what can we say about the rest of the galaxy? The galaxies hosting the XMP starburst are low surface brightness galaxies with a metallicity around half the solar metallicity ($Z_g \sim Z_\odot/2$; Sánchez Almeida et al. 2015). We will call them *host galaxies*. Since the gas accretion process is stochastic, there should be galaxies with the properties of the host galaxies, i.e., relatively high metallicity for their mass, low surface brightness, and without the bright low metallicity star-forming region (i.e., *XMP host galaxies*). However, such galaxies have not been identified before. Low surface brightness galaxies are also faint galaxies (e.g., Skillman 1999) which, according to the luminosity–metallicity relation (e.g., Berg et al. 2012), are metal poor. Actually, a few known low surface brightness dwarf galaxies with mean metallicity determined through the direct-method (DM; details in Sect. 4.2.2) seem to be XMP (e.g., Leo P by Skillman et al. 2013; Leoncino Dwarf by Hirschauer et al. 2016; and Little Cub by Hsyu et al. 2017).

UGC 2162 may be an exception compared to these low surface brightness

[1]This work partly appeared in Sanchez Almeida, Olmo-Garcia et al. (2018b)

dwarf galaxies with known metallicity, and so, it may be the sought-after XMP host galaxy that provides support to the whole picture. It may be one of the expected host galaxies, without a metal-poor starburst. It has been recently identified as a nearby low-mass UDG[2] by Trujillo et al. (2017), with $M_\star \simeq 2 \times 10^7 M_\odot$, $M_{\rm HI}/M_\star \simeq 10$, and $M_{dyn}/M_\star \simeq 200$ ($M_\star$, $M_{\rm HI}$, and M_{dym} stand for the stellar mass, the HI mass, and the dynamical mass, respectively). With an effective radius of 1.7 kpc, its g-band central surface brightness is 24.4 mag arcsec^{-2}. The galaxy is irregular with several bluish star-forming knots (Fig. 4.1). UGC 2162 belongs to the group of M77, even though it is quite far from the central galaxy (293±40 kpc projected distance; Trujillo et al. 2017). One of these knots has a spectrum in the Sloan Digital Sky Survey Data (SDSS-

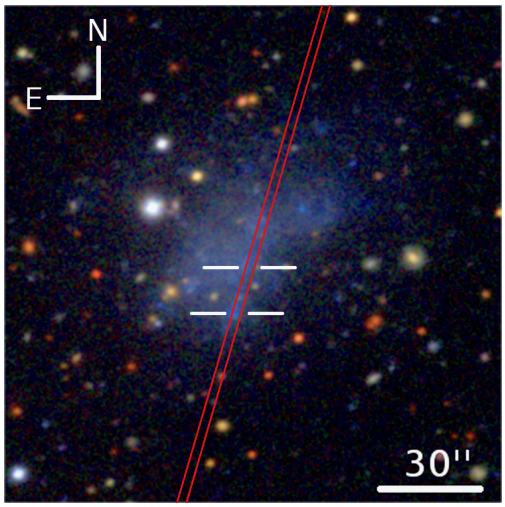

Figure 4.1: Composite image of UGC 2162 in g, r, and i from the IAC Stripe 82 Legacy Project (Fliri & Trujillo 2016). The white ticks indicate the location of the two star-forming regions mentioned in the main text, with their spectra shown in Figs. 4.2 and 4.3. The orientation of the spectrograph slit during GTC observations is shown in red. A 30 arcsec scale has been included for reference. North (N) and east (E) are also indicated. This image has been tweaked to appear brighter and be seen clearly in the printed version.

[2]The term UDG (Ultra Diffuse Galaxy) was recently introduced by van Dokkum et al. (2015), and it quickly became widely used in the literature despite the fact it describes galaxies which were already known as low surface brightness dwarf ellipticals or dwarf irregulars, depending on whether they reside in clusters or the field (e.g., Impey & Bothun 1997; Dalcanton et al. 1997; Conselice 2018). We have decided to stick to the now popular terminology, acknowledging that the word UDG could be replaced throughout the text with *low surface brightness dwarf irregular* without altering the content of the chapter.

DR12, Alam et al. 2015). Using the line ratio N2 ([NII]λ6583/Hα) derived from the SDSS spectrum, and the calibration by Pettini & Pagel (2004), Trujillo et al. (2017) estimate an oxygen abundance for the star-forming ionized gas of $12+\log(\mathrm{O/H}) = 8.22\pm0.07$, which corresponds to 1/3 of the solar abundance[3]. If this metallicity estimate is correct, the gas of UGC 2162 is of high metallicity for its mass and magnitude, in the vein expected for the galaxies that, when hosting a metal-poor starburst, give rise to the observed XMP galaxies[4].

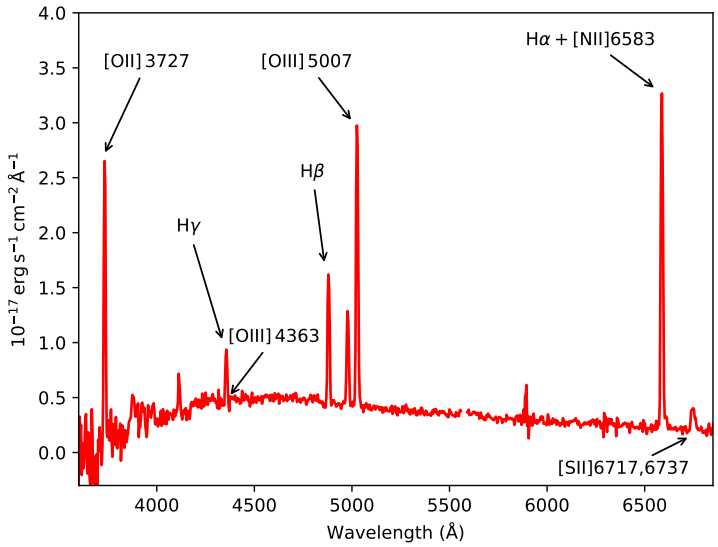

Figure 4.2: GTC spectrum corresponding to the brightest knot of UGC 2162 (the southmost in Fig. 4.1). The position of the main emission lines used to estimate the metallicity are labeled, including [OIII]λ4363, even though is below the detection threshold. Hγ is also labeled for clarity to avoid confusion with [OIII]λ4363.

The reported high metallicity of UGC 2162 rests only on the low signal-to-noise ratio (S/N) SDSS spectrum, and on the estimate of its metallicity using N2. Due to the importance of the gas-phase metallicity of this particular galaxy, we obtained long-slit spectra of UGC 2162 with the 10-m GTC telescope, with enough wavelength coverage and S/N to carry out an independent robust determination of the gas-phase metallicity. The analysis of these spectra confirms the high metallicity of the star-forming gas in UGC 2162 (Sect. 4.2).

[3] With $12+\log(\mathrm{O/H})_\odot = 8.69$, from Asplund et al. (2009).

[4] As I did throughout the thesis, I use the term *XMP galaxy* to denote a host galaxy plus one or a few metal-poor starbursts which outshine the emission line spectrum of the host, so that the light-weighted average metallicity of the combined system is smaller than a tenth of the solar metallicity.

The purpose of this chapter is to present this determination, and to show that UGC 2162 shares many properties in common with those expected for the host galaxies having XMP star-forming regions (Sect. 4.3). There seem to be a few other objects in the literature with the characteristics of UGC 2162. Discussions are included in Sect. 4.4.

4.2 Observations and metallicity determination

4.2.1 Observations

We obtained long-slit spectra of UGC 2162 integrating for 2 hours with the instrument OSIRIS at the 10-m GTC telescope[5]. The 1 arcsec wide slit was placed as shown in Fig. 4.1, inclined with respect to the major axis so as to cover the two main star-forming regions of the galaxy and the diffuse emission around them. The resulting visible spectra span from 3600 to 7200 Å with a spectral resolution around 550, thus covering the wavelength range containing [OII]λ3727 and the temperature sensitive line [OIII]λ4363. The raw data were reduced following the usual procedure which includes correction for bias and flat-field, and flux and wavelength calibration. We employ PyRAF[6] for the task. Figure 4.2 shows one of the resulting spectra, corresponding to the brightest knot of the galaxy (the southmost in Fig. 4.1). The slit was not oriented along the parallactic angle, however, differential refraction is not an issue since the airmass of observation is low (< 1.2), and the residual effect is corrected for by the flux calibration.

4.2.2 Metallicity determination

The DM is the method of reference to measure metallicities when all the required emission lines are available (e.g., Stasińska 2004; Pérez-Montero 2017). It obtains the physical properties of the emitting gas from the same spectrum used to determine the metallicity, minimizing the model dependence of the result. In the case of the oxygen abundance, the emission-line ratio [OIII]λ4363/[OIII]λ5007 is needed to determine the electron temperature of the nebulae and so to determine the oxygen abundance using the DM (e.g., Osterbrock 1974; Pérez-Montero 2017). As it happened with the SDSS spectrum analyzed by Trujillo et al. (2017), [OIII]λ4363 does not show up above the noise level even in the GTC spectra. The 2D spectrum around [OIII]λ4363

[5] `http://www.gtc.iac.es/instruments/osiris/osiris.php`

[6] PyRAF is a product of the Space Telescope Science Institute, which is operated by AURA for NASA `http://www.stsci.edu/institute/software_hardware/pyraf/`

is shown in Fig. 4.3a. [OIII]λ4363 is prominent in low metallicity HII regions (e.g., Ly et al. 2015; Sánchez Almeida et al. 2016) and so the non-detection already suggests the high metallicity of the gas in the galaxy. On the other hand, the non-detection implies that we cannot use the DM to infer the gas-phase metallicity. We employ the code HII-CHI-mistry (HCm) to determine O/H. HCm compares the observed emission line fluxes of a selected number

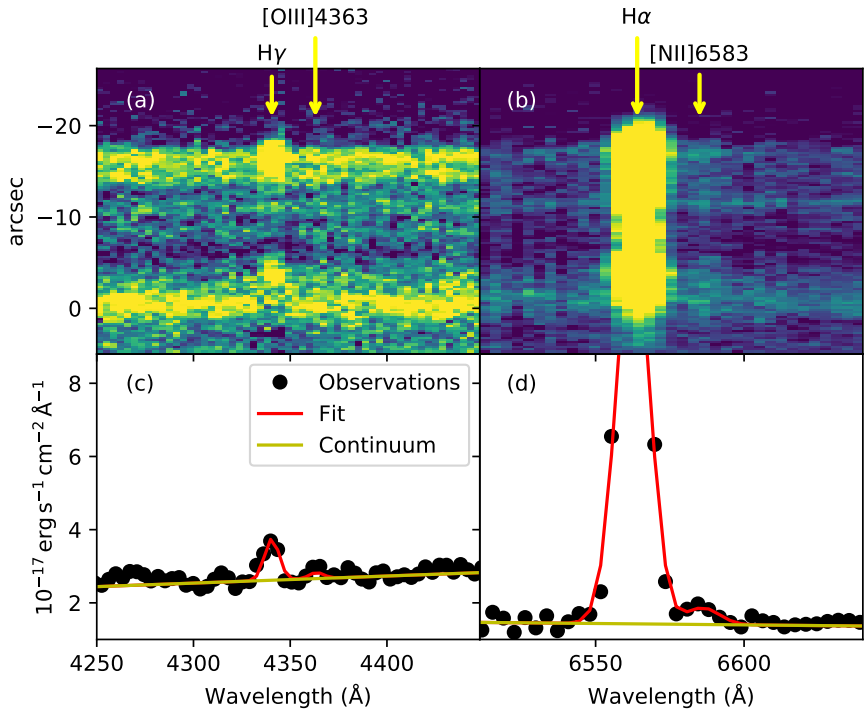

Figure 4.3: (a) Image with the part of the 2D spectrum which should contain [OIII]λ4363. The horizontal and the vertical directions correspond to wavelength and position along the slit, respectively. The color palette goes from dark blue to yellow from low to high signal. Hγ, at 4340 Å shows up clearly. However, any possible signal of [OIII]λ4363 is buried within the noise level. (b) Same as (a) for the spectral region around Hα. The faint [NII]λ6583 is barely visible in the red wing of Hα. (c) Fit with two Gaussians and a continuum to the spectral region around [OIII]λ4363. The observed spatially integrated spectrum of the galaxy is presented as solid symbols whereas the red and the yellow lines stand for the full fit and the continuum, respectively. (d) Same as (c) for the spectral region around Hα. [NII]λ6583 stands out above the noise level.

of lines with a grid of photoionization models, finding the best fit through a least-squares minimization algorithm (Pérez-Montero 2014). In principle, HCm employs the fluxes of [OII]λ3727, [OIII]λ4363, [OIII]λ5007, [NII]λ6583, and [SII]$\lambda\lambda$6717,6737, relative to Hβ and corrected for reddening. However, HCm was chosen because it can be used without [OIII]λ4363, and it is robust in the sense of being equivalent to the direct method when [OIII]λ4363 is available (Pérez-Montero 2014; Sánchez Almeida et al. 2016; Calabrò et al. 2017). The fluxes of the required emission lines were obtained fitting a Gaussian plus a linear continuum to each emission line. In the case of two overlapping lines, the two Gaussians were fitted simultaneously. Examples are given in Figs. 4.3c and 4.3d. Dust extinction was considered and corrected for following the usual approach of assuming a Milky Way extinction law (Cardelli et al. 1989), with the ratio between Hα and Hβ given by the case B recombination at high electron temperatures in HII regions (i.e., 2.76; Osterbrock 1974). The flux ratios thus obtained are collected in Table 4.1, with the corresponding oxygen abundances given in Table 4.2, column 1. The four rows correspond to four different spatial averages of the observed long-slit spectrum: the full galaxy, two bright points, and the diffuse component. In terms of the distances represented in Fig. 4.3a, the full galaxy considers the average spectrum from $-21''$ to $+1''$, the first bright point from $-19''$ to $-15''$, the second bright point from $-8''$ to $-3''$, and the diffuse component from $-15''$ to $-6''$ (see also the ticks in Fig. 4.1). Thus the spectra of the two bright points and the diffuse component come from different parts of UGC 2162, whereas the full galaxy spectrum basically averages out the three of them. In all four cases the metallicity is relatively high, with $12 + \log(\mathrm{O/H})$ between 8.3 and 8.7 (Table 4.2, column 1). This range of values is within the error bar of the measurement, as we discuss in the next paragraph.

HCm provides formal error bars from the difference between the observed fluxes and those provided by the photoionization models. They are rather small

Table 4.1: Emission line flux ratios used in the metallicity determination.

Component	[OII]λ3727	[OIII]λ4363	[OIII]λ5007	[NII]λ6583	[SII]$\lambda\lambda$6717,6737
Full Galaxy	2.35 ± 0.17	< 0.04	1.61 ± 0.05	0.17 ± 0.05	0.94 ± 0.05
1st Bright Point	1.91 ± 0.14	< 0.02	2.11 ± 0.07	0.09 ± 0.05	0.43 ± 0.05
2nd Bright Point	2.29 ± 0.20	< 0.05	1.50 ± 0.05	0.11 ± 0.05	0.92 ± 0.05
Diffuse Emission	2.89 ± 0.37	< 0.05	0.99 ± 0.05	0.13 ± 0.06	0.96 ± 0.05

NOTE — The dimensionless flux ratios are relative to Hβ and corrected for reddening assuming Hα/Hβ = 2.76. Error bars are statistical errors inferred from fitting the observed emission lines to Gaussian functions.

Table 4.2: Different estimates of $12 + \log(\mathrm{O/H})$ in UGC 2162.

Component	HCm No [OIII]λ4363 (1)	HCm Monte Carlo (2)	Direct Method Monte Carlo (3)	N2-based GTC (4)	N2-based SDSS (5)
Full Galaxy	8.38 ± 0.06	...	...	8.12 ± 0.11	8.22 ± 0.07
1st Bright Point	8.29 ± 0.08	$8.52^{+0.27}_{-0.24}$	$8.22^{+0.39}_{-0.18}$	8.05 ± 0.14	...
2nd Bright Point	8.40 ± 0.06	...	...	8.11 ± 0.10	...
Diffuse Emission	8.70 ± 0.02	...	...	8.14 ± 0.12	...

NOTE — (1) Values with the formal error bars provided by HCm.
(2) Monte-Carlo simulation assuming the [OIII]λ4363 flux randomly distributed with values below the observed noise. The table lists the median and the 1-σ error bar of the resulting distribution, with the error given by the values between percentiles 15.9 % and 84.1 %.
(3) Same as (2) for metallicities based on the DM.
(4) Based on the index N2, with the same calibration employed by Trujillo et al. (2017).
(5) As given by Trujillo et al. (2017).

(< 0.1 dex; see Table 4.2), and do not include the uncertainty associated with the non-detection of [OIII]λ4363. In order to be conservative and include this other source of error, we developed an alternative way to evaluate the error bars of the measured abundances. We carried out a Monte-Carlo simulation where [OIII]λ4363 was assumed to have a flux smaller than the upper limit set by the noise of the GTC spectra. Specifically, we assume [OIII]λ4363 to be drawn from a uniform distribution consistent with the noise in the observation, with values going from zero to the value set by the Gaussian function fit to the noise shown in Fig. 4.3c. We drew 1000 random values, from which we compute the median and the 1-σ error bar (i.e., the range of values in between percentiles 15.9 % and 84.1 %). The result for the brightest point is given in Table 4.2, column 2. The measurement, along with its error bar, provides the range of values of $12 + \log(\mathrm{O/H})$ consistent with the noise level of the GTC spectra. The range is consistent with the value inferred from a single application of HCm, except that the error bars are significantly larger. We repeated the same exercise with the metallicities inferred applying the DM[7]. The result is given in Table 4.2, column 3. Once again, the result is consistent with the high metallicity inferred by Trujillo et al. (2017) from the SDSS spectrum. In the case of Trujillo et al. (2017), they used the line ratio N2 ([NII]λ6583/Hα) to estimate $12 + \log(\mathrm{O/H})$ as calibrated by Pettini & Pagel (2004). We have repeated the same exercise with the GTC spectra, and the metallicities inferred from N2 also agree: compare the N2-based metallicity from the full galaxy GTC spectra, Table 4.2 column 4, with the metallicity worked out in Trujillo et al. (2017), Table 4.2 column 5. One final comment is in order. Note that the

[7]We followed the step-by-step prescription described by Pérez-Montero (2017).

metallicity estimated for the diffuse component using HCm differs by 0.4 dex from the metallicity of the brightest star-forming knot (Table 4.2, column 1). In view of the error bars inferred from the Monte-Carlo simulation, we do not consider this difference to be significant, and our observation is consistent with UGC 2162 having a uniform metallicity.

N/O in local galaxies increases with increasing gas phase metallicity (e.g., Vincenzo et al. 2016), and can be used to constrain O/H. HCm also provides an estimate for N/O, which is consistent with O/H if UGC 2162 follows the trend observed in local galaxies (e.g., Vincenzo et al. 2016). The 1st bright point turns out to have $\log(\mathrm{N/O}) = -1.67 \pm 0.03$, or -1.52 ± 0.08 if the Monte Carlo simulation is considered. These values correspond to $12+\log(\mathrm{O/H}) < 8.5$ (e.g., Fig. 1 in Vincenzo et al. 2016), and so are compatible with the other determinations of the metallicity in UGC 2162.

4.3 Results and Implications

Figure 4.4 shows the $M_\star$ versus the gas-phase metallicity relation (MZR) derived for local dwarf galaxies by Berg et al. (2012, the red solid line, with the empty circles being the original data), as well as the relation inferred for all star-forming SDSS galaxies by Andrews & Martini (2013, the orange solid line and shaded region). Both rely on the DM to infer $12 + \log(\mathrm{O/H})$. The three blue squares represent three different estimates of the UGC 2162 metallicity as traced by the brightest knot, namely, the one inferred using HCm without [OIII]λ4363, and the two Monte-Carlo based estimates using HCm and the DM (Sect. 4.2, with the values given in Table 4.2). Thus, UGC 2162 is a high metallicity outlier of the MZR defined by local star-forming dwarfs. We have used $M_\star = 2^{+2}_{-1} \times 10^7 M_\odot$, which was inferred from the absolute magnitude and color by Trujillo et al. (2017).

The fundamental metallicity relation (FMR; Ellison et al. 2008; Mannucci et al. 2010; Lara-López et al. 2010) links the metallicity and the SFR of a galaxy. For the same stellar mass, objects with larger SFR are also metal poorer. Thus, according to the FMR, the section of the MZR plane occupied by UGC 2162 corresponds to galaxies having low SFR for their mass, which is indeed the case of UGC 2162. Objects occupying this section of the plane appear only when the surveys are not biased toward galaxies having intense emission lines, as it has been shown by, e.g., Calabrò et al. (2017). Low mass galaxies are faint, therefore, good metallicities are available only for those with the strongest emission lines, where the estimates are more precise. Thus, the empirical MZRs are inevitably biased toward high SFR objects in a way that depends on the galaxy luminosity, and so, on the galaxy mass. The interme-

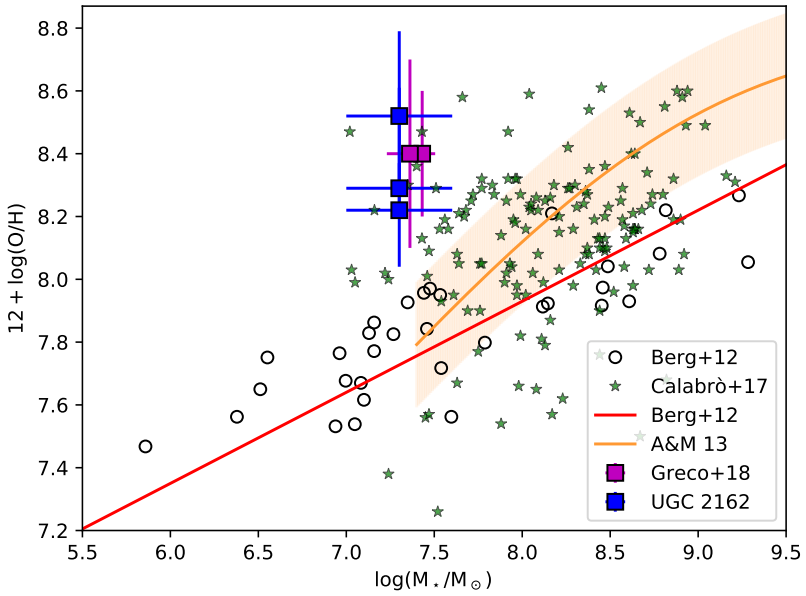

Figure 4.4: UGC 2162 in the MZR (gas-phase metallicity versus $M_\star$). The blue square symbols correspond to three different gas-phase metallicities for the brightest star-forming knot in UGC 2162 inferred from the GTC spectra (using HCm directly, HCm through a Monte Carlo simulation, and the DM; see Table 4.2). For reference, the figure includes the MZR derived for local dwarf galaxies by Berg et al. (2012, the red solid line, with the empty circles being the original data), as well as the relation inferred for all star-forming SDSS galaxies by Andrews & Martini (2013, the orange solid line, with the shaded region representing the 1σ dispersion). Other objects occupying the same region as UGC 2162 are also shown (green stars, Calabrò et al. 2017, and magenta squares, Greco et al. 2018).

diate redshift galaxies studied by Calabrò et al. (2017, with 0.13 < redshift < 0.88) have been included in Fig. 4.4 for illustration (the green stars). Even if these objects are emission line galaxies, their selection criteria do not include detecting [OIII]λ4363, and they present a large scatter in the $12 + \log(\mathrm{O/H})$ versus $M_\star$ plane. Some of them overlap with the region where UGC 2162 is located. The bias toward high SFR objects influences the current determination of the MZR, but the importance of the effect remains unclear. The impact is expected to be more pronounced at the low-mass end, and it has to be determined by comparison of the current estimates with new ones based

on volume limited samples of galaxies (e.g., Sánchez-Janssen et al. 2013), or MZRs corrected for Malmquist and surface brightness biases, as it is done when measuring luminosity functions (e.g., Takeuchi et al. 2000; Blanton et al. 2005).

The gas-phase metallicity and the surface brightness of UGC 2162 agree with the properties expected for the host galaxies having an XMP starburst analyzed by Sánchez Almeida et al. (2015). Figure 4.5 shows a scatter plot of the oxygen abundance versus surface SFR for the metal-poor star-forming region and the host galaxy of the ten galaxies studied by Sánchez Almeida et al. (2015). Host galaxies have high metallicity and low surface SFR compared to the star-forming regions. UGC 2162 has been represented in Fig. 4.5 including the three different metallicity estimates of the brightest knot and a common surface SFR of $\Sigma_{\rm SFR} = 3.4(\pm 0.5) \times 10^{-3}\ M_\odot\,{\rm yr}^{-1}\,{\rm kpc}^{-2}$. This $\Sigma_{\rm SFR}$ was inferred by Trujillo et al. (2017) from the Hα flux of the brightest star-forming knot through the calibration of Kennicutt (1998). An inspection of Fig. 4.5 shows that the surface SFR and the metallicity of UGC 2162 naturally fit the values inferred for the host galaxies[8]. Moreover, its stellar and gas masses are also typical of an XMP galaxy (for reference, see Filho et al. 2013). Thus, UGC 2162 has the properties to be expected an XMP galaxy in a pre or post starburst phase, when the bright starburst has faded away and only the host galaxy remains. Its mere existence cleans up the difficulty posed by the lack of host-like galaxies without starburst (Sect. 4.1).

UGC 2162 is a galaxy with high gas-phase metallicity for its mass. It is not unique. Some of the emission line galaxies at high redshift studied by Calabrò et al. (2017) also belong to this regime (Fig. 4.4). In addition, Greco et al. (2018) have recently characterized two diffuse dwarf galaxies in the local Universe similar to UGC 2162 in this respect, namely, LSBG-285 and LSBG-750. They are low stellar mass galaxies ($M_\star \simeq 2-3\times10^7\,M_\odot$) with a gas phase metallicity around 1/2 solar, which makes them high-metallicity outliers of the gas-phase MZR (the magenta squares in Fig. 4.4). These two objects have their stellar metallicity ($Z_\star$) estimated from the continuum emission. Although with large uncertainty, $Z_\star$ is estimated to be low, between 3 % and 10 % of the solar metallicity. What is expected if the stars were produced during past starbursts

[8]UGC 2162 is represented in Fig. 4.5 through the metallicity and surface SFR of the 1st bright point. The metallicity inferred for the diffuse component of the galaxy is somewhat larger ($\sim$ 0.4 dex; Table 4.2, column 1), but this diffuse component also has a significantly smaller $\Sigma_{\rm SFR}$ ($\sim 1/3$, attending to the ratio of Hα fluxes). Thus, we note that even the two components of UGC 2162 (diffuse and bright point) seem to follow the global trend in Fig. 4.5, where metallicity increases with decreasing $\Sigma_{\rm SFR}$. However, we are reluctant to over-interpret this result since the difference in metallicity between diffuse component and bright point may not be significant according to the error budget worked out in Sect. 4.2.2.

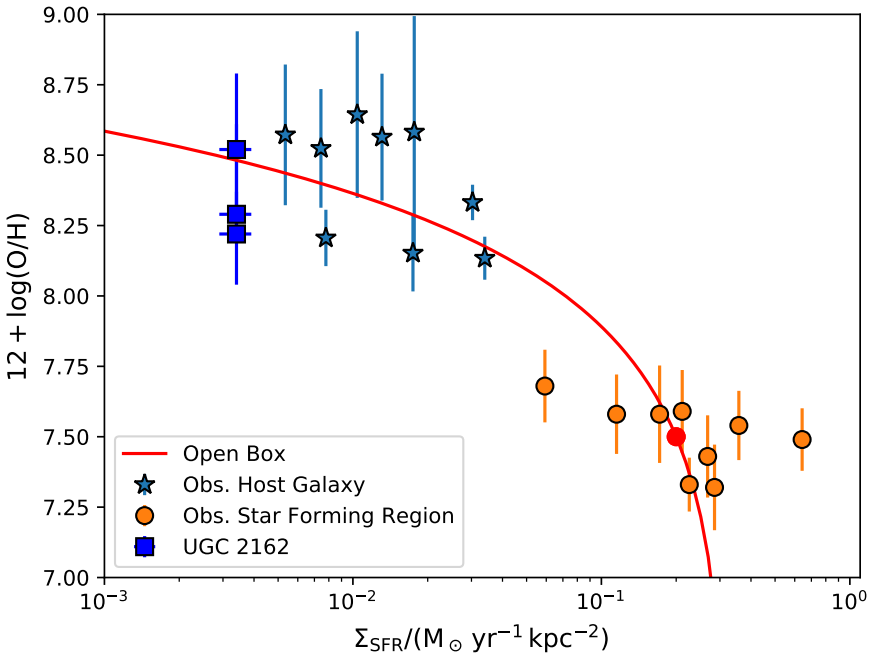

Figure 4.5: Oxygen abundance versus surface SFR for the bright star-forming region (circles) and the host galaxy (stars) of the objects analyzed by Sánchez Almeida et al. (2015). Host galaxies have high metallicity and low surface SFR compared to the starbursts. UGC 2162 is also shown as the blue squares, and it appears in the realm of the host galaxies. (We show the same three estimates included in Fig. 4.4, with the surface SFR taken from Trujillo et al. 2017.) The solid line has been included to guide the eye, and it traces the open-box evolution of the starburst shown as a red bullet, that moves from right to left along the line while SF consumes gas and produces metals (details are given in Sánchez Almeida et al. 2015).

feeding from metal-poor gas. Other works also show high metallicity outliers of the MZR, e.g., Peeples et al. (2008, in the local Universe) and Zahid et al. (2012, at redshift < 0.4).

4.4 Discussion and Conclusions

Using spectra from the 10-m GTC telescope, we confirm the relatively high metallicity of the ionized gas forming stars in the UDG UGC 2162 (Sect. 4.2 and Table 4.2). This result together with its low stellar mass make UGC 2162

a high metallicity outlier of the MZR (Fig. 4.4). Its surface SFR is also low, so that UGC 2162 seems to have all the properties characterizing the host galaxies associated with the XMP galaxies (Sects. 4.1 and 4.3). XMP galaxies have a low light-weighted mean metallicity ($Z_g < Z_\odot/10$) which, however, is often not uniform. The metallicity is low only in the young off-center bright starburst that often gives XMP galaxies their characteristic tadpole morphology (see Sect. 4.1). However, the underlying galaxy hosting the starburst is significantly more metallic than the starburst. The properties of UGC 2162 make it a candidate to be one of such host galaxies (i.e., a *XMP host galaxy*).

Detecting galaxies with the properties of the hosts is essential for consistency, because they are expected if the lopsided starburst is created by external gas accretion. These hosts are galaxies leftover after a major star-formation phase, or the precursors of XMP galaxies before a gas accretion event triggers new star-formation episodes. We have found that UGC 2162 may be one of them. Moreover, there are also other galaxies populating the high-metallicity region of the mass metallicity plane (see Sect. 4.3). These objects are usually underrepresented in emission line galaxy surveys because they are faint, low surface brightness, and with lines of low equivalent width. However, they may represent a fundamental phase in the star-formation process of low mass galaxies, which have a bursty SF history, with periods of high SF interleaved with others of inactiveness.

Systematic searches for XMP galaxies based on galaxy spectra provide objects that usually comply with the definition of Blue Compact Dwarf (BCD) galaxies (e.g., Kunth & Östlin 2000; Morales-Luis et al. 2011; Sánchez Almeida et al. 2016). Thus, the XMPs mentioned in this chapter, with luminous lopsided HII regions, seem to correspond to extreme cases of the more common BCDs. The same kind of duty cycle hypothetically linking XMPs and UDGs also fits in the relation between BCDs and their quiescent counterparts (QBCD). BCD galaxies are metal-poor systems for their stellar mass, presently going through a star-forming phase. Thus, they are relatively luminous with high surface brightness. Their outskirt light is dominated by the host galaxy, so that star-forming regions and host can be separated out (e.g., Amorín et al. 2007). Using the properties of the host galaxies to search for QBCDs, one infers the existence of a population of QBCDs 30 times more numerous than the BCDs (Sánchez Almeida et al. 2008). As expected if BCDs and QBCDs alternate their roles cyclicly, $Z_\star$ is the same in both types of galaxies, and agrees with Z_g in BCDs, during the star-forming phase of the cycle (Sánchez Almeida et al. 2009). On the other hand, Z_g in QBCDs is significantly larger than in BCDs (0.35 dex), as if their star-forming gas was already metal enriched. Their duty cycle also concurs with the luminosity-weighted ages of their respective stellar popula-

tions, being young in BCDs ($\lesssim 1$ Gyr) and older in QBCDs (from 1 to 10 Gy) (Sánchez Almeida et al. 2009). We hypothesize that the evolution of a single galaxy might be like this: from an initially quiescent state, with $Z_g > Z_\star$ as a result of a few Gyr of stellar evolution, and with $Z_\star$ equal to that in other quiescent galaxies of the same $M_\star$, an accretion event brings in relatively low metallicity gas with $Z_{g,in} < Z_g$, making a local star formation spot with low metallicity compared to other regions in the galaxy. This would be the phase observed as BCD (or XMP) because of the increase in surface brightness and luminosity caused by star formation. $Z_{g,in}$ is comparable to $Z_\star$ at the beginning of this phase, but soon after, star formation makes $Z_\star$ slightly larger than $Z_{g,in}$ and increases the stellar mass of the galaxy as well. When star formation stops the galaxy turns quiescent again, increasing Z_g over the next few Gyr. As a result, $Z_g > Z_\star$ in the new quiescent phase, with the stellar metallicity being greater than it was before, but it still consistent with the mass metallicity relation as the stellar mass has also increased.

From the point of view of the cosmological simulations of galaxy formation, low-mass high-metallicity systems are to be expected (e.g., Lagos et al. 2016; De Rossi et al. 2017; Sánchez Almeida & Dalla Vecchia 2018). Fixed $M_\star$, the galaxies of high SFR have star-forming gas of low metallicity. When this gas is consumed through SF and outflows, the small fraction that remains forming stars is contaminated by metals injected during the past SF episodes, and thus, the leftover gas tends to be fairly metallic. At this point the galaxy is underluminous and of low surface brightness. Thus, galaxies like UGC 2162 would represent systems in the late stages of consuming the gas that led to the last major outburst. This scenario fits in well the formation processes for UDGs found in zoom-in cosmological simulations from the Numerical Investigation of a Hundred Astrophysical Objects (NIHAO) project (Di Cintio et al. 2017). Some of their objects are UDGs. They reside in isolated haloes, have $M_\star$ of $10^{7-8.5}\,M_\odot$, effective radii larger than 1 kpc, and dark matter cores rather than cusps. They exhibit a broad range of colors, and a non-negligible M_g of $10^{7-9}\,M_\odot$. The presence of gas turns out to be crucial to form UDGs. Gas needs to be accreted to trigger SF. Then feedback-driven gas outflows, and the subsequent dark matter and stellar expansion, are the key to reproduce faint extended galaxies, in a process similar to the creation of dark matter cores in dwarfs (e.g., Governato et al. 2010). Somehow, dwarf galaxies with particularly bursty and prolonged SF histories tend to be extended in size, therefore, have low surface brightness when in between bursts. In a very recent paper, Chan et al. (2018) reach a similar conclusion, and they also predict the UDGs to have low $Z_\star$.

The need of significant amounts of gas that cycles between the galaxy and

its surrounding medium seems to be a central ingredient for the creation of very low surface brightness systems. UGC 2162 is a fairly gas rich object thus fitting well with the idea. However, for UGC 2162 to be truly consistent with the picture, its large gas reservoir cannot participate in the present residual SF. It has to be gas that either will fuel future SF once it settles down onto the disk, or gas driven out by past SF episodes. If the total mass of gas were participating in the SF, then according to the Kennicutt-Schmidt relation (K-S relation; e.g., Kennicutt & Evans 2012) the total SFR of the galaxy[9] would be around $6 \times 10^{-2}\,M_{\odot}\,\mathrm{yr}^{-1}$. The SFR of the main SF knot in UGC 2162 is around $8.7 \times 10^{-5}\,M_{\odot}\,\mathrm{yr}^{-1}$ (Trujillo et al. 2017), so that even if tens of knots like this one contribute to the total SF, they will never sum up to give the SFR expected if all the observed HI mass participates in the SF process.

[9] Assuming $M_{\mathrm{HI}} = 1.9 \times 10^{9}\,M_{\odot}$ and a HI radius three times the effective radius (i.e., 5.1 kpc; Trujillo et al. 2017), one gets a surface gas density of $3.3\,M_{\odot}\,\mathrm{pc}^{-2}$. Then the K-S relation in Kennicutt & Evans (2012) gives a surface SFR of $6.6 \times 10^{-4}\,M_{\odot}\,\mathrm{yr}^{-1}\,\mathrm{kpc}^{-2}$, which integrated over the optical galaxy gives a SFR of $6.0 \times 10^{-2}\,M_{\odot}\,\mathrm{yr}^{-1}$.

5

Conclusions and future work

5.1 Summary and conclusions

In this thesis we have explored the properties of Extremely Metal-Poor (XMP) galaxies in order to better understand the process of cold-flow gas accretion in the local Universe and to explore different possibilities to constrain it observationally.

In Chapter 2, I analyse the kinematics along the mayor axis of 9 XMPs, whose chemical inhomogeneities where first studied in Sánchez Almeida et al. (2015). Most XMPs have rotational velocity of around a few tens of $\mathrm{km\,s^{-1}}$. They also present turbulent motions of typically 50 $\mathrm{km\,s^{-1}}$ FWHM, thus larger than the rotational velocities. The star-forming regions appear to move coherently. The velocity is constant within each region, and the velocity dispersion sometimes increases within the star-forming clump towards the galaxy midpoint, suggesting inspiral motion toward the galaxy center. Other regions present a local maximum in velocity dispersion at their center, suggesting a moderate global expansion. No obvious relationship was found between the kinematic properties and the metallicity drops. Contrary to the metallicity, the N/O ratio remains constant along the galaxy, as expected in the metal-poor gas accretion scenario. The Hα line wings show a number of faint emission features with amplitudes around a few percent of the main Hα component, and wavelength shifts between 100 and 400 $\mathrm{km\,s^{-1}}$. The components are often paired, so that red and blue emission features with similar amplitudes and shifts appear simultaneously. The mass associated to those components ranges between 10 and 10^5 $\mathrm{M_\odot}$. Assuming the faint emission to be produced by expanding

shell-like structures, we infer a mass loss rate between 10^{-2} and a few $M_\odot\,yr^{-1}$ and a mass loading factor (mass loss rate divided by star formation rate) that exceeds 10. Since the expansion velocity of the faint emission features exceeds by far the rotational and turbulent velocities, the gas involved in the expansion may eventually escape from the galaxy disk. The observed motions involve energies consistent with the kinetic energy released by individual core-collapse supernovae. Alternative explanations for the faint emission were considered and discarded.

In Chapter 3, I present a proof-of-concept observation to detect faint Hα emission around an XMP galaxy (UM 260) using deep images taken with the 10-m GTC telescope. The images were obtained with two filters: one broad-band (BB) filter for the continuum and one medium-band (MB) filter for the line emission (Hα at the redshift of the target galaxy). The observing strategy and the reduction process were aimed at minimising the noise of the sky residual, which is the main limiting factor in the detection of faint sources. The images reach a magnitude limit of 28.8 mag arcsec^2 in the BB filter and 28.2 mag arcsec^2 in the MB filter (3σ, 10 arcsec box). I detect emission line-dominated objects all around the FOV, whose presence have been confirmed using independent detection methods. A total of 96 blobs were identified, of which 63 (66%) have a reliable detection in Hα. The measured Hα flux of the blobs is around 10^{-17} erg/s/cm^2. Assuming that the detected emission is produced by recombination of H, and that the gas temperature and density are the typical of the CGM ($T_e \simeq 10^4$ K, $n_e \sim 0.01$ cm^{-3}), I obtain gas masses for the emitting clumps of around 10^6 $M_\odot$. No evident correlation was found between the mass of the object and the distance from the target galaxy. However we find that the distribution of azimuth of the blobs is not uniform, indicating that there is a preference for the blobs to be along certain directions with respect to the target galaxy. I also detect a low surface brightness emission halo surrounding the target galaxy. The total flux of the halo, defined by the elliptical apertures enclosed within 10 and 25 arcsec from the center of the galaxy, is $4.0 \pm 0.7 \times 10^{-16}$ erg s^{-1} cm^{-2} over an area of 0.33 arcmin^2. With the same assumptions as with the blobs, the total mass of the halo is $6 \pm 1 \times 10^7$ $M_\odot$. The resulting signals are interpreted in terms of the gas in the CGM and IGM around the galaxy, as well as high redshift contaminants.

In Chapter 4, I study the ultra-diffuse galaxy (UDG) UGC2162 with the purpose of finding a galaxy sharing the properties of an XMP host but without the low metallicity starburst. I measure the high metallicity of UGC 2162 ($12 + \log[O/H] = 8.52^{+0.27}_{-0.24}$) using spectra taken with the 10-m GTC telescope. UGC 2162 has the stellar mass, metallicity, and star-formation rate (SFR) surface density expected for a host galaxy in between outbursts. This fact suggests

a physical connection between some UDGs and the metal-poor galaxies, which may be the same type of object in a different phase of the SF cycle. UGC 2162 is a high-metallicity outlier of the mass-metallicity relation, a property shared by the few UDGs with known gas-phase metallicity.

In the search for observational evidence, we drew a list of potential targets for observations. In Appendix A, I selected XMP galaxies with non-axisymmetric structures and made a classification based on their morphology. This list will be used in the future for more observing proposals.

Central results of the thesis

The most important results described in this thesis are highlighted here:

- I found expanding shell-like structures in XMPs with a mass loading factor that exceeds 10. It reveals how inefficient dwarf galaxies are at using the gas to form stars, as most of it escapes due to stellar feedback.
- I detected a low surface brightness halo in Hα and 63 emission line-dominated objects surrounding an XMP galaxy, the latter with a preference to be along certain directions. This proof-of-concept observation opens up new possibilities for studying the CGM and IGM of local galaxies through deep Hα imaging.
- I provide a list of XMP galaxies with distorted morphology, which are ideal for follow up observations in Hα aimed at detecting their CGM and IGM.
- I characterized an ultra-diffuse galaxy UGC2162 that shares the properties of an XMP host without the low metallicity starburst. They are the kind of galaxy expected before or after a gas accretion event. This had not been observed before.

5.2 Future work

As a follow-up work from the thesis, I plan to work on,

- Studying if XMPs are low-mass analogues of high-redshift clumpy galaxies, as both are growing through gas accretion. It would need to take into account the different physical conditions in both redshift regimes and the observational biases that affect them.

- To take spectra of the emission line-dominated objects identified in Chapter 3. These observations will allow us to confirm the existence of diffuse line emission around UM260, to infer the redshift of such emission, and to constraint the physical properties of the emitting gas. We can infer the kinematics from the brightest emission line and the metallicity from line ratios.

- To continue observing the galaxies selected in Appendix A, following the same observing strategy as in Chapter 3, with a spectroscopic follow-up to measure the properties of the detected objects.

- To measure the metallicity of UDGs, to confirm whether all of them can be precursors of XMPs. The stellar metallicity of UDGs is also important, and it should be much lower than that of the gas in the framework of the interpretation defended in the thesis.

A

XMP galaxies in IAC Stripe 82 Legacy Project

The work described in this appendix was carried out during the first months of the PhD. The purpose was twofold: first, to become familiar with the sample of XMPs, their properties, like colors and morphology; second, to produce a list of potential targets for future observations (for example the observations described in Chapter 3)

A.1 Description of IAC Stripe 82 Project

The target for the observations was chosen from previous searches of XMPs in the SDSS spectrum catalog (Morales-Luis et al. 2011; Sánchez Almeida et al. 2016). In order to select the optimal target for the observation, we decided to look for XMPs with distinct non-axisymmetric structures in the deep images of the IAC Stripe 82 Legacy Project.

The IAC Stripe 82 Legacy Project led by Trujillo and Fliri (Fliri & Trujillo 2016) gathers several observations of the Stripe 82 made by SDSS, reprocesses them and makes them available to the public[1]. Among other improvements with respect to the standard SDSS Stripe 82 (Jiang et al. 2008; Abazajian et al. 2009), they carried out a particular careful sky removal, leading to final images showing more low surface brightness structures. The images are in the

[1] http://www.iac.es/proyecto/stripe82/

standard SDSS filters (*u, g, r, i, z*), each composed of $30 - 100$ stacked images, making them $\sim$2 magnitudes deeper than standard SDSS images. In the sky covered by Stripe 82 ($310° < \mathrm{RA} < 60°$ and $-1.25° < \mathrm{DEC} < 1.25°$), I find $\sim$23% of the objects in the XMP lists, described below.

A.2 Classification of interesting targets

The first list I use is gathered from Morales-Luis et al. (2011). The list comes from merging the two tables present in the paper. The second list comes from Sánchez Almeida et al. (2016). In this paper there are 2 tables, and we chose the larger one to have more targets. This table is less restrictive than the other one available in the paper, because to estimate metallicity, the authors use emission lines with fluxes only twice above the noise level. Galaxies were selected based on the faint line [O III]λ4363, therefore, lowering the detection threshold tends to include more XMP galaxies in the list. The mere presence of [O III]λ4363 is a hint for metal poor gas in the emitting region.

From these lists, we selected the galaxies that can be observed in the Stripe 82 field that corresponds to the coordinate range: $310° < \mathrm{RA} < 60°$ and $-1.25° < \mathrm{DEC} < 1.25°$. These lists contain 141 and 332 objects, respectively, from which we recover a total of 107 objects in Stripe 82, i.e., $\sim$ 23% of the parent XMP sample.

I downloaded the images of each of those galaxies in each filter from the webpage of the project[2]. I smoothed the images of each galaxy with a gaussian filter of FWHM 9.4 pix (3.7 arcsec). I also made high contrast images by subtracting the smoothed image from the original image. I visually inspected the images of each galaxy: the smoothed ones to look for large scale patterns and the high contrast ones to look for small scale patterns. In the smoothed images, the presence of galactic cirrus is enhanced. The galactic cirrus are dust clouds in the Milky Way that should be avoided in our observations because they are an unwanted source of noise and complicate the sky subtraction process. In the high contrast images we can see faint substructures near to or hidden by brighter objects.

I also made color composite images using the filters *g*, *r* & *i* to resemble SDSS colors. This was done with an IDL procedure[3] described in Lupton et al. (2004). This allow us to discriminate red background sources near our XMP targets that could be misidentified as neighbours.

I selected XMP galaxies considered to be interesting for future observations

[2]http://www.iac.es/proyecto/stripe82/

[3]http://cosmo.nyu.edu/hogg/visualization/

according to various criteria. These will be described in the following subsections, where I also show images of the most representative galaxies within each category, and a table summarizing the properties of all the potential targets (Table A.1).

A.2.1 Galaxies with extended diffuse emission

The XMP galaxies selected in this category present extended emission beyond the main star forming region. Some of them are roundish whereas others present a more elongated morphology. Most of the XMPs have little blobs around with color similar to the galaxy. These blobs may be companions or satellites.

Examples of galaxies selected under this category are shown in Fig. A.1. The whole list of them are included in Table A.1, marked in the column *Classification* as diffuse.

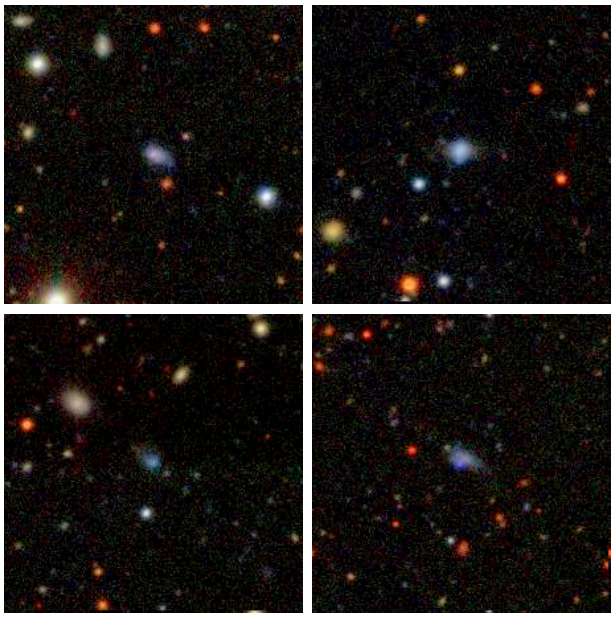

Figure A.1: Examples of galaxies with extended diffuse emission. Custom made color composition images based on IAC Stripe 82 Legacy Project g, r and i filters. The field of view in each image is 1.5×1.5 arcmin^2. These images had been tweaked to appear brighter and be seen clearly in the printed version.

A.2.2 Galaxies with two SDSS spectra

The galaxies in this category are spiral galaxies with two SDSS spectra: one in the center of the galaxy and the other at a star forming region in the outer part of the galaxy. The latter provides the rationale for the galaxy to be selected as XMP. These two spectra can be used to infer metallicity gradients. It is interesting to know how far from the galaxy center it is possible to form HII regions with such low metallicity.

Examples of galaxies selected under this category are shown in Fig. A.2. The whole list of them are included in Table A.1, marked in the column *Classification* as multi-spectra.

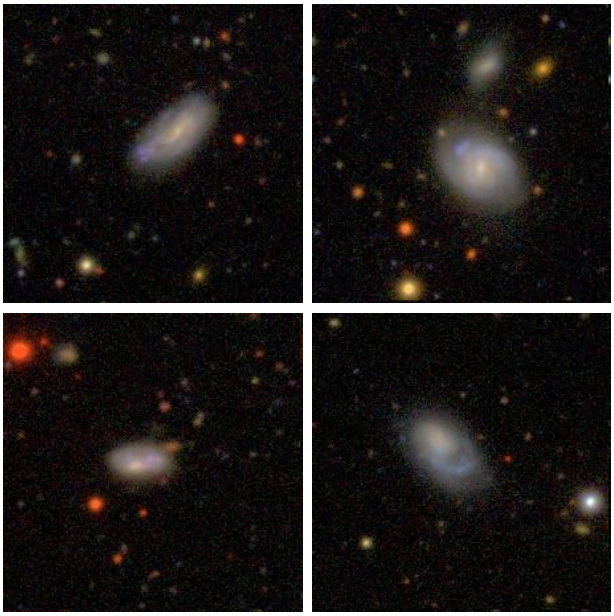

Figure A.2: Examples of galaxies with several SDSS spectra. Custom made color composition images based on IAC Stripe 82 Legacy Project g, r and i filters. The field of view in each image is 1.5×1.5 arcmin^2.

A.2.3 Galaxies with elongated morphology

The galaxies in this category have an elongated morphology, with the mayor axis two or three times the minor axis. In most of them, a particularly bright star forming region stands out. Often there is a mismatch between the elongated part and the long axis of the galaxy. They may correspond to on-going mergers.

Examples of galaxies selected under this category are shown in Fig. A.3. The whole list of them are included in Table A.1, marked in the column *Classification* as elongated.

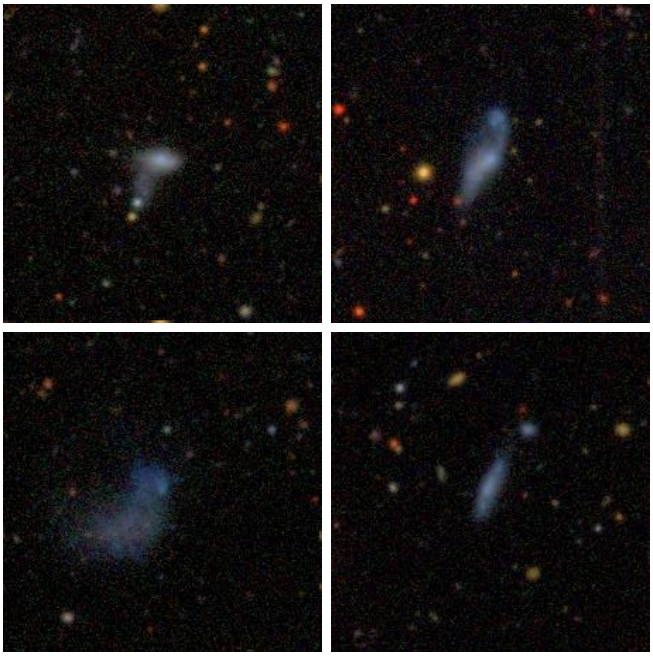

Figure A.3: Examples of galaxies with elongated morphology. Custom made color composition images based on IAC Stripe 82 Legacy Project g, r and i filters. The field of view in each image is 1.5×1.5 arcmin^2.

A.2.4 Galaxies with fragmented/clumpy morphology

The galaxies in this category have a fragmented morphology, formed by clumps of different size, close together with same color. They may trace mergers, or a few star-forming regions on an undetected faint host galaxy.

Examples of galaxies selected under this category are shown in Fig. A.4. The whole list of them are included in Table A.1, marked in the column *Classification* as fragmented.

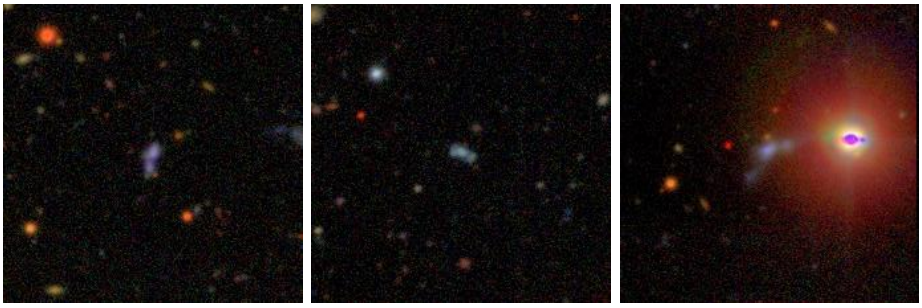

Figure A.4: Examples of galaxies with fragmented/clumpy morphology. Custom made color composition images based on IAC Stripe 82 Legacy Project g, r and i filters. The field of view in each image is 1.5×1.5 arcmin^2.

A.2.5 Galaxies with possible companions

The galaxies in this category have very near an object of similar size and color, which may be a companion. They also have little blobs around. They may portray a group of galaxies.

Examples of galaxies selected under this category are shown in Fig. A.5. The whole list of them are included in Table A.1, marked in the column *Classification* as companions.

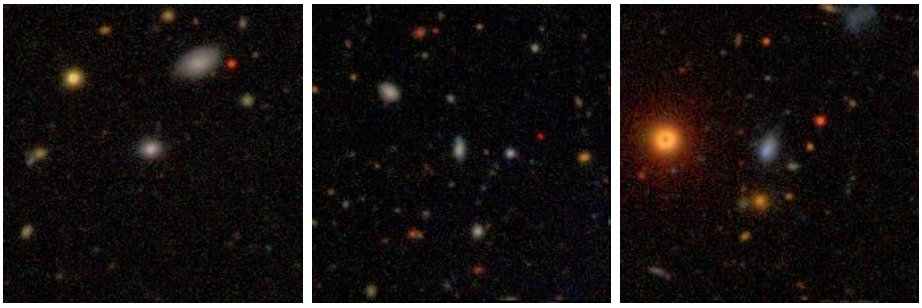

Figure A.5: Examples of galaxies with possible companions. Custom made color composition images based on IAC Stripe 82 Legacy Project g, r and i filters. The field of view in each image is 1.5×1.5 arcmin^2.

Table A.1: Properties of potential targets.

RA	DEC	Classification	Redshift	12+log(O/H) [dex]	Distance [e] [Mpc]	Size [f] [kpc]	log M_* [$M_\odot$]
21:26:58.0	−00:32:27.9	diffuse	0.0877 [c]	7.66 ± 0.17 [c]	375.9	2.79	$9.47^{+0.31}_{-0.44}$ [h]
22:50:59.3	+00:00:33.0	diffuse	0.0808 [c]	7.68 ± 0.15 [c]	346.3	1.31	8.10 ± 0.04 [g]
23:20:29.4	+00:19:37.2	diffuse	0.0251 [c]	7.53 ± 0.22 [c]	107.8	1.10	$8.27^{+0.28}_{-0.38}$ [h]
00:16:28.2	+01:08:02.0	diffuse	0.0104 [c]	7.32 ± 0.20 [c]	44.6	0.37	$7.64^{+0.29}_{-0.40}$ [h]
00:29:04.7	−01:08:26.0	diffuse	0.013 [a]	7.35 [d]	55.7	0.70	$7.88^{+0.30}_{-0.46}$ [h]
00:29:49.5	−00:25:40.0	diffuse	0.014 [a]	7.29 [d]	60.0	0.60	$6.88^{+0.26}_{-0.34}$ [h]
* 00:37:41.1	+00:33:20.2	diffuse	0.0145 [c]	7.67 ± 0.16 [c]	62.1	0.51	7.73 ± 0.014 [g]
02:44:29.0	+00:07:41.4	diffuse	0.0355 [c]	7.63 ± 0.15 [c]	152.1	1.98	$8.34^{+0.29}_{-0.39}$ [h]
03:03:31.3	−01:09:47.0	diffuse	0.030 [a]	7.48 [b]	128.6	1.27	$8.33^{+0.29}_{-0.38}$ [h]
03:02:44.7	+00:12:24.3	diffuse	0.1155 [c]	7.68 ± 0.17 [c]	495.0	1.78	$9.61^{+0.31}_{-0.43}$ [h]
03:10:24.3	+00:28:58.7	diffuse	0.1411 [c]	7.58 ± 0.22 [c]	604.7	3.77	$9.94^{+0.31}_{-0.43}$ [h]
03:16:04.2	−00:43:47.1	diffuse	0.0371 [c]	7.57 ± 0.21 [c]	159.0	2.07	$9.11^{+0.32}_{-0.49}$ [h]
03:16:45.0	+01:05:03.3	diffuse	0.1659 [c]	7.65 ± 0.18 [c]	711.0	3.24	$9.84^{+0.30}_{-0.41}$ [h]
01:53:14.9	−00:56:33.6	multi-spectra	0.0598 [c]	7.57 ± 0.22 [c]	256.3	0.70	7.58 ± 0.08 [g]
02:37:38.3	−00:54:15.4	multi-spectra	0.0387 [c]	7.58 ± 0.23 [c]	165.9	4.31	$9.40^{+0.31}_{-0.42}$ [h]
02:53:06.5	+01:09:44.9	multi-spectra	0.0589 [c]	7.56 ± 0.22 [c]	252.4	3.52	$9.06^{+0.14}_{-0.12}$ [h]
02:54:55.1	+00:06:31.9	multi-spectra	0.0141 [c]	7.28 ± 0.23 [c]	60.4	1.49	$8.34^{+0.31}_{-0.44}$ [h]
21:04:55.3	−00:35:22.0	elongated	0.005 [a]	7.05 [d]	21.4	0.25	$6.19^{+0.03}_{-0.07}$ [h]
21:28:55.9	+00:03:25.7	elongated	0.0309 [c]	7.62 ± 0.19 [c]	132.4	1.55	$7.91^{+0.08}_{-0.08}$ [h]
23:35:40.7	−00:25:33.1	elongated	0.0767 [c]	7.58 ± 0.21 [c]	328.7	1.64	$9.27^{+0.12}_{-0.07}$ [h]
23:34:14.8	+00:29:07.3	elongated	0.0238 [c]	7.66 ± 0.15 [c]	102.0	1.06	$8.07^{+0.07}_{-0.07}$ [h]
23:40:44.3	−00:53:14.9	elongated	0.0191 [c]	7.31 ± 0.19 [c]	81.9	1.44	$7.84^{+0.07}_{-0.08}$ [h]
00:15:20.7	+01:04:37.0	elongated	0.007 [a]	7.07 [d]	30.0	0.42	$7.46^{+0.29}_{-0.38}$ [h]
01:38:35.0	+00:20:05.1	elongated	0.0170 [a]	7.29 ± 0.18 [c]	72.9	0.89	$8.00^{+0.29}_{-0.39}$ [h]
01:58:09.3	−00:06:38.0	elongated	0.012 [b]	7.75 [b]	51.4	0.66	$7.89^{+0.28}_{-0.37}$ [h]
03:38:11.8	+00:13:13.0	elongated	0.043 [a]	7.64 [d]	184.3	1.05	7.74 ± 0.04 [g]
22:11:17.9	+00:48:05.0	fragmented	0.0646 [c]	7.56 ± 0.21 [c]	276.9	1.36	$9.09^{+0.31}_{-0.42}$ [h]
22:12:26.9	+01:08:35.3	fragmented	0.2101 [c]	7.59 ± 0.20 [c]	900.4	6.85	$10.01^{+0.30}_{-0.40}$ [h]
02:13:57.7	−00:02:55.7	fragmented	0.0364 [c]	7.53 ± 0.20 [c]	156.0	1.19	$8.43^{+0.29}_{-0.38}$ [h]
03:31:28.5	+00:37:37.4	fragmented	0.0494 [c]	7.69 ± 0.17 [c]	211.7	1.27	8.71 ± 0.02 [g]
23:58:52.5	+00:47:35.3	companions	0.0604 [c]	7.55 ± 0.21 [c]	258.9	1.21	$8.99^{+0.18}_{-0.10}$ [h]
00:21:03.0	−01:01:41.2	companions	0.2170 [c]	7.57 ± 0.24 [c]	930.0	4.47	$10.21^{+0.32}_{-0.46}$ [h]
02:00:08.7	+00:27:50.4	companions	0.0235 [c]	7.64 ± 0.18 [c]	100.7	0.75	$8.38^{+0.29}_{-0.40}$ [h]

[a] Redshift from SDSS DR12
[b] Redshift and metallicity from Morales-Luis et al. (2011)
[c] Redshift and metallicity from Sánchez Almeida et al. (2016)
[d] Metallicity from Guseva et al. (2009)
[e] Redshift distance, calculated as $D = cz/H_0$, where $H_0 = 70$ km s^{-1} Mpc^{-1}
[f] Size derived from parameter petroR50 of SDSS DR12
[g] Stellar mass derived from photometry colors, using Table 1 from Bell & de Jong (2001) and the solar magnitude from Willmer (2018). The errorbars are propagated from the color errors and do not take into account the uncertainty of the coefficients of the calibration in Bell & de Jong (2001)
[h] Total stellar mass from catalogue MPA-JHU(Brinchmann et al. 2004; Salim et al. 2007). These values agree with the stellar mass derived from colors, within the errorbars provided in the catalogue.
* Also known as UM260, it is the target of the observations described in Chapter 3

B

Acronyms

Table B.1: Description of the acronyms used in this thesis.

Acronym	Meaning
AGN	Active Galactic Nuclei
ALFA	Arecibo L-band Feed Array
ALFALFA	The Arecibo Legacy Fast ALFA Survey
ASK	Automatic Spectral K-means classification of galaxies
BB	Broad-Band
BCD	Blue Compact Dwarf
BH	Black Hole
CCD	Charge-Coupled Device
CGM	Circumgalactic Medium
CIB	Cosmic Ionizing Background
CWL	Central Wavelength
DM	Direct Method
DR7/9/12	Data Release 7/9/12
ETC	Exposure Time Calculator
EW	Equivalent Width
FMR	Fundamental Metallicity Relation
FOV	Field of View
FUV	Far Ultraviolet
FWHM	Full Width at Half Maximum
GALEX	Galaxy Evolution Explorer
GTC	Gran Telescopio Canarias
HCm	HII-CHI-mistry
HIPASS	HI Parkes All Sky Survey
HST	Hubble Space Telescope
IAC	Instituto de Astrofísica de Canarias

Continued on next page

Table B.1 – *Continued from previous page*

Acronym	Meaning
IDL	Interactive Data Language
IGM	Intergalactic Medium
IMF	Initial Mass Function
IRAF	Image Reduction and Analysis Facility
ISIS	Intermediate dispersion Spectrograph and Imaging System
ISM	Interstellar Medium
LARS	Lyα Reference Sample
LF	Luminosity Function
LOS	Line Of Sight
MAD	Median Absolute Deviation
MB	Medium-Band
MOSFIRE	Multi Object Spectrometer for Infra Red Exploration
MW	Milky Way
MZR	Mass-metallicity(Z) Relation
NASA	National Aeronautics and Space Administration
NED	NASA/IPAC Extragalactic Database
NIHAO	Numerical Investigation of a Hundred Astrophysical Objects
NUV	Near Ultraviolet
ORM	Observatorio del Roque de los Muchachos
OSIRIS	Optical System for Imaging and low-Intermediate- -Resolution Integrated Spectroscopy
PSF	Point Spread Function
QBCD	Quiescent Blue Compact Dwarf
RMS	Root Mean Square
SCAMP	Software for Calibrating AstroMetry and Photometry
SDSS	Sloan Digital Sky Survey
SED	Spectral Energy Distribution
SF	Star Formation
SFR	Star Formation Rate
sSFR	Specific Star Formation Rate
SHARDS	Survey for High-z Absorption Red and Dead Sources
SINFONI	Spectrograph for INtegral Field Observations in the Near Infrared
SINS	Spectroscopic Imaging survey in the Near-infrared with SINFONI
SKA	Square Kilometer Array
SN, SNa, SNe	Supernova, Supernovae
SNR, S/N	Signal to Noise Ratio
UDG	Ultra Diffuse Galaxy
UGC	Uppsala General Catalogue of Galaxies
UV	Ultraviolet
WHT	William Herschel Telescope
WISE	Wide-field Infrared Survey Explorer
XMP	eXtremely Metal-Poor

Bibliography

Abazajian, K. N., Adelman-McCarthy, J. K., Agüeros, M. A., et al. 2009, ApJS, 182, 543

Akhlaghi, M., & Ichikawa, T. 2015, ApJS, 220, 1

Alam, S., Albareti, F. D., Allende Prieto, C., et al. 2015, ApJS, 219, 12

Amorín, R., Pérez-Montero, E., Vílchez, J. M., & Papaderos, P. 2012, ApJ, 749, 185

Amorín, R. O., Muñoz-Tuñón, C., Aguerri, J. A. L., Cairós, L. M., & Caon, N. 2007, A&A, 467, 541

Amorín, R. O., Pérez-Montero, E., & Vílchez, J. M. 2010, ApJ, 715, L128

Andrews, B. H., & Martini, P. 2013, ApJ, 765, 140

Arrigoni Battaia, F., Hennawi, J. F., Prochaska, J. X., et al. 2019, MNRAS, 482, 3162

Asplund, M., Grevesse, N., Sauval, A. J., & Scott, P. 2009, ARA&A, 47, 481

Atek, H., Kunth, D., Schaerer, D., et al. 2009, A&A, 506, L1

Avni, Y., & Bahcall, J. N. 1980, ApJ, 235, 694

Bahcall, J. N., & Salpeter, E. E. 1965, ApJ, 142, 1677

Bahcall, J. N., & Spitzer, Jr., L. 1969, ApJ, 156, L63

Baldwin, J. A. 1977, MNRAS, 178, 67P

Barentsen, G., Farnhill, H. J., Drew, J. E., et al. 2014, MNRAS, 444, 3230

Bastian, N., Emsellem, E., Kissler-Patig, M., & Maraston, C. 2006, A&A, 445, 471

Bell, E. F., & de Jong, R. S. 2001, ApJ, 550, 212

Benn, C. R., & Ellison, S. L. 1998, NewAR, 42, 503

Berg, D. A., Skillman, E. D., Marble, A. R., et al. 2012, ApJ, 754, 98

Bertin, E. 2006, in Astronomical Society of the Pacific Conference Series, Vol. 351, Astronomical Data Analysis Software and Systems XV, ed. C. Gabriel, C. Arviset, D. Ponz, & S. Enrique, 112

Bertin, E., & Arnouts, S. 1996, A&AS, 117, 393

Bertin, E., Mellier, Y., Radovich, M., et al. 2002, in Astronomical Society of the Pacific Conference Series, Vol. 281, Astronomical Data Analysis Software and Systems XI, ed. D. A. Bohlender, D. Durand, & T. H. Handley, 228

Bianchi, L., Herald, J., Efremova, B., et al. 2011, Ap&SS, 335, 161

Binney, J., & Tremaine, S. 2008, Galactic Dynamics: Second Edition (Princeton University Press)

Birnboim, Y., & Dekel, A. 2003, MNRAS, 345, 349

Bland-Hawthorn, J., Maloney, P. R., Stephens, A., Zovaro, A., & Popping, A. 2017, ApJ, 849, 51

Blanton, M. R., Lupton, R. H., Schlegel, D. J., et al. 2005, ApJ, 631, 208

Bonazzola, S., Heyvaerts, J., Falgarone, E., Perault, M., & Puget, J. L. 1987, A&A, 172, 293

Bond, J. R., Kofman, L., & Pogosyan, D. 1996, Nature, 380, 603

Borlaff, A., Eliche-Moral, M. C., Beckman, J. E., et al. 2018, A&A, 615, A26

Bouché, N., Dekel, A., Genzel, R., et al. 2010, ApJ, 718, 1001

Bournaud, F., Daddi, E., Elmegreen, B. G., et al. 2008, A&A, 486, 741

Bournaud, F., Perret, V., Renaud, F., et al. 2014, ApJ, 780, 57

Bradley, L., Sipocz, B., Robitaille, T., et al. 2017, astropy/photutils: v0.4, doi:10.5281/zenodo.1039309

Bregman, J. N. 2007, ARA&A, 45, 221

Brinchmann, J., Charlot, S., White, S. D. M., et al. 2004, MNRAS, 351, 1151

Brisbin, D., & Harwit, M. 2012, ApJ, 750, 142

Calabrò, A., Amorín, R., Fontana, A., et al. 2017, A&A, 601, A95

Camps-Fariña, A., Zaragoza-Cardiel, J., Beckman, J. E., et al. 2015, MNRAS, 447, 3840

Cantalupo, S., Arrigoni-Battaia, F., Prochaska, J. X., Hennawi, J. F., & Madau, P. 2014, Nature, 506, 63

Cantalupo, S., Lilly, S. J., & Haehnelt, M. G. 2012, MNRAS, 425, 1992

Cantalupo, S., Porciani, C., Lilly, S. J., & Miniati, F. 2005, ApJ, 628, 61

Cardelli, J. A., Clayton, G. C., & Mathis, J. S. 1989, ApJ, 345, 245

Carniani, S., Marconi, A., Maiolino, R., et al. 2015, A&A, 580, A102

Cepa, J., Aguiar, M., Escalera, V. G., et al. 2000, in Proc. SPIE, Vol. 4008, Optical and IR Telescope Instrumentation and Detectors, ed. M. Iye & A. F. Moorwood, 623–631

Cepa, J., Aguiar-Gonzalez, M., Bland-Hawthorn, J., et al. 2003, in Proc. SPIE, Vol. 4841, Instrument Design and Performance for Optical/Infrared Ground-based Telescopes, ed. M. Iye & A. F. M. Moorwood, 1739–1749

Ceverino, D., Dekel, A., & Bournaud, F. 2010, MNRAS, 404, 2151

Ceverino, D., Sánchez Almeida, J., Muñoz Tuñón, C., et al. 2016, MNRAS, 457, 2605

Chan, T. K., Kereš, D., Wetzel, A., et al. 2018, MNRAS, 478, 906

Chandrasekhar, S. 1951, Proceedings of the Royal Society of London Series A, 210, 18

Chang, Y.-Y., van der Wel, A., da Cunha, E., & Rix, H.-W. 2015, The Astrophysical Journal Supplement Series, 219, 8

Cheung, E., Stark, D. V., Huang, S., et al. 2016, ApJ, 832, 182

Christensen, C. R., Davé, R., Governato, F., et al. 2016, ApJ, 824, 57

Cid Fernandes, R., & Terlevich, R. 1994, Line profiles in compact supernova remnants and active galactic nuclei., ed. G. Tenorio-Tagle

Conselice, C. J. 2018, Research Notes of the American Astronomical Society, 2, 43

Cresci, G., Mannucci, F., Maiolino, R., et al. 2010, Nature, 467, 811

Dalcanton, J. J., Spergel, D. N., Gunn, J. E., Schmidt, M., & Schneider, D. P. 1997, AJ, 114, 635

Dalcanton, J. J., & Stilp, A. M. 2010, ApJ, 721, 547

Dale, D. A., Barlow, R. J., Cohen, S. A., et al. 2008, AJ, 135, 1412

Davé, R., Finlator, K., & Oppenheimer, B. D. 2012, MNRAS, 421, 98

Dawson, S., Rhoads, J. E., Malhotra, S., et al. 2007, ApJ, 671, 1227

de Avillez, M. A., & Mac Low, M.-M. 2002, ApJ, 581, 1047

de Blok, W. J. G., Fraternali, F., Heald, G. H., et al. 2015, ArXiv e-prints, arXiv:1501.01211

De Rossi, M. E., Bower, R. G., Font, A. S., Schaye, J., & Theuns, T. 2017, MNRAS, 472, 3354

Dekel, A., & Birnboim, Y. 2006, MNRAS, 368, 2

Dekel, A., & Mandelker, N. 2014, MNRAS, 444, 2071

Dekel, A., Birnboim, Y., Engel, G., et al. 2009, Nature, 457, 451

Di Cintio, A., Brook, C. B., Dutton, A. A., et al. 2017, MNRAS, 466, L1

Dijkstra, M., & Loeb, A. 2009, MNRAS, 400, 1109

Dopita, M. A., & Sutherland, R. S. 1995, ApJ, 455, 468

Drake, A. B., Guiderdoni, B., Blaizot, J., et al. 2017, MNRAS, 471, 267

Dwarkadas, V. V., & Gruszko, J. 2012, MNRAS, 419, 1515

Eckert, K. D., Kannappan, S. J., Stark, D. V., et al. 2015, ApJ, 810, 166

Efstathiou, G. 1992, MNRAS, 256, 43P

Ellison, S. L., Patton, D. R., Simard, L., & McConnachie, A. W. 2008, ApJ, 672, L107

Elmegreen, B. G., Bournaud, F., & Elmegreen, D. M. 2008, ApJ, 688, 67

Elmegreen, B. G., Elmegreen, D. M., Sánchez Almeida, J., et al. 2013, ApJ, 774, 86

Elmegreen, B. G., Zhang, H.-X., & Hunter, D. A. 2012a, ApJ, 747, 105

Elmegreen, D. M., Elmegreen, B. G., Sánchez Almeida, J., et al. 2012b, ApJ, 750, 95

—. 2016a, ApJ, 825, 145

Elmegreen, D. M., Elmegreen, B. G., Sanchez Almeida, J., et al. 2016b, ArXiv e-prints, arXiv:1605.02822

Emerson, D. 1996, Interpreting Astronomical Spectra, 472

Epinat, B., Amram, P., Marcelin, M., et al. 2008, MNRAS, 388, 500

Epstein, E. E. 1964, AJ, 69, 521

Faucher-Giguère, C.-A., Kereš, D., Dijkstra, M., Hernquist, L., & Zaldarriaga, M. 2010, ApJ, 725, 633

Ferrara, A., Salvadori, S., Yue, B., & Schleicher, D. 2014, MNRAS, 443, 2410

Fierlinger, K. M., Burkert, A., Ntormousi, E., et al. 2016, MNRAS, 456, 710

Filho, M. E., Fraternali, F., Markoff, S., et al. 2004, A&A, 418, 429

Filho, M. E., Sánchez Almeida, J., Muñoz-Tuñón, C., et al. 2015, ApJ, 802, 82

Filho, M. E., Winkel, B., Sánchez Almeida, J., et al. 2013, A&A, 558, A18

Fisher, D. B., Glazebrook, K., Damjanov, I., et al. 2016, MNRAS, arXiv:1608.08241

Fliri, J., & Trujillo, I. 2016, MNRAS, 456, 1359

Ford, A. B., Davé, R., Oppenheimer, B. D., et al. 2014, MNRAS, 444, 1260

Förster Schreiber, N. M., Genzel, R., Bouché, N., et al. 2009, ApJ, 706, 1364

Fox, A., & Davé, R., eds. 2017, Astrophysics and Space Science Library, Vol. 430, Gas Accretion onto Galaxies

Frank, J., King, A., & Raine, D. J. 2002, Accretion Power in Astrophysics: Third Edition, 398

Fukugita, M., Ichikawa, T., Gunn, J. E., et al. 1996, AJ, 111, 1748

Fumagalli, M., O'Meara, J. M., & Prochaska, J. X. 2011a, Science, 334, 1245

Fumagalli, M., Prochaska, J. X., Kasen, D., et al. 2011b, MNRAS, 418, 1796

Furlanetto, S. R., Schaye, J., Springel, V., & Hernquist, L. 2003, ApJ, 599, L1

Gallego, S. G., Cantalupo, S., Lilly, S., et al. 2018, MNRAS, 475, 3854

Gaustad, J. E., McCullough, P. R., Rosing, W., & Van Buren, D. 2001, PASP, 113, 1326

Genzel, R., Tacconi, L. J., Gracia-Carpio, J., et al. 2010, MNRAS, 407, 2091

Gill, C. D., & O'Brien, T. J. 1999, MNRAS, 307, 677

Giovanelli, R., Haynes, M. P., Kent, B. R., et al. 2005, AJ, 130, 2598

Gnedin, N. Y., Tasker, E. J., & Fujimoto, Y. 2014, ApJ, 787, L7

Goerdt, T., Dekel, A., Sternberg, A., et al. 2010, MNRAS, 407, 613

González-Martín, O., Masegosa, J., Márquez, I., Guerrero, M. A., & Dultzin-Hacyan, D. 2006, A&A, 460, 45

Gould, A., & Weinberg, D. H. 1996, ApJ, 468, 462

Governato, F., Brook, C., Mayer, L., et al. 2010, Nature, 463, 203

Greco, J. P., Goulding, A. D., Greene, J. E., et al. 2018, ApJ, 866, 112

Gunn, J. E., & Peterson, B. A. 1965, ApJ, 142, 1633

Guseva, N. G., Papaderos, P., Meyer, H. T., Izotov, Y. I., & Fricke, K. J. 2009, A&A, 505, 63

Hayes, M., Östlin, G., Schaerer, D., et al. 2010, Nature, 464, 562

—. 2013, ApJ, 765, L27

Hayes, M., Östlin, G., Duval, F., et al. 2014, ApJ, 782, 6

Herenz, E. C., Hayes, M., Papaderos, P., et al. 2017, A&A, 606, L11

Herenz, E. C., Wisotzki, L., Saust, R., et al. 2019, A&A, 621, A107

Hernquist, L., Katz, N., Weinberg, D. H., & Miralda-Escudé, J. 1996, ApJ, 457, L51

Hinojosa-Goñi, R., Muñoz-Tuñón, C., & Méndez-Abreu, J. 2016, ArXiv e-prints, arXiv:1604.01698

Hinz, J. L., Rix, H.-W., & Bernstein, G. M. 2001, AJ, 121, 683

Hirschauer, A. S., Salzer, J. J., Skillman, E. D., et al. 2016, ApJ, 822, 108

Hogg, D. W. 1999, ArXiv Astrophysics e-prints, astro-ph/9905116

Holwerda, B. W. 2005, ArXiv Astrophysics e-prints, astro-ph/0512139

Hsyu, T., Cooke, R. J., Prochaska, J. X., & Bolte, M. 2017, ApJ, 845, L22

Hu, E. M. 1992, ApJ, 391, 608

Hwang, H.-C., & et al. 2018, ApJ, preprint

Impey, C., & Bothun, G. 1997, ARA&A, 35, 267

Israelian, G., Ecuvillon, A., Rebolo, R., et al. 2004, A&A, 421, 649

Izotov, Y. I., & Thuan, T. X. 1999, ApJ, 511, 639

Izotov, Y. I., Thuan, T. X., & Guseva, N. G. 2012, A&A, 546, A122

Jaiswal, S., & Omar, A. 2016, MNRAS, 462, 92

James, B. L., Koposov, S., Stark, D. P., et al. 2015, MNRAS, 448, 2687

James, P. A., Shane, N. S., Beckman, J. E., et al. 2004, A&A, 414, 23

Jiang, L., Fan, X., Annis, J., et al. 2008, AJ, 135, 1057

Kaaret, P., Schmitt, J., & Gorski, M. 2011, ApJ, 741, 10

Kasen, D., & Woosley, S. E. 2009, ApJ, 703, 2205

Kehrig, C., Vílchez, J. M., Pérez-Montero, E., et al. 2015, ApJ, 801, L28

Keller, B. W., Wadsley, J., Benincasa, S. M., & Couchman, H. M. P. 2014, MNRAS, 442, 3013

Kennicutt, R. C., & Evans, N. J. 2012, ARA&A, 50, 531

Kennicutt, Jr., R. C. 1998, ARA&A, 36, 189

Kereš, D., Katz, N., Weinberg, D. H., & Davé, R. 2005, MNRAS, 363, 2

Kollmeier, J. A., Zheng, Z., Davé, R., et al. 2010, ApJ, 708, 1048

Kormendy, J., & Ho, L. C. 2013, ARA&A, 51, 511

Kravtsov, A. V. 2013, ApJ, 764, L31

Kunth, D., & Östlin, G. 2000, A&A Rev., 10, 1

Lagos, C. d. P., Theuns, T., Schaye, J., et al. 2016, MNRAS, 459, 2632

Lang, K. R. 1999, Astrophysical formulae

Lara-López, M. A., Cepa, J., Bongiovanni, A., et al. 2010, A&A, 521, L53

Lee, J. C., Veilleux, S., McDonald, M., & Hilbert, B. 2016, ApJ, 817, 177

Leibler, C. N., Cantalupo, S., Holden, B. P., & Madau, P. 2018, MNRAS, 480, 2094

Leitherer, C., Schaerer, D., Goldader, J. D., et al. 1999, ApJS, 123, 3

Lin, L., Lin, J.-H., Hsu, C.-H., et al. 2017, ApJ, 837, 32

Lupton, R., Blanton, M. R., Fekete, G., et al. 2004, PASP, 116, 133

Ly, C., Rigby, J. R., Cooper, M., & Yan, R. 2015, ApJ, 805, 45

Mac Low, M.-M., & Ferrara, A. 1999, ApJ, 513, 142

Maiolino, R., Gallerani, S., Neri, R., et al. 2012, MNRAS, 425, L66

Mandelker, N., Dekel, A., Ceverino, D., et al. 2014, MNRAS, 443, 3675

Mannucci, F., Cresci, G., Maiolino, R., Marconi, A., & Gnerucci, A. 2010, MNRAS, 408, 2115

Martin, B. R. 1971, Statistics for physicists

Martin, C. L. 1999, ApJ, 513, 156

Martin, C. L., Shapley, A. E., Coil, A. L., et al. 2012, ApJ, 760, 127

Martin, D. C., Chang, D., Matuszewski, M., et al. 2014, ApJ, 786, 107

Martins, F. 2015, in SF2A-2015: Proceedings of the Annual meeting of the French Society of Astronomy and Astrophysics, ed. F. Martins, S. Boissier, V. Buat, L. Cambrésy, & P. Petit, 343–348

Matteucci, F. 2004, in Origin and Evolution of the Elements, ed. A. McWilliam & M. Rauch, 85

McQuinn, M. 2016, ARA&A, 54, 313

Meaburn, J. 1984, MNRAS, 211, 521

Meyer, M. J., Zwaan, M. A., Webster, R. L., et al. 2004, MNRAS, 350, 1195

Miller, J. S. 1974, ARA&A, 12, 331

Morales-Luis, A. B., Sánchez Almeida, J., Aguerri, J. A. L., & Muñoz-Tuñón, C. 2011, ApJ, 743, 77

Moran, S. M., Heckman, T. M., Kauffmann, G., et al. 2012, ApJ, 745, 66

Mori, M., Umemura, M., & Ferrara, A. 2004, ApJ, 613, L97

Moss, C., Whittle, M., & Irwin, M. J. 1988, MNRAS, 232, 381

Münch, G., & Zirin, H. 1961, ApJ, 133, 11

Murray, N., & Chang, P. 2015, ApJ, 804, 44

Newman, S. F., Genzel, R., Förster-Schreiber, N. M., et al. 2012, ApJ, 761, 43

Newville, M., Stensitzki, T., Allen, D. B., & Ingargiola, A. 2014, LMFIT: Non-Linear Least-Square Minimization and Curve-Fitting for Python¶, doi:10.5281/zenodo.11813

Ohyama, Y., Taniguchi, Y., Kawabata, K. S., et al. 2003, ApJ, 591, L9

Oke, J. B. 1974, ApJS, 27, 21

Olmo-García, A., Sánchez Almeida, J., Muñoz-Tuñón, C., et al. 2017, ApJ, 834, 181

Oppenheimer, B. D., Davé, R., Katz, N., Kollmeier, J. A., & Weinberg, D. H. 2012, MNRAS, 420, 829

Osterbrock, D. E. 1974, Astrophysics of gaseous nebulae

Östlin, G., Hayes, M., Duval, F., et al. 2014, ApJ, 797, 11

Pacucci, F., Ferrara, A., Grazian, A., et al. 2016, MNRAS, 459, 1432

Papaderos, P., Guseva, N. G., Izotov, Y. I., & Fricke, K. J. 2008, A&A, 491, 113

Pedani, M. 2004, NewA, 9, 641

Peeples, M. S., Pogge, R. W., & Stanek, K. Z. 2008, ApJ, 685, 904

Peeples, M. S., & Shankar, F. 2011, MNRAS, 417, 2962

Peeples, M. S., Werk, J. K., Tumlinson, J., et al. 2014, ApJ, 786, 54

Pérez-González, P. G., Cava, A., Barro, G., et al. 2013, ApJ, 762, 46

Pérez-Montero, E. 2014, MNRAS, 441, 2663

—. 2017, PASP, 129, 043001

Pérez-Montero, E., & Contini, T. 2009, MNRAS, 398, 949

Pérez-Montero, E., Contini, T., Lamareille, F., et al. 2013, A&A, 549, A25

Pettini, M., & Pagel, B. E. J. 2004, MNRAS, 348, L59

Popping, A., & Braun, R. 2011, A&A, 527, A90

Press, W. H., Flannery, B. P., & Teukolsky, S. A. 1986, Numerical recipes. The art of scientific computing

Prestwich, A. H., Tsantaki, M., Zezas, A., et al. 2013, ApJ, 769, 92

Putman, M. E., Peek, J. E. G., & Joung, M. R. 2012, ARA&A, 50, 491

Read, J. I., Iorio, G., Agertz, O., & Fraternali, F. 2016, MNRAS, 462, 3628

Rees, M. J. 1986, MNRAS, 218, 25P

Robertson, B., & Goldreich, P. 2012, ApJ, 750, L31

Rosdahl, J., & Blaizot, J. 2012, MNRAS, 423, 344

Sabbi, E., Anderson, J., Lennon, D. J., et al. 2013, AJ, 146, 53

Salim, S., Rich, R. M., Charlot, S., et al. 2007, ApJS, 173, 267

Salucci, P., Lapi, A., Tonini, C., et al. 2007, MNRAS, 378, 41

Sánchez Almeida, J. 2017, in Astrophysics and Space Science Library, Vol. 430, Gas Accretion onto Galaxies, ed. A. Fox & R. Davé, 67

Sánchez Almeida, J., Aguerri, J. A. L., Muñoz-Tuñón, C., & de Vicente, A. 2010, ApJ, 714, 487

Sánchez Almeida, J., Aguerri, J. A. L., Muñoz-Tuñón, C., & Vazdekis, A. 2009, ApJ, 698, 1497

Sánchez Almeida, J., Caon, N., Muñoz-Tuñón, C., Filho, M., & Cerviño, M. 2018a, MNRAS, 476, 4765

Sánchez Almeida, J., & Dalla Vecchia, C. 2018, ApJ, 859, 109

Sánchez Almeida, J., Elmegreen, B. G., Muñoz-Tuñón, C., & Elmegreen, D. M. 2014a, A&A Rev., 22, 71

Sánchez Almeida, J., Filho, M. E., Dalla Vecchia, C., & Skillman, E. D. 2017, ApJ, 835, 159

Sánchez Almeida, J., Morales-Luis, A. B., Muñoz-Tuñón, C., et al. 2014b, ApJ, 783, 45

Sánchez Almeida, J., Muñoz-Tuñón, C., Amorín, R., et al. 2008, ApJ, 685, 194

Sánchez Almeida, J., Muñoz-Tuñón, C., Elmegreen, D. M., Elmegreen, B. G., & Méndez-Abreu, J. 2013, ApJ, 767, 74

Sánchez Almeida, J., Olmo-García, A., Elmegreen, B. G., et al. 2018b, ApJ, 869, 40

Sánchez Almeida, J., Pérez-Montero, E., Morales-Luis, A. B., et al. 2016, ApJ, 819, 110

Sánchez Almeida, J., Terlevich, R., Terlevich, E., Cid Fernandes, R., & Morales-Luis, A. B. 2012, ApJ, 756, 163

Sánchez Almeida, J., Elmegreen, B. G., Muñoz-Tuñón, C., et al. 2015, ApJ, 810, L15

Sánchez-Janssen, R., Amorín, R., García-Vargas, M., et al. 2013, A&A, 554, A20

Sánchez-Menguiano, L., Sánchez Almeida, J., Muñoz-Tuñón, C., et al. 2019, arXiv e-prints, arXiv:1904.03930

Sancisi, R., Fraternali, F., Oosterloo, T., & van der Hulst, T. 2008, A&A Rev., 15, 189

Schweizer, F. 1979, PASP, 91, 149

Seljak, U., Makarov, A., McDonald, P., et al. 2005, Phys. Rev. D, 71, 103515

Shen, S., Madau, P., Aguirre, A., et al. 2012, ApJ, 760, 50

Shull, J. M., Smith, B. D., & Danforth, C. W. 2012, ApJ, 759, 23

Silk, J., & Mamon, G. A. 2012, Research in Astronomy and Astrophysics, 12, 917

Skillman, E. D. 1999, in Astronomical Society of the Pacific Conference Series, Vol. 170, The Low Surface Brightness Universe, ed. J. I. Davies, C. Impey, & S. Phillips, 169

Skillman, E. D., Kennicutt, R. C., & Hodge, P. W. 1989, ApJ, 347, 875

Skillman, E. D., Salzer, J. J., Berg, D. A., et al. 2013, AJ, 146, 3

Sobral, D., Smail, I., Best, P. N., et al. 2013, MNRAS, 428, 1128

Spite, M., Cayrel, R., Plez, B., et al. 2005, A&A, 430, 655

Spitzer, Jr., L. 1956, ApJ, 124, 20

Stark, D. V., Kannappan, S. J., Eckert, K. D., et al. 2016, ApJ, 832, 126

Stasińska, G. 2004, in Cosmochemistry. The melting pot of the elements, ed. C. Esteban, R. García López, A. Herrero, & F. Sánchez, 115–170

Stern, J., Hennawi, J. F., Prochaska, J. X., & Werk, J. K. 2016, ApJ, 830, 87

Stroe, A., Sobral, D., Matthee, J., Calhau, J., & Oteo, I. 2017, MNRAS, 471, 2575

Takeuchi, T. T., Yoshikawa, K., & Ishii, T. T. 2000, ApJS, 129, 1

Taniguchi, Y., & Shioya, Y. 2000, ApJ, 532, L13

Taylor, M. B. 2006, in Astronomical Society of the Pacific Conference Series, Vol. 351, Astronomical Data Analysis Software and Systems XV, ed. C. Gabriel, C. Arviset, D. Ponz, & S. Enrique, 666

Tenorio-Tagle, G., Munoz-Tunon, C., & Cid-Fernandes, R. 1996, ApJ, 456, 264

Thompson, T. A., & Krumholz, M. R. 2016, MNRAS, 455, 334

Thoul, A. A., & Weinberg, D. H. 1996, ApJ, 465, 608

Tinsley, B. M. 1981, ApJ, 250, 758

Troncoso, P., Maiolino, R., Sommariva, V., et al. 2014, A&A, 563, A58

Trujillo, I., & Fliri, J. 2016, ApJ, 823, 123

Trujillo, I., Roman, J., Filho, M., & Sánchez Almeida, J. 2017, ApJ, 836, 191

Tumlinson, J., Peeples, M. S., & Werk, J. K. 2017, Annual Review of Astronomy and Astrophysics, 55, 389

van de Voort, F., & Schaye, J. 2012, MNRAS, 423, 2991

van der Kruit, P., & Freeman, K. 2011, Annual Review of Astronomy and Astrophysics, 49, 301

van Dokkum, P. G. 2001, PASP, 113, 1420

van Dokkum, P. G., Abraham, R., Merritt, A., et al. 2015, ApJ, 798, L45

van Wassenhove, S., Volonteri, M., Walker, M. G., & Gair, J. R. 2010, MNRAS, 408, 1139

Veilleux, S., Cecil, G., & Bland-Hawthorn, J. 2005, ARA&A, 43, 769

Viel, M., Lesgourgues, J., Haehnelt, M. G., Matarrese, S., & Riotto, A. 2005, Phys. Rev. D, 71, 063534

Vilchez, J. M., Pagel, B. E. J., Diaz, A. I., Terlevich, E., & Edmunds, M. G. 1988, MNRAS, 235, 633

Vincenzo, F., Belfiore, F., Maiolino, R., Matteucci, F., & Ventura, P. 2016, MNRAS, 458, 3466

Volonteri, M. 2010, A&A Rev., 18, 279

Willmer, C. N. A. 2018, ApJS, 236, 47

Wisotzki, L., Bacon, R., Blaizot, J., et al. 2016, A&A, 587, A98

Wisotzki, L., Bacon, R., Brinchmann, J., et al. 2018, Nature, 562, 229

Yang, C.-C., & Krumholz, M. 2012, ApJ, 758, 48

Zahid, H. J., Bresolin, F., Kewley, L. J., Coil, A. L., & Davé, R. 2012, ApJ, 750, 120

Zhang, Y., Anninos, P., & Norman, M. L. 1995, ApJ, 453, L57

Zheng, Z.-Y., Finkelstein, S. L., Finkelstein, K., et al. 2013, MNRAS, 431, 3589

Zuckerman, B. 1987, in Spectroscopy of Astrophysical Plasmas, ed. A. Dalgarno & D. Layzer, 185–209